



저작자표시-비영리-변경금지 2.0 대한민국

이용자는 아래의 조건을 따르는 경우에 한하여 자유롭게

- 이 저작물을 복제, 배포, 전송, 전시, 공연 및 방송할 수 있습니다.

다음과 같은 조건을 따라야 합니다:



저작자표시. 귀하는 원저작자를 표시하여야 합니다.



비영리. 귀하는 이 저작물을 영리 목적으로 이용할 수 없습니다.



변경금지. 귀하는 이 저작물을 개작, 변형 또는 가공할 수 없습니다.

- 귀하는, 이 저작물의 재이용이나 배포의 경우, 이 저작물에 적용된 이용허락조건을 명확하게 나타내어야 합니다.
- 저작권자로부터 별도의 허가를 받으면 이러한 조건들은 적용되지 않습니다.

저작권법에 따른 이용자의 권리는 위의 내용에 의하여 영향을 받지 않습니다.

이것은 [이용허락규약\(Legal Code\)](#)을 이해하기 쉽게 요약한 것입니다.

[Disclaimer](#)

이학박사학위논문

**Mott Physics
in Multicomponent Systems**

뭇성분계의 모트 물리

2015년 2월

서울대학교 대학원

물리천문학부

김 아 람

Mott Physics
in Multicomponent Systems

뭇성분계의 모트 물리

지도교수 최 무 영

이 논문을 이학박사 학위논문으로 제출함

2014년 12월

서울대학교 대학원

물리천문학부

김 아 람

김아람의 이학박사 학위논문을 인준함

2014년 12월

위 원 장 유 재 준 (인)

부위원장 최 무 영 (인)

위 원 민 홍 기 (인)

위 원 이 진 호 (인)

위 원 전 건 상 (인)

Mott Physics in Multicomponent Systems

Aaram J. Kim

Supervised by

Professor **MooYoung Choi**

A Dissertation

Submitted to the Faculty of

Seoul National University

in Partial Fulfillment of

the Requirements for the Degree of

Doctor of Philosophy

December 2014

Department of Physics and Astronomy

Graduate School

Seoul National University

Abstract

We investigate Hubbard-type models by means of the dynamical mean-field theory (DMFT) combined with the continuous-time quantum Monte Carlo (CTQMC) method. In this thesis, a great deal of effort has been devoted to investigating diverse facets of Mott physics. Interesting phenomena in strongly correlated electron systems emerge mostly when various energy scales compete with each other. We introduce additional degrees of freedom to the standard Hubbard model. The additional degrees of freedom include a staggered lattice potential, two orbitals, bilayer structure, and superconductivity. Depending on the model system, we extend the single-site DMFT to the multi-orbital one or employ cluster extension of the DMFT. In addition, two complementary versions of CTQMC, weak and strong coupling algorithm, are adopted as an impurity solver.

We first consider a Mott transition of the Hubbard model in infinite dimensions. The DMFT is employed in combination with the CTQMC method for an accurate description at low temperatures. Through the use of the double occupancy and the energy density, which are directly measured via the CTQMC method, we construct the phase diagram. We pay particular attention to the

construction of the first-order phase transition line (PTL) in the coexistence region of metallic and insulating phases. The resulting PTL is found to exhibit reasonable agreement with earlier finite-temperature results. We also show, by including systematically low-temperature data, that the PTL, which is obtained independently of the previous zero-temperature results, approaches monotonically the transition point reported in earlier zero-temperature studies.

We next investigate paramagnetic metal-insulator transitions in the infinite-dimensional ionic Hubbard model at finite temperatures. By means of the DMFT with an impurity solver of the CTQMC, we show that an increase in the interaction strength brings about a crossover from a band insulating phase to a metallic one, followed by a first-order transition to the Mott insulating phase. The first-order transition turns into a crossover above a certain critical temperature, which becomes higher as the strength of the staggered lattice potential is increased. Further, analysis of the temperature dependence of the energy density discloses that the intermediate metallic phase is a Fermi liquid. It is also found that the metallic phase is stable against strong staggered potentials even at very low temperatures.

Finite-temperature phase transitions are also examined in the two-orbital Hubbard model with Ising-type Hund's coupling. We adopt the multi-orbital extension of the DMFT combined with the strong coupling CTQMC. It is found that there emerges a peculiar reverse-sloped first-order Mott transition between the orbital-selective Mott phase and the Mott insulator phase. It turns out that the increase of Hund's coupling lowers the critical temperature

of the reverse-sloped Mott transition. Beyond a certain critical value of Hund's coupling the first-order transition becomes a finite-temperature crossover.

Bilayer effects in the Hubbard model are also studied in the dynamical cluster approximation (DCA) combined with the weak coupling algorithm of CTQMC. In the magnetic phase diagrams obtained in earlier studies, there still remain several controversial issues, particularly for weak on-site Coulomb interactions. In this study, we adopt eight-site clusters which preserve the underlying lattice symmetry. Magnetic properties and associated metal-insulator transitions are examined at low temperatures, and their implications to the ground-state phase diagram are also discussed.

Finally, we discuss the BCS+ U model which is a natural generalization of Gutzwiller-projected BCS model. For this study, we use the DCA combined with the weak coupling CTQMC and verify the reliability of our calculation by changing the cluster size. Our main focus is on the correlation effects of the phenomenological d -wave superconductor. The transition between the superconductor and the Mott insulator is observed as we change the interaction strength or doping concentration. We discuss the change in the spectral properties of the system during the transition.

Keywords: strongly correlated electron systems, Hubbard-type model, dynamical mean-field theory, continuous-time quantum Monte Carlo method

Student Number: 2009-20403

Contents

Abstract	i
1 Introduction	1
2 Hubbard Model and Strongly Correlated Systems	5
2.1 Derivation	8
2.2 Limiting cases	10
2.2.1 Noninteracting limit	10
2.2.2 Atomic limit	13
2.2.3 Infinite dimensions	14
2.3 Symmetries	19
2.3.1 Spin-rotational symmetry	19
2.3.2 Particle-hole symmetry	21
2.4 Multi-orbital Hubbard model	21
2.4.1 Hund's coupling	24
3 Numerical Methods	26
3.1 Dynamical Mean-Field Theory	26

3.2	Dynamical Cluster Approximation	29
3.3	Continuous-Time Quantum Monte Carlo method	31
3.3.1	Weak Coupling Algorithm	32
3.3.2	Strong Coupling Algorithm	35
4	Estimate of the Phase Transition Line in the Infinite-Dimensional Hubbard Model	40
4.1	Introduction	40
4.2	Model and method	43
4.3	Results	45
4.3.1	Double occupancy and energy density	45
4.3.2	Phase diagram and critical point	47
4.3.3	Phase transition line	50
4.3.4	Transition interaction strength at zero temperature . . .	57
4.3.5	Next-order correction	58
4.4	Summary	59
5	Correlation Effects in Band Insulator	60
5.1	Introduction	60
5.2	Model and methods	64
5.3	Results	66
5.3.1	Spectral properties	66
5.3.2	Local quantities	71
5.3.3	Energy density	74
5.3.4	Finite-temperature phase transition	77

5.3.5	Nature of the intermediate metallic phase	80
5.3.6	Critical point of the Mott transition	83
5.3.7	Phase diagram at low temperatures	84
5.4	Summary	86
6	Orbital Selective Mott Phase and Finite Temperature Transitions	87
6.1	Introduction	87
6.2	Model and methods	89
6.3	Results	91
6.3.1	Finite-temperature phase diagram	91
6.3.2	Spectral function and self-energy	93
6.3.3	Local magnetic moments	95
6.3.4	Effects of Hund's coupling	97
6.4	Summary	99
7	Magnetic Properties in the Bilayer Hubbard Model	100
7.1	Introduction	100
7.2	Model	102
7.3	Results	104
7.3.1	Staggered magnetization	104
7.3.2	Néel temperatures	106
7.3.3	Spin-resolved local spectral function	107
7.4	Summary	107

8 Strongly Correlated Superconductivity	110
8.1 Introduction	110
8.2 Model	112
8.3 Results	113
8.3.1 Duality of local Green function	113
8.3.2 Local Spectral Function for half-filled system	114
8.3.3 Local spectral function for hole-doped system	116
8.3.4 Quasi-particle weight for half-filled system	119
8.3.5 Renormalized superconducting gap	121
8.4 Summary	123
A High-frequency Expansion of Green Function	124
A.1 Hubbard model	126
A.2 Ionic Hubbard model	127
A.3 Two-orbital Hubbard model	128
Bibliography	131
Abstract in Korean	143
Acknowledgement	147

List of Figures

2.1	Phase diagram for the metal-insulator transition in V_2O_3	6
2.2	Dispersion and DOS of the square lattice	11
2.3	DOS of the atomic Hamiltonian and occupation as a function of the chemical potential	14
2.4	DOS of the infinite-dimensional lattices	15
2.5	Bethe lattice with coordinate number $z = 3$	17
3.1	Schematic diagram of the iterative flows in the DMFT	29
3.2	Examples of the DCA tile shape in the Brillouin-zone of the square lattice	30
3.3	Configuration of the weak coupling algorithm	33
3.4	Configuration of the strong coupling algorithm	37
4.1	Double occupancy and energy density as functions of U at the temperature $T=1/128$	46
4.2	Phase diagram for the Mott transition in the infinite-dimensional Hubbard model	48

4.3	Inverse susceptibility estimated by using numerical derivatives with a finite interval δU for various temperatures	49
4.4	$F(T, U)$ as a function of the interaction strength for various temperatures and $A(T)$ as a function of the temperature	53
4.5	Phase transition line of the infinite-dimensional Hubbard model and comparison with earlier DMFT results	56
4.6	$U_c(T=0)$ obtained from the CTQMC data in the temperature range of $T_L < T < T_H$	58
5.1	Fermi-level spectral weight \tilde{A}_α for $\Delta = 0.5$	67
5.2	Spectral function $A(\omega)$ for $\Delta = 0.5$, $T = 1/128$, and various values of U	69
5.3	Double-occupancy d_O as a function of U	72
5.4	Staggered charge density, $n_B - n_A$ as a function of U	73
5.5	Energy densities as functions of U at temperature $T = 1/128$ and $\Delta = 0.5$	75
5.6	Phase diagram for $\Delta = 0.5$ on the plane of T and U	78
5.7	Total energy density ε as a function of temperature T	81
5.8	Inverse susceptibility χ^{-1} versus temperature T for the various values of staggered lattice potential Δ	82
5.9	Coexistence region for various values of Δ	83
5.10	Phase diagram on the plane of Δ and U at temperature $T = 1/128$	85
6.1	Phase diagrams on the plane of temperature T and interaction strength U for $J = U/16$ and $J = U/4$	90

6.2	Spectral functions calculated via the maximum entropy method and imaginary-part self-energies of wide-orbital electrons at $T =$ $1/200$ for $J/U = 1/16$	94
6.3	Squared magnetic moments of wide-orbital electron as a func- tion of the interaction strength at various temperatures for $J/U =$ $1/16$	96
6.4	Phase diagram on the plane of the interaction strength U and the Hund's coupling strength J/U at temperature $T = 1/200$. .	98
7.1	The phase diagrams obtained from previous studies	101
7.2	Noninteracting energy dispersions and Fermi surface of the bi- layer Hubbard model for $t_{\perp} = 0.8$	104
7.3	The staggered magnetization as a function of t_{\perp} for various val- ues of T and U	105
7.4	The Néel temperature as a function of U for various values of t_{\perp}	106
7.5	Spin-resolved local spectral functions for $U = 4.0$ and $T = 0.05$.	109
8.1	sublattice index for 2-dimensional square lattice	113
8.2	Local duality of Imaginary-time local Green's function for $N_c = 1$	115
8.3	Local duality of Imaginary-time local Green's function for $N_c = 4$	115
8.4	Local spectral function in the half-filled system for $N_c = 1$. . .	117
8.5	Local spectral function in the half-filled system for $N_c = 4$. . .	118
8.6	Local spectral function in the hole-doped system	120
8.7	Quasi-particle weight of the half-filled system as a function of interaction strength U	121

8.8	Coarse-grained superconducting pairing	122
-----	--	-----

List of Tables

2.1	Eigenstates and corresponding energies for the interaction part of the two-orbital Hamiltonian	24
-----	---	----

Chapter 1

Introduction

Strong correlations in electron systems are one of the central subjects in modern condensed matter physics. The electron-electron correlations can give rise to various novel emergent phenomena such as the Mott transition, high- T_c superconductivity, fractional quantum Hall effect, spin liquid, and heavy fermions. It is, however, essentially impossible to consider the entire degrees of freedom and their correlations in real materials because of their complexity. From a theoretical point of view, extracting the most relevant degrees of freedom from real materials and constructing an effective model is an essential and promising choice to study strongly correlated systems. Historically, this approach has made great success in describing various phenomena in the strongly correlated systems via simple models: examples include the BCS model for superconductivity, Kondo model for the Kondo effect, and Anderson model for the disorder-driven metal-insulator transition.

The Hubbard model is a well-known effective model to describe the correlation-driven metal-insulator transition, called the Mott transition [1–3]. It is a very

simple model which considers just two mechanisms, hopping of electrons and mutual Coulomb interactions. Due to its simplicity and a variety of fruitful results, the Hubbard model has been regarded as a cornerstone of strongly correlated electron systems. In spite of its simplicity, solving the Hubbard model is extremely difficult due to its exponentially large Hilbert space. Except for few special cases, the analytic solution of the Hubbard model is not known. Since the Mott transition usually appear when two energy scales, the hopping amplitude and the Coulomb interaction, compete with each other, it is inevitable to resort to non-perturbative numerical approaches.

The dynamical mean-field theory (DMFT) is the first attempt to describe in a non-perturbative unified framework the Mott transition itself and the phases on both sides of the transition [4]. The DMFT approximates the self-energy as a local dynamic quantity in a self-consistent way, which is one of the most important quantities in describing the properties of strongly correlated electrons. This approximation neglects spatial fluctuations of the system but fully incorporates the temporal (quantum) fluctuations. Indeed, in the limit of infinite dimensions, it is known that the spatial fluctuations freeze completely and the approximation becomes exact. The DMFT is known to give an accurate description of the Mott transition in relatively high spatial dimensions.

With the help of the recent development of the computing power and algorithms for numerical calculations, studies beyond the DMFT now become possible. The cluster extensions of the DMFT have recently been introduced to incorporate spatial fluctuations which are completely ignored in the DMFT. The dynamical cluster approximation (DCA) and the cellular DMFT (cDMFT) are

representative examples of cluster extensions; the multi-orbital extension of the DMFT is another direction to enlarge the scope of calculations.

Equipped with such newly developed methods, we investigate more realistic models beyond the simple Hubbard model including another degrees of freedom. Various interesting mechanisms and phenomena in such systems which we call the multi-component systems, are the main subjects of this thesis.

This thesis is organized as follows: Chapter 2 presents the brief theoretical background of the Hubbard model. In Chap. 3, we discuss the DMFT, and its cluster and multi-orbital extensions as numerical methods. In Chap. 4, we apply our numerical method to calculate the first-order transition line in the infinite-dimensional Hubbard model and compare our results with those in existing literature to verify the accuracy of our calculation by the comparison with the previous results. In the remaining part (Chap. 5 to 8), additional degrees of freedom are introduced in the simple Hubbard model and diverse phenomena beyond a simple Mott transition are investigated. Chapter 5 is devoted to the finite-temperature nature of the ionic Hubbard model which corresponds to the Hubbard model in the presence of the staggered lattice potential. Specifically, the correlation effects in the band insulator will be discussed. In Chap. 6, the orbital-selective Mott phase in the multi-orbital Hubbard model is investigated and peculiar thermodynamic properties are described. Chapter 7 deals with the magnetic properties of the bilayer Hubbard model, which exhibits magnetic transitions between two different insulators. Finally, in Chap. 8, the DCA study of the strongly correlated superconductor is presented. In particular, the effects of the mutual interactions in the phe-

nomenological d -wave superconductor are studied.

Chapter 2

Hubbard Model and Strongly Correlated Systems

In the strongly correlated electron systems, the Hubbard model is one of the most popular model. The Hubbard model has a very simple form of Hamiltonian,

$$\mathcal{H} = -t \sum_{\langle ij \rangle \sigma} (c_{i\sigma}^\dagger c_{j\sigma} + h.c.) + U \sum_i n_{i\uparrow} n_{i\downarrow} - \mu \sum_{i\sigma} n_{i\sigma} . \quad (2.1)$$

It consists of the nearest-neighbor hopping t and on-site Coulomb interaction between electrons, U . Here, $c_{i\sigma}(c_{i\sigma}^\dagger)$ is the electron annihilation (creation) operator at site i and μ is chemical potential of the system. In spite of its simple form, the Hubbard model is known to show very rich phases of matters.

In 1963, the Hubbard model is first introduced by Hubbard [1], Kanamori [2], and Gutzwiller [3] independently, to describe the ferromagnetism of the d electrons in the transition metal oxides. After its proposal, the Hubbard model is used as an prototype model to describe the metal-insulator transition driven

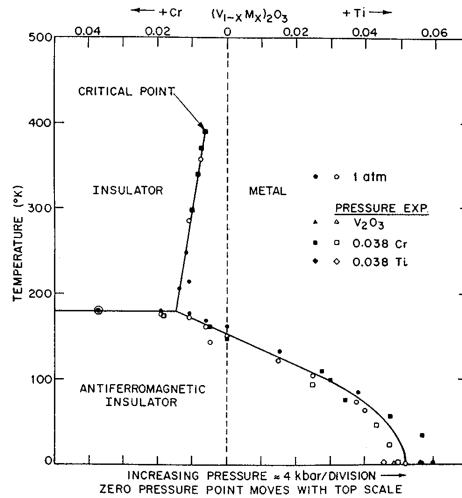


Figure 2.1: Phase diagram for the metal-insulator transition in V_2O_3 as a function of doping with Cr or Ti and as a function of pressure [5].

by the mutual Coulomb interaction, called the Mott transition. V_2O_3 is the representative material which shows the Mott transition. Figure 2.1 shows the temperature-versus-pressure phase diagram of V_2O_3 [5]. Three different phases appear in this phase diagram; paramagnetic insulator at low pressure, paramagnetic metal at high pressure, and antiferromagnetically ordered insulator at low temperature. Here, the pressure controls the hopping amplitude, so the effective interaction strength U/t , can be increased by decreasing the pressure.

In the theoretical point of view, three different approaches have been introduced to describe the Mott transition with the focus on each phase. In 1970, Brinkman and Rice explained the Mott transition as the divergence of the effective mass of itinerant electrons [6]. So electrons lose their itinerant

character at the Mott transition. On the other hand, Hubbard concentrated on the spatially localized states of electrons in the paramagnetic insulator phase, which resides in so-called Hubbard subbands [7]. In this approach, the Mott transition can be viewed as closing of the gap between two Hubbard subbands. And Slater considered the mechanism of the magnetic phase focusing on the role of the mutual Coulomb interaction [8]. Although each of these approaches gives clear mechanism for the Mott transition focusing on one phase of matter, any of these does not give a coherent framework to cover these three phases. The dynamical mean-field theory which is explained in Chap. 3 is the first coherent framework to cover the three different phases.

In addition to the Mott transition, the Hubbard model is related to the diverse phenomena in the condensed matter. The high- T_c superconductivity is one of the most important example. In addition to the rather high transition temperature, the cuprate superconductors show several mysterious phenomena such as d -wave pairing symmetry and pseudo-gap phase. After the discovery of the cuprate superconductor, Anderson pointed out that it is the doped Mott insulator and that two-dimensional Hubbard model is the key to understand cuprate superconductors [9]. Although it is controversial whether the Hubbard model is sufficient to describe the high- T_c superconductivity, the importance of the Coulombic correlation effect and the Hubbard model is a general consensus among researchers.

Recently discovered iron-based superconductors have attracted much academic attentions. Since the iron-based superconductor is believed to be a new example of unconventional superconductor, it is expected that these materials

can give clues to understand the cuprate superconductors. One of the most important difference compared with the cuprate superconductor is multiple-orbital effects. In comparison to the single-band character originating from the $d_{x^2-y^2}$ orbital band in cuprate materials, all of the five orbital bands cross the Fermi levels. In this respect, the multi-orbital Hubbard model is required to study. The research about the multi-orbital Hubbard model is now one of the active fields in modern condensed matter physics.

Following sections are devoted to the description of the basic properties of the Hubbard model. In the first section, the simple derivation of the one-band Hubbard model is given. Important limiting cases and the symmetries are discussed in the next section. Finally, the multi-orbital extension of the Hubbard model is presented in the last section.

2.1 Derivation

The general two-body interacting Hamiltonian can be written as

$$\begin{aligned} \mathcal{H} = & \sum_{\sigma} \int d\mathbf{x} \, \psi_{\sigma}^{\dagger}(\mathbf{x}) \left[-\frac{1}{2m} \nabla^2 + V_1(\mathbf{x}) \right] \psi_{\sigma}(\mathbf{x}) \\ & + \frac{1}{2} \sum_{\sigma\sigma'} \int d\mathbf{x} d\mathbf{x}' \, \psi_{\sigma}^{\dagger}(\mathbf{x}) \psi_{\sigma'}^{\dagger}(\mathbf{x}') V_2(\mathbf{x} - \mathbf{x}') \psi_{\sigma'}(\mathbf{x}') \psi_{\sigma}(\mathbf{x}) , \end{aligned} \quad (2.2)$$

where $V_1(\mathbf{x})$ and $V_2(\mathbf{x} - \mathbf{x}')$ are the one-body and the two-body potential, respectively.

The wave function can be conveniently expanded by the localized Wannier

function basis,

$$\psi_\sigma(\mathbf{x}) = \sum_i \varphi_i(\mathbf{x}) c_{i\sigma} , \quad (2.3)$$

where $\varphi_i(\mathbf{x})$ is the Wannier function localized at the lattice site i . Then the hopping integral, t_{ij} , and the chemical potential, μ , can be defined by the diagonal and the off-diagonal parts of the one-body Hamiltonian

$$t_{ij}(1 - \delta_{ij}) - \mu\delta_{ij} \equiv \int d\mathbf{x} \varphi_i^*(\mathbf{x}) \left[-\frac{1}{2m} \nabla^2 + V_1(\mathbf{x}) \right] \varphi_j(\mathbf{x}) . \quad (2.4)$$

For the model of narrow-band electrons such as d or f -orbital electrons, the Wannier functions are well-localized and the electrons are tightly bound at the i lattice site. In the circumstances, the most dominant terms of the Hamiltonian are the nearest-neighbor hopping and on-site two-body interactions. By defining the on-site Coulomb interaction as

$$U \equiv \int d\mathbf{x} d\mathbf{x}' |\varphi_i(\mathbf{x})|^2 V_2(\mathbf{x} - \mathbf{x}') |\varphi_i(\mathbf{x}')|^2, \quad (2.5)$$

We can reduce the Hamiltonian to

$$\mathcal{H} = -t \sum_{\langle ij \rangle \sigma} (c_{i\sigma}^\dagger c_{j\sigma} + h.c.) + U \sum_i n_{i\uparrow} n_{i\downarrow} - \mu \sum_{i\sigma} n_{i\sigma} . \quad (2.6)$$

Here, nearest-neighbor-hopping integral is denoted as constant t . This is the celebrated form of the one-band Hubbard model.

2.2 Limiting cases

The interesting phenomena of the Hubbard model emerge when the energy scales compete with each other. In other words, the hopping amplitude t and the mutual Coulomb interaction U are comparable to each other. In the intermediate-parameter region, the nature of the Hubbard model depends on the details of model, such as lattice structure and dimensionality. However, some limiting cases are independent of the details of the system. In the following, some limiting cases will be discussed.

2.2.1 Noninteracting limit

The first limiting case of the Hubbard model is the noninteracting limit where the mutual Coulomb interaction strength vanishes ($U = 0$). Then the Hubbard model becomes the tight-binding model

$$\mathcal{H}_0 = -t \sum_{\langle ij \rangle \sigma} \left(c_{i\sigma}^\dagger c_{j\sigma} + h.c. \right) . \quad (2.7)$$

With the help of the translational invariance, the tight-binding Hamiltonian can be diagonalized by Fourier transformation,

$$c_i = \frac{1}{N} \sum_{\mathbf{k}} c_{\mathbf{k}} e^{i\mathbf{k} \cdot \mathbf{x}_i} , \quad (2.8)$$

where N is the number of the lattice sites. The resulting diagonalized Hamiltonian is

$$\mathcal{H}_0 = \sum_{\mathbf{k}} \varepsilon_{\mathbf{k}} c_{\mathbf{k}\sigma}^\dagger c_{\mathbf{k}\sigma} , \quad (2.9)$$

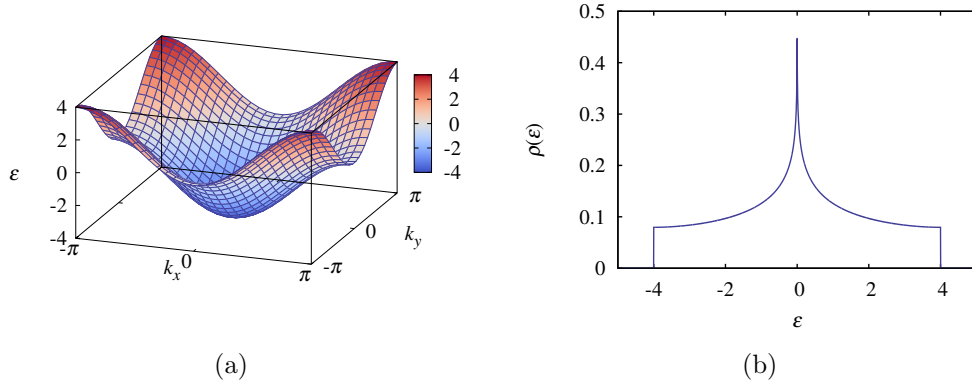


Figure 2.2: (a) Dispersion and (b) DOS of the square lattice.

and the momentum dependence of $\varepsilon_{\mathbf{k}}$ depends on the underlying lattice structure.

As a representative example, the square lattice will be considered. In the square lattice, the energy dispersion has the form of

$$\varepsilon_{\mathbf{k}} = -2t(\cos k_x + \cos k_y) , \quad (2.10)$$

which is shown in Fig. 2.2(a).

The density of states (DOS) of the square lattice,

$$\rho(\varepsilon) = \frac{1}{N} \sum_{\mathbf{k}} \delta(\varepsilon - \varepsilon_{\mathbf{k}}) , \quad (2.11)$$

can be expressed as a closed form by the analytic calculation. Using the 4-fold symmetry of the energy dispersion in the Brillouin zone, we obtain

$$\rho(\varepsilon) = 4 \int_0^\pi \frac{dk_x}{2\pi} \int_0^\pi \frac{dk_y}{2\pi} \delta(\varepsilon + 2t(\cos k_x + \cos k_y)) . \quad (2.12)$$

Defining $x = \cos k_x$, $y = \cos k_y$, and $\tilde{\varepsilon} = \varepsilon/2t$,

$$\begin{aligned}\rho(2t\tilde{\varepsilon}) &= \frac{1}{2t\pi^2} \int_{-1}^1 dx \int_{-1}^1 dy \frac{\delta(\tilde{\varepsilon} + x + y)}{\sqrt{(1-x^2)(1-y^2)}} \\ &= \frac{1}{2t\pi^2} \begin{cases} \int_{-1}^{1-\tilde{\varepsilon}} dx f(x), & 2 > \tilde{\varepsilon} \geq 0 \\ \int_{1+\tilde{\varepsilon}}^1 dx f(x), & -2 < \tilde{\varepsilon} < 0 \\ 0, & \text{otherwise} \end{cases},\end{aligned}\quad (2.13)$$

where

$$f(x) = \frac{1}{\sqrt{(1-x^2)(1-(\tilde{\varepsilon}+x)^2)}}. \quad (2.14)$$

By the change of the variable

$$x = -(1 + \tilde{\varepsilon}) + \frac{2\tilde{\varepsilon}}{2 - (2 - \tilde{\varepsilon}) \sin^2 \varphi}, \quad (2.15)$$

the DOS becomes

$$\rho(2t\tilde{\varepsilon}) = \frac{1}{2t\pi^2} \theta(2 - |\tilde{\varepsilon}|) \int_0^{\pi/2} \frac{d\varphi}{\sqrt{1 - m \sin^2 \varphi}} \quad (2.16)$$

for $0 < \tilde{\varepsilon} < 2$. Here, $m = 1 - \frac{\tilde{\varepsilon}^2}{4}$. Using the fact that $\rho(\varepsilon) = \rho(-\varepsilon)$, we can obtain the DOS of the square lattice,

$$\rho(\varepsilon) = \frac{1}{2\pi^2 t} \theta(4t - |\varepsilon|) K \left(1 - \frac{\varepsilon^2}{16t^2} \right), \quad (2.17)$$

where $K(x)$ is the complete elliptic integral of the first kind. Figure. 2.2 shows the DOS of the square lattice in the unit of t . The characteristic Van Hove singularity is observed at $\varepsilon = 0$.

2.2.2 Atomic limit

Another limit of the Hubbard model is the atomic limit where $t = 0$. The atomic limit corresponds to the strong interaction limit where U/t becomes infinite. Then the Hamiltonian becomes

$$\mathcal{H}_U = U \sum_i n_{i\uparrow} n_{i\downarrow} + \varepsilon_0 \sum_i n_i , \quad (2.18)$$

where $n_i = n_{i\uparrow} + n_{i\downarrow}$. Since the Hamiltonian consists only of the local density operators, the local occupation number is a good quantum number. When the first electron is created at empty site i , it has the energy of ε_0 . Adding another electron to the site i which is occupied by the electron with different spin, the two electrons in site i have $U + 2\varepsilon_0$ energy. It can be interpreted as meaning that the second electron is added to the state with the energy $U + \varepsilon_0$. Since the resulting many-body state is the product state of local eigenstates, the DOS of the system is simply the sum of two delta functions

$$\rho(\varepsilon) = \frac{1}{2} [\delta(\varepsilon - \varepsilon_0) + \delta(\varepsilon - (\varepsilon_0 + U))] , \quad (2.19)$$

which is shown in Fig. 2.3(a). Each level has N degeneracy. As we increase the chemical potential μ , the occupancy of the system increases as in Fig. 2.3(b) at zero temperature.

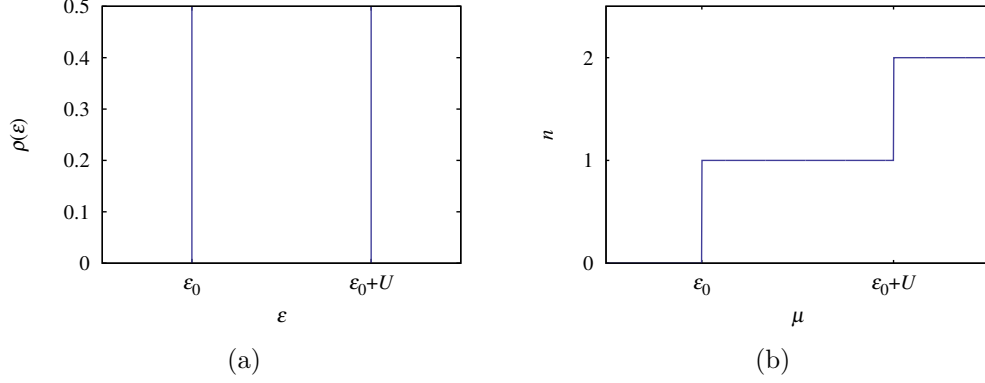


Figure 2.3: (a) DOS of the atomic Hamiltonian. (b) Occupation as a function of the chemical potential.

2.2.3 Infinite dimensions

The limit of infinite dimensions is a very useful theoretical tool since the mean-field theory becomes exact in this limit. In the Hubbard model, however, it is tricky to make the appropriate limit of infinite dimensions due to the different dimensional-scaling behavior of the constituting terms. For the noninteracting Hamiltonian, the kinetic energy scales by $\sqrt{2D}$ while the Coulomb interaction term does not scale, where D is the spatial dimension of the system. As an example, the variation of the kinetic energy of the half-filled system on the hypercubic lattice at zero temperature,

$$\begin{aligned}
\frac{1}{N} \sum_{\mathbf{k}} \epsilon_{\mathbf{k}}^2 &= \int_{-\pi}^{\pi} \frac{dk_n}{2\pi} \left(-2t \sum_{n=1}^D \cos k_n \right)^2 \\
&= 4t^2 \int_{-\pi}^{\pi} \frac{dk_n}{2\pi} \left(\sum_{n=1}^D \cos^2 k_n + \sum_{n \neq m}^D \cos k_n \cos k_m \right) \\
&= 2Dt^2 .
\end{aligned} \tag{2.20}$$

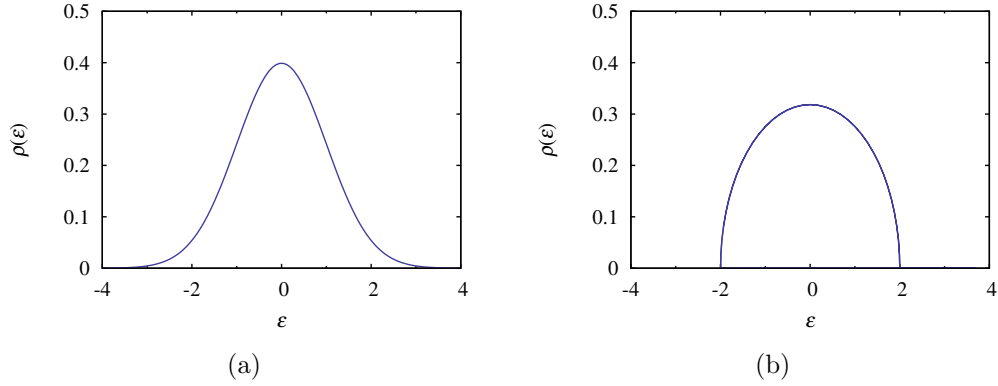


Figure 2.4: DOS of (a) hypercubic lattice and (b) Bethe lattice in the limit of infinite dimensions.

As a result, we observe that the kinetic energy scales by $\sqrt{2D}$. For a non-trivial model where the kinetic energy and Coulomb interaction energy compete with each other, the hopping amplitude, t^* , should scale as $1/\sqrt{2D}$,

$$t^* = \frac{t}{\sqrt{2D}} . \quad (2.21)$$

In the limit of infinite dimensions, we can obtain the DOS analytically for the several lattices. We consider two representative lattices, the hypercubic lattice and the Bethe lattice.

hypercubic lattice

The hypercubic lattice is a generalization of the three-dimensional cubic lattice in arbitrary dimension. In the D -dimensional hypercubic lattice, the DOS of

the system can be written by

$$\rho(\varepsilon) = \prod_{n=1}^D \int_{-\pi}^{\pi} \frac{dk_n}{2\pi} \delta(\varepsilon - \varepsilon_{\mathbf{k}}) , \quad (2.22)$$

where $\varepsilon_{\mathbf{k}}$ is the noninteracting dispersion

$$\varepsilon_{\mathbf{k}} = -2t^* \sum_{n=1}^D \cos k_n . \quad (2.23)$$

Then its Fourier transformation is

$$\begin{aligned} \Phi(s) &= \int_{-\infty}^{\infty} d\varepsilon \rho(\varepsilon) e^{is\varepsilon} = \left[\int_{-\pi}^{\pi} \frac{dk}{2\pi} e^{-2ist^* \cos k} \right]^D \\ &= (J_0(2st^*))^D , \end{aligned} \quad (2.24)$$

where $J_0(x)$ is the zeroth-order Bessel function of the first kind. Using the fact that $J_0(x)$ has a peak at $x = 0$, we can expand in the order of st^* which scales by $1/\sqrt{2D}$. Then,

$$\Phi(s) = \exp \left(-\frac{(st)^2}{2} - \frac{(st)^4}{16D} + \mathcal{O}(D^{-2}) \right) . \quad (2.25)$$

In the infinite dimensions, the corresponding inverse Fourier transformation is the Gaussian distribution

$$\rho(\varepsilon) = \frac{1}{\sqrt{2\pi t^2}} \exp \left(-\frac{\varepsilon^2}{2t^2} \right) , \quad (2.26)$$

which is the DOS of the hypercubic lattice. Figure 2.4(a) represents the DOS of the hypercubic lattice.

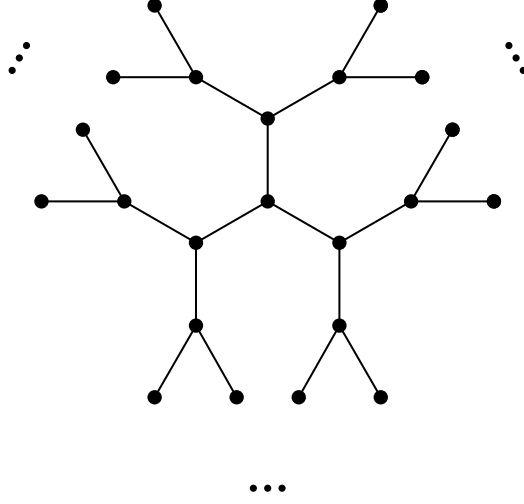


Figure 2.5: Bethe lattice with coordinate number $z = 3$.

Bethe lattice

Another useful theoretical lattice is a Bethe lattice, which is shown in Fig. 2.5. By the same scaling argument, the hopping amplitude in Bethe lattice should scales by

$$t^* = \frac{t}{\sqrt{z}} . \quad (2.27)$$

The DOS of the Bethe lattice can be derived under the Green function formalism, called a cavity method. In the tight-binding Hamiltonian, the action

of the system can be split into three parts,

$$\begin{aligned}
S &= S_o + S_\Delta + S^{(o)} , \\
S_o &= \int_0^\beta d\tau \, c_o^\dagger \partial_\tau c_o , \\
S_\Delta &= - \int_0^\beta d\tau \, t^* \sum_{\langle i,o \rangle} \left(c_o^\dagger c_i + c_i^\dagger c_o \right) , \\
S^{(o)} &= \int_0^\beta d\tau \, \left(\sum_{i \neq o} c_i^\dagger \partial_\tau c_i - t^* \sum_{\langle ij \rangle \neq o} c_i^\dagger c_j \right) . \tag{2.28}
\end{aligned}$$

S_o and $S^{(o)}$ are the local action at site o and the bath action, respectively. And S_Δ is the hybridization term between the site o and the bath sites. Performing the Gaussian integral over the Grassmann variables, c_i^\dagger and c_i , where $i \neq o$, we can get the relation of the Green function,

$$\begin{aligned}
G_{oo}^{-1}(i\omega) &= i\omega - (t^*)^2 \sum_{\langle ij,o \rangle} G_{ij}^{(o)}(i\omega_n) \\
&= i\omega - (t^*)^2 \sum_{\langle i,o \rangle} G_{ii}^{(o)}(i\omega_n) . \tag{2.29}
\end{aligned}$$

Here, G_{oo} and $G_{ij}^{(o)}$ are the Green functions of the site o and of the sites i, j for the cavity action in which the lattice site o is removed. On the second line, i and j site are identified due to the property of the Bethe lattice, where two nearest neighbor sites of o are completely disconnected when the o site is removed. Since the removal of the o site does not change the local Green

function of i site due to the infinite connectivity,

$$G_{ii}^{(o)}(i\omega_n) = G_{oo}(i\omega_n) . \quad (2.30)$$

By the analytic continuation, $i\omega_n \rightarrow \omega + i\eta$ after solving the second order equation of G_{oo} , we can obtain the local Green function in real frequency,

$$\begin{aligned} G(\omega) &\equiv G_{oo}(\omega) \\ &= \frac{\omega - \sqrt{\omega^2 - 4(t^*)^2 z}}{2(t^*)^2 z} . \end{aligned} \quad (2.31)$$

Finally, the DOS of the infinite-dimensional Bethe lattice becomes

$$\begin{aligned} \rho(\varepsilon) &= -\frac{1}{\pi} \text{Im} G(\varepsilon) \\ &= \frac{\theta(2t - |\varepsilon|)}{\pi t} \sqrt{1 - \left(\frac{\varepsilon}{2t}\right)^2} . \end{aligned} \quad (2.32)$$

The form of the DOS is semi-circular and shown in Fig. 2.4(b).

2.3 Symmetries

The Hubbard model intrinsically has some useful symmetries. In the sense of numerical calculation, these symmetries can help to reduce significantly the cost of the calculations,

2.3.1 Spin-rotational symmetry

The Hubbard model intrinsically has a spin-rotational symmetry. For spin-1/2 electrons, the Pauli matrices are the generators of the spin-rotational symmetry

operation. Since the tight-binding and the chemical potential terms can be represented by

$$-t \sum_{\langle ij \rangle} (c_{i\uparrow}^\dagger c_{i\downarrow}^\dagger) \mathbb{I}_{2 \times 2} \begin{pmatrix} c_{j\uparrow} \\ c_{j\downarrow} \end{pmatrix}, \quad (2.33)$$

and

$$-\mu \sum_i (c_{i\uparrow}^\dagger c_{i\downarrow}^\dagger) \mathbb{I}_{2 \times 2} \begin{pmatrix} c_{i\uparrow} \\ c_{i\downarrow} \end{pmatrix}, \quad (2.34)$$

respectively, it is obvious that these terms are invariant under the spin rotation.

On the other hand, the mutual interaction term is represented by

$$\begin{aligned} n_{i\downarrow} n_{i\uparrow} &= n_{i\uparrow} - S_i^+ S_i^- \\ &= n_{i\downarrow} - S_i^- S_i^+ \\ &= \frac{n_i}{2} - 2(S_i^z)^2, \end{aligned} \quad (2.35)$$

where $S^+ = c_\uparrow^\dagger c_\downarrow$, $S^- = c_\downarrow^\dagger c_\uparrow$, $S^\alpha = \frac{1}{2} \sum_{ab} c_a^\dagger \sigma_{ab}^{(\alpha)} c_b$, and $\sigma^{(\alpha)}$ is Pauli matrices with $\alpha = x, y, z$. Averaging three expressions of the right-hand sides in Eqn. (2.35), we can get the expression

$$n_{i\uparrow} n_{i\downarrow} = \frac{n_i}{2} - \frac{2}{3} \mathbf{S}_i^2, \quad (2.36)$$

where we have used the identity

$$S_i^+ S_i^- + S_i^- S_i^+ = 2[(S_i^x)^2 + (S_i^y)^2]. \quad (2.37)$$

Since n_i and \mathbf{S}_i^2 are spin-rotationally invariant terms, we can conclude that the

Hubbard Hamiltonian has the spin-rotationally symmetry.

2.3.2 Particle-hole symmetry

In the bipartite lattice, the Hubbard model has a particle-hole symmetry when $\mu = U/2$. Considering the particle-hole transformation,

$$\begin{pmatrix} c_{A\sigma} \\ c_{B\sigma} \end{pmatrix} \rightarrow \begin{pmatrix} c_{A\sigma}^\dagger \\ -c_{B\sigma}^\dagger \end{pmatrix}, \quad (2.38)$$

each term in Eqn. (2.6) is transformed into

$$\begin{aligned} -t(c_{A\sigma}^\dagger c_{B\sigma} + c_{B\sigma}^\dagger c_{A\sigma}) &\rightarrow -t(c_{B\sigma}^\dagger c_{A\sigma} + c_{A\sigma}^\dagger c_{B\sigma}) \\ U n_{i\uparrow} n_{i\downarrow} &\rightarrow U(n_{i\uparrow} n_{i\downarrow} - n_{i\uparrow} - n_{i\downarrow} + 1) \\ -\mu n_{i\sigma} &\rightarrow -\mu(1 - n_{i\sigma}). \end{aligned} \quad (2.39)$$

When $\mu = U/2$, the Hubbard model is invariant under the particle-hole transformation up to a constant,

$$\mathcal{H} \rightarrow \mathcal{H} + \frac{UN}{2}, \quad (2.40)$$

where N is total particle number in the system.

2.4 Multi-orbital Hubbard model

One of the most important extensions of the single band Hubbard is the examination of the multiple orbital effects. In the following section, the derivation of the multi-orbital Hubbard model will be discussed.

In the multi-orbital system, the general two-body interacting Hamiltonian can be written as

$$\begin{aligned}\mathcal{H} = & \sum_{\sigma} \int d\mathbf{x} \psi_{\sigma}^{\dagger}(\mathbf{x}) \left[-\frac{1}{2m} \nabla^2 + V_1(\mathbf{x}) \right] \psi_{\sigma}(\mathbf{x}) \\ & + \frac{1}{2} \sum_{\sigma\sigma'} \int d\mathbf{x} d\mathbf{x}' \psi_{\sigma}^{\dagger}(\mathbf{x}) \psi_{\sigma'}^{\dagger}(\mathbf{x}') V_2(\mathbf{x} - \mathbf{x}') \psi_{\sigma'}(\mathbf{x}') \psi_{\sigma}(\mathbf{x}) .\end{aligned}\quad (2.41)$$

It is useful to expand the wave function based on the Wannier function basis,

$$\psi_{\sigma}(\mathbf{x}) = \sum_{i\alpha} \varphi_{i\alpha}(\mathbf{x}) c_{i\alpha\sigma} . \quad (2.42)$$

Here, $\varphi_{i\alpha}(\mathbf{x})$ is the α orbital Wannier function localized at the lattice site i . Then the hopping integral, $t_{ij}^{\alpha\alpha'}$ and the chemical potential, μ_{α} can be defined as the diagonal and off-diagonal parts of the first term of the Hamiltonian,

$$t_{ij}^{\alpha\alpha'} (1 - \delta_{ij}) - \mu_{\alpha} \delta_{\alpha\alpha'} \delta_{ij} \equiv \int d\mathbf{x} \varphi_{i\alpha}^*(\mathbf{x}) \left[-\frac{1}{2m} \nabla^2 + V_1(\mathbf{x}) \right] \varphi_{j\alpha'}(\mathbf{x}) . \quad (2.43)$$

If we assume the Wannier function of d orbital as the spherical harmonics with $l = 2$, the only non-vanishing integrals are

$$\begin{aligned}U_{\alpha\alpha'} & \equiv \int d\mathbf{x} d\mathbf{x}' |\varphi_{i\alpha}(\mathbf{x})|^2 V_2(\mathbf{x} - \mathbf{x}') |\varphi_{i\alpha'}(\mathbf{x}')|^2, \\ J_{\alpha\alpha'} & \equiv \int d\mathbf{x} d\mathbf{x}' \varphi_{i\alpha}^*(\mathbf{x}) \varphi_{i\alpha'}^*(\mathbf{x}') V_2(\mathbf{x} - \mathbf{x}') \varphi_{i\alpha}(\mathbf{x}') \varphi_{i\alpha'}(\mathbf{x}) \quad (\alpha \neq \alpha'), \\ J'_{\alpha\alpha'} & \equiv \int d\mathbf{x} d\mathbf{x}' \varphi_{i\alpha}^*(\mathbf{x}) \varphi_{i\alpha'}^*(\mathbf{x}') V_2(\mathbf{x} - \mathbf{x}') \varphi_{i\alpha'}(\mathbf{x}') \varphi_{i\alpha}(\mathbf{x}) \quad (\alpha \neq \alpha').\end{aligned}\quad (2.44)$$

The remaining part of mutual interaction Hamiltonian is

$$\begin{aligned}
& \sum_{i\alpha} U_{\alpha\alpha} n_{i\alpha\uparrow} n_{i\alpha\downarrow} \\
& + \sum_{i,\alpha<\alpha',\sigma} [U_{\alpha\alpha'} n_{i\alpha\sigma} n_{i\alpha'\bar{\sigma}} + (U_{\alpha\alpha'} - J_{\alpha\alpha'}) n_{i\alpha\sigma} n_{i\alpha'\sigma}] \\
& + \sum_{i,\alpha\neq\alpha'} J_{\alpha\alpha'} c_{i\alpha\uparrow}^\dagger c_{i\alpha'\downarrow}^\dagger c_{i\alpha\downarrow} c_{i\alpha'\uparrow} \\
& + \sum_{i,\alpha\neq\alpha'} J'_{\alpha\alpha'} c_{i\alpha\uparrow}^\dagger c_{i\alpha\downarrow}^\dagger c_{i\alpha'\downarrow} c_{i\alpha'\uparrow} .
\end{aligned} \tag{2.45}$$

If we further assume that the overlap integral of the Wannier function is only finite within the nearest-neighbor lattice sites, the final form of the multi-orbital extension of the Hubbard Hamiltonian is

$$\begin{aligned}
\mathcal{H} &= \mathcal{H}_0 + \mathcal{H}_{\text{int}} , \\
\mathcal{H}_0 &= \sum_{\langle ij \rangle} \sum_{\alpha\alpha'\sigma} t_{ij}^{\alpha\alpha'} c_{i\alpha\sigma}^\dagger c_{j\alpha'\sigma} - \sum_{i\alpha\sigma} \mu_\alpha n_{i\alpha\sigma} , \\
\mathcal{H}_{\text{int}} &= U \sum_{i\alpha} n_{i\alpha\uparrow} n_{i\alpha\downarrow} + \sum_{i,\alpha<\alpha',\sigma} [U' n_{i\alpha\sigma} n_{i\alpha'\bar{\sigma}} + (U' - J) n_{i\alpha\sigma} n_{i\alpha'\sigma}] , \\
&+ J \sum_{i,\alpha<\alpha'} \left(c_{i\alpha\uparrow}^\dagger c_{i\alpha'\downarrow}^\dagger c_{i\alpha\downarrow} c_{i\alpha'\uparrow} + c_{i\alpha\uparrow}^\dagger c_{i\alpha\downarrow}^\dagger c_{i\alpha'\downarrow} c_{i\alpha'\uparrow} + h.c. \right) .
\end{aligned} \tag{2.46}$$

This form of the Hamiltonian has a spin-rotational $SU(2)$ symmetry. By introducing the spin operator,

$$S_{i\alpha}^a \equiv \frac{1}{2} \sum_{ss'} c_{i\alpha s}^\dagger \sigma_{ss'}^a c_{i\alpha s'} , \tag{2.47}$$

with $a = x, y, z$, the symmetry can be explicitly shown in the form of the

$SU(2)$		Ising	
eigenstate	energy	eigenstate	energy
$ \uparrow; \uparrow\rangle$	$U' - J$	$ \uparrow; \uparrow\rangle$	$U' - J$
$ \downarrow; \downarrow\rangle$	$U' - J$	$ \downarrow; \downarrow\rangle$	$U' - J$
$\frac{1}{\sqrt{2}}(\uparrow; \downarrow\rangle + \downarrow; \uparrow\rangle)$	$U' - J$	$\frac{1}{\sqrt{2}}(\uparrow; \downarrow\rangle + \downarrow; \uparrow\rangle)$	$U' + J$
$\frac{1}{\sqrt{2}}(\uparrow; \downarrow\rangle - \downarrow; \uparrow\rangle)$	$U' + J$	$\frac{1}{\sqrt{2}}(\uparrow; \downarrow\rangle - \downarrow; \uparrow\rangle)$	$U' + J$
$\frac{1}{\sqrt{2}}(\uparrow\downarrow; 0\rangle - 0; \downarrow\uparrow\rangle)$	$U - J$	$\frac{1}{\sqrt{2}}(\uparrow\downarrow; 0\rangle - 0; \downarrow\uparrow\rangle)$	U
$\frac{1}{\sqrt{2}}(\uparrow\downarrow; 0\rangle + 0; \downarrow\uparrow\rangle)$	$U + J$	$\frac{1}{\sqrt{2}}(\uparrow\downarrow; 0\rangle + 0; \downarrow\uparrow\rangle)$	U

Table 2.1: Eigenstates and corresponding energies for the interaction part of the two-orbital Hamiltonian. Only the half-filled sector of the Hamiltonian is represented.

Hamiltonian,

$$\begin{aligned}
\mathcal{H}_{\text{int}} = & \frac{U}{2} \sum_i \left[\left(\sum_{\alpha} n_{i\alpha} \right)^2 - \sum_{\alpha} n_{i\alpha} \right] - \frac{5J}{2} \sum_{i, \alpha < \alpha'} n_{i\alpha} n_{i\alpha'} \\
& - 2J \sum_{i, \alpha < \alpha'} \mathbf{S}_{i\alpha} \cdot \mathbf{S}_{i\alpha'} + \frac{J}{2} \sum_{i, \alpha \neq \alpha'} \left(\sum_{\sigma} c_{i\alpha\sigma}^{\dagger} c_{i\alpha'\sigma} \right)^2. \quad (2.48)
\end{aligned}$$

2.4.1 Hund's coupling

The role of the Hund's coupling is explicitly shown in Eqn. (2.48). The term $-2J \sum_{i, \alpha < \alpha'} \mathbf{S}_{i\alpha} \cdot \mathbf{S}_{i\alpha'}$ prefers the maximized total spin-angular momentum reflecting the famous Hund's first rule. This property can be clearly shown from the atomic eigenstates of the interacting part of the Hamiltonian, Eqn. (2.48). For the half-filled sector of the two-orbital model, the eigenstates are listed with their energy in the left column of Table 2.1.

Ising-type Hund's coupling

During the derivation of the multi-orbital Hubbard model, we have assumed the $SU(2)$ spin-rotational symmetry of the system and as a result, the Hund's coupling also has the form of spin-rotational symmetry. If we imagine the symmetry breaking of the spin space, however, the form of the Hund's coupling becomes

$$- 2J \sum S_z S_z - 2J' \sum (S_x S_x + S_y S_y) . \quad (2.49)$$

For the case $J > J'$, it was shown that J' is irrelevant in the low-energy effective Hamiltonian by the poor man's scaling of Kondo model [10]. Following this argument, the form of the Hamiltonian becomes

$$\begin{aligned} \mathcal{H} = & \sum_{\langle ij \rangle} \sum_{\alpha\alpha'\sigma} t_{ij}^{\alpha\alpha'} c_{i\alpha\sigma}^\dagger c_{j\alpha\sigma} - \sum_{i\alpha\sigma} \mu_\alpha n_{i\alpha\sigma} , \\ & + U \sum_{i\alpha} n_{i\alpha\uparrow} n_{i\alpha\downarrow} + \sum_{i,\alpha<\alpha',\sigma} [U' n_{i\alpha\sigma} n_{i\alpha'\bar{\sigma}} + (U' - J) n_{i\alpha\sigma} n_{i\alpha\sigma}] , \end{aligned} \quad (2.50)$$

and it is called multi-orbital Hubbard model with Ising-type Hund's coupling.

Ising-type Hund's coupling exhibits different atomic levels. The eigenstate of the half-filled sector is shown in the right column of Table 2.1. The difference in the ground states could result in different physical properties of the system.

Chapter 3

Numerical Methods

3.1 Dynamical Mean-Field Theory

The dynamical mean-field theory (DMFT) is a coherent framework to describe various energy scales in strongly correlated electron systems. Since it fully incorporates local quantum (temporal) fluctuation, it has been regarded as an appropriate tool for strongly correlated electron systems.

The Hubbard model is a representative example of the model to which the DMFT is applied successfully. The model Hamiltonian is written as

$$\mathcal{H} = -t \sum_{\langle ij \rangle \sigma} (c_{i\sigma}^\dagger c_{j\sigma} + h.c.) + U \sum_i n_{i\uparrow} n_{i\downarrow} . \quad (3.1)$$

Within the DMFT, the Hubbard model on the lattice is mapped onto the quantum impurity model which is defined by

$$\mathcal{H}_{\text{QI}} = \mathcal{H}_{\text{loc}} + \mathcal{H}_{\text{hyb}} + \mathcal{H}_{\text{bath}}, \quad (3.2)$$

where

$$\mathcal{H}_{\text{loc}} \equiv U n_{o\uparrow} n_{o\downarrow} - \mu \sum_{\sigma} n_{o\sigma} , \quad (3.3)$$

$$\mathcal{H}_{\text{hyb}} \equiv \sum_{\mathbf{p}\sigma} (V_{\mathbf{p}\sigma} a_{\mathbf{p}\sigma}^{\dagger} c_{o\sigma} + V_{\mathbf{p}\sigma}^* c_{o\sigma}^{\dagger} a_{\mathbf{p}\sigma}) , \quad (3.4)$$

$$\mathcal{H}_{\text{bath}} \equiv \sum_{\mathbf{p}\sigma} \varepsilon_{\mathbf{p}} a_{\mathbf{p}\sigma}^{\dagger} a_{\mathbf{p}\sigma} . \quad (3.5)$$

Here, $c_{o\sigma}$ is an annihilation operator of spin- σ electron at the impurity site and $a_{\mathbf{p}\sigma}$ is that of spin- σ electron at the bath of the index \mathbf{p} . Note that $V_{\mathbf{p}\sigma}$ and $\varepsilon_{\mathbf{p}}$ are auxiliary parameters which can be determined in a self-consistent way. In the noninteracting case, $U = 0$, the Green function of the impurity electron, called Weiss function, is written as

$$\mathcal{G}_{0\sigma}^{-1}(i\omega_n) = i\omega_n + \mu - \sum_k \frac{|V_{\mathbf{p}\sigma}|^2}{i\omega_n - \varepsilon_{\mathbf{p}}} , \quad (3.6)$$

which plays the role of Weiss fields. The information of auxiliary parameters are encoded in this function. Then the effective action for the impurity electron becomes

$$S_{\text{eff}} = - \sum_{\sigma} \int_0^{\beta} d\tau' \int_0^{\beta} d\tau c_{o\sigma}^{\dagger}(\tau) \mathcal{G}_{0\sigma}^{-1}(\tau - \tau') c_{o\sigma}(\tau') + U \int_0^{\beta} d\tau n_{o\uparrow}(\tau) n_{o\downarrow}(\tau) . \quad (3.7)$$

Now, the lattice problem is transformed into the impurity problem with the effective action. Several methods have been developed to solve the latter effective action and these are called impurity solvers. Impurity solvers, which are known to be very accurate, are (continuous-time) quantum Monte Carlo

(QMC) method, exact diagonalization (ED), numerical renormalization group (NRG), and so on. Particularly, the continuous-time quantum Monte Carlo (CTQMC) method will be explained in great detail.

After obtaining the interacting impurity Green function of the effective action, $\mathcal{G}(i\omega_n)$, by using the impurity solver, the impurity self-energy is extracted by Dyson's equation,

$$\Sigma_{\text{imp}}(i\omega_n) = \mathcal{G}_0^{-1}(i\omega_n) - \mathcal{G}^{-1}(i\omega_n) . \quad (3.8)$$

Note that the self-energy is a local, namely, momentum independent quantity due to the local nature of the effective action. This is the formal definition of the DMFT, which states that the self-energy of the original lattice model is momentum independent quantity and that it is the same with the impurity self-energy,

$$\Sigma(\mathbf{k}, i\omega_n) = \Sigma_{\text{imp}}(i\omega_n) . \quad (3.9)$$

To adjust the auxiliary parameters of the quantum impurity model, we need the self-consistency relation which equates the given self-energy with the updated Weiss function,

$$\mathcal{G}_0^{-1}(i\omega_n) = \left(\frac{1}{N} \sum_{\mathbf{k}} \frac{1}{i\omega_n - \epsilon_{\mathbf{k}} + \mu - \Sigma(i\omega_n)} \right)^{-1} + \Sigma(i\omega_n) . \quad (3.10)$$

Here, the quantity in the parenthesis is a local Green function, which is the momentum sum of lattice Green function,

$$G(\mathbf{k}, i\omega_n) = \frac{1}{i\omega_n - \epsilon_{\mathbf{k}} + \mu - \Sigma(i\omega_n)} . \quad (3.11)$$

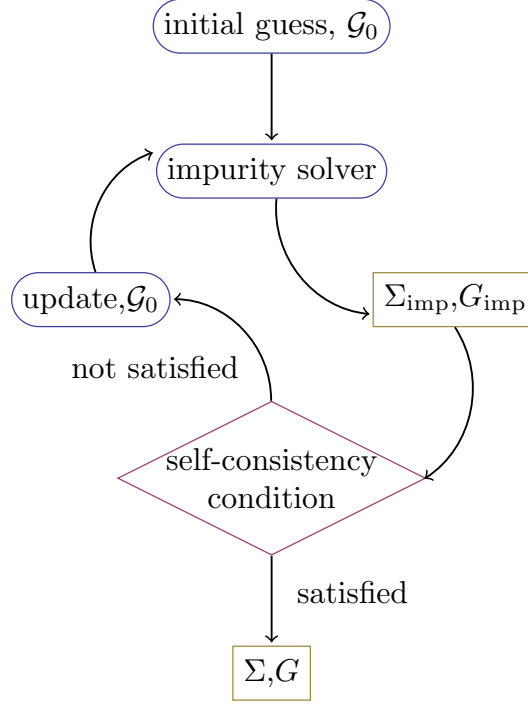


Figure 3.1: Schematic diagram of the iterative flows in the DMFT. The lattice information is used in the self-consistency relation.

The information of a lattice structure is reflected in the momentum-dependent noninteracting single-particle energy $\epsilon_{\mathbf{k}}$. Equation (3.10) closes the loop of the DMFT and successive iterations determine the self-energy in a self-consistent way.

3.2 Dynamical Cluster Approximation

The central approximation of the DMFT is that the self-energy is a momentum independent quantity. This implies that the spatial fluctuation of the system is

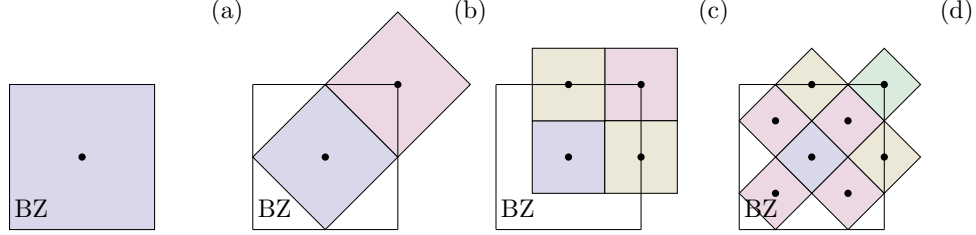


Figure 3.2: Examples of the DCA tile shape in the Brillouin-zone of the square lattice. Cluster size, N_c is (a) 1, (b) 2, (c) 4, (d) 8. $N_c = 1$ corresponds to the DMFT case. The black dots are the coarse-grained momentum value, \mathbf{K} .

suppressed within a mean-field theory. In low-dimensional systems, however, it is known that the spatial fluctuation and corresponding momentum space anisotropy plays a central role in strongly correlated electron systems.

To incorporate the spatial fluctuation, several cluster extensions of the DMFT have been introduced. Two of the representative examples are the cellular DMFT (cDMFT) and the dynamical cluster approximation (DCA).

The DCA introduces the momentum dependence into the self-energy in a systematic way. Within the DCA, the Brillouin zone (BZ) of the lattice is divided into a finite number of tiles, usually denoted as N_c . Some examples are demonstrated in Fig. 3.2. Then we can consider the variation of the self-energy between the tiles even though the self-energy is assumed to be the same within each tile. Formally,

$$\Sigma(\mathbf{k}, i\omega_n) \sim \Sigma(\mathbf{K}, i\omega_n) , \quad (3.12)$$

where \mathbf{K} represents the momentum of the BZ tile.

The tiling in the BZ constitutes the translationally invariant cluster in the

real space. This is the characteristic feature of the DCA compared with the cDMFT.

3.3 Continuous-Time Quantum Monte Carlo method

The basic idea of the continuous-time quantum Monte Carlo method (CTQMC) is the stochastic sampling of perturbation diagrams of a partition function. In the system with the Hamiltonian $\mathcal{H}=\mathcal{H}_0+\mathcal{H}_1$, we can express the partition function as an expansion in the interaction picture,

$$\begin{aligned} Z &= \text{tr} [e^{-\beta\mathcal{H}}] \\ &= \sum_k (-1)^k \int_{\tau_{k-1}}^{\beta} d\tau_k \cdots \int_0^{\beta} d\tau_1 \text{tr} \left[\mathcal{T}_{\tau} e^{-\beta\mathcal{H}_0} \hat{\mathcal{H}}_1(\tau_k) \cdots \hat{\mathcal{H}}_1(\tau_1) \right] , \end{aligned} \quad (3.13)$$

where $\hat{\mathcal{O}}(\tau) \equiv e^{\tau\mathcal{H}_0} \mathcal{O} e^{-\tau\mathcal{H}_0}$ for an operator \mathcal{O} and T_{τ} represents a time-ordering operator. After the expansion, the partition function can be regarded as a sum of probability distribution,

$$Z = \int_{\mathcal{C}} d\mathbf{x} \, p(\mathbf{x}) . \quad (3.14)$$

In the CTQMC method, a random walker roams the configuration space \mathcal{C} , satisfying the probability distribution $p(\mathbf{x})$. The configuration space is composed of a perturbation order, perturbation positions on the imaginary-time axis, and other parameters depending on the specific algorithm. Using the

stochastic sampling of observables, we can obtain the expectation value of the general observables A ,

$$\langle A \rangle = \frac{1}{Z} \int_{\mathcal{C}} d\mathbf{x} A(\mathbf{x}) p(\mathbf{x}) . \quad (3.15)$$

The observables are not limited to the number but the function such as Green's function, two-particle correlation function, and etc.

In the subsequent subsections, we will discuss two different CTQMC algorithms to solve the quantum impurity problem in Eqn. (3.2).

3.3.1 Weak Coupling Algorithm

In the weak coupling algorithm, the expansion term in the quantum impurity model is the on-site Coulomb interaction term

$$\mathcal{H}_1 = U \left(n_{\uparrow} n_{\downarrow} - \frac{n_{\uparrow} + n_{\downarrow}}{2} \right) - \frac{K}{\beta} . \quad (3.16)$$

Here, K is introduced as a tuning parameter of the perturbation order. Using the Hubbard-Stratonovich transformation, we can decompose the interacting Hamiltonian into the bilinear form,

$$1 - \frac{\beta U}{K} \left(n_{\uparrow} n_{\downarrow} - \frac{n_{\uparrow} + n_{\downarrow}}{2} \right) = \frac{1}{2} \sum_{s=\pm 1} e^{\gamma s (n_{\uparrow} - n_{\downarrow})} , \quad (3.17)$$

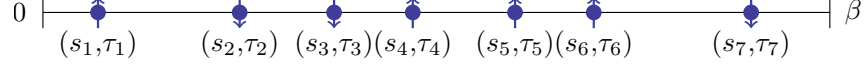


Figure 3.3: Configuration of the weak coupling algorithm. Horizontal line represents the imaginary-time axis. Auxiliary Ising spins are marked as the up and down arrows at the time points of closed symbol.

where $\cosh \gamma = 1 + \frac{U\beta}{2K}$. And the expansion term is $(-\mathcal{H}_1) = (K/2\beta) \sum_{\{s\}} \exp\{\gamma s(n_{\uparrow} - n_{\downarrow})\}$. Then the partition function can be expressed by

$$Z = \sum_{k=0} \sum_{\{s_i\}} \int_0^{\beta} d\tau_1 \cdots \int_{\tau_{k-1}}^{\beta} d\tau_k \left(\frac{K}{2\beta} \right)^k Z_k(\{s_i, \tau_i\}) ,$$

$$Z_k(\{s_i, \tau_i\}) \equiv \text{tr} \left[\prod_{i=k}^1 e^{-\Delta\tau_i \mathcal{H}_0} e^{s_i \gamma (n_{\uparrow} - n_{\downarrow})} \right] . \quad (3.18)$$

Here, $\Delta\tau_i = \tau_{i+1} - \tau_i$. Now, the configuration space is defined by the combination of $\{(s_i, \tau_i)\}$, which is demonstrated in Fig. 3.3. For a given point in configuration space, it can be easily shown that the weight of the point is proportional to Z_k ,

$$\frac{Z_k(\{s_i, \tau_i\})}{Z_0} = \prod_{\sigma} \det \mathbf{N}_{\sigma}^{-1}(\{s_i, \tau_i\}) ,$$

$$\mathbf{N}_{\sigma}^{-1}(\{s_i, \tau_i\}) \equiv e^{V_{\sigma}(\{s_i\})} - \mathbf{G}_{0\sigma}^{\{\tau_i\}} (e^{V_{\sigma}(\{s_i\})} - 1) ,$$

$$e^{V_{\sigma}(\{s_i\})} \equiv \text{diag}(e^{\gamma(-1)^{\sigma} s_1}, \dots, e^{\gamma(-1)^{\sigma} s_k}) , \quad (3.19)$$

where $(-1)^{\uparrow} \equiv 1$, $(-1)^{\downarrow} \equiv -1$, and $(\mathbf{G}_{0\sigma}^{\{\tau_i\}})_{a,b} = \mathcal{G}_{\sigma}^0(\tau_a - \tau_b)$.

The three major Monte Carlo updates will be described below. The first update is the insertion of an auxiliary Ising spin. If the insertion update is accepted, the configuration of the Monte Carlo sampling is changed in the

following manner

$$\begin{aligned} & \{(s_1, \tau_1), \dots, (s_i, \tau_i), (s_{i+1}, \tau_{i+1}), \dots, (s_k, \tau_k)\} \\ \rightarrow & \{(s_1, \tau_1), \dots, (s_i, \tau_i), (s_{new}, \tau_{new}), (s_{i+1}, \tau_{i+1}), \dots, (s_k, \tau_k)\} . \end{aligned} \quad (3.20)$$

The removal of an arbitrarily chosen auxiliary Ising spin is another update. In this update, the configuration space is updated by

$$\begin{aligned} & \{(s_1, \tau_1), \dots, (s_{i-1}, \tau_{i-1}), (s_i, \tau_i), (s_{i+1}, \tau_{i+1}), \dots, (s_k, \tau_k)\} \\ \rightarrow & \{(s_1, \tau_1), \dots, (s_{i-1}, \tau_{i-1}), (s_{i+1}, \tau_{i+1}), \dots, (s_k, \tau_k)\} . \end{aligned} \quad (3.21)$$

The insertion and removal updates constitute the ergodic sampling to span the whole configuration space.

In addition to these two updates, there exists another update which makes Monte Carlo sampling more efficient. It is the spin-flip update which modifies the configuration space by

$$\begin{aligned} & \{(s_1, \tau_1), \dots, (s_i, \tau_i), \dots, (s_k, \tau_k)\} \\ \rightarrow & \{(s_1, \tau_1), \dots, (-s_i, \tau_i), \dots, (s_k, \tau_k)\} . \end{aligned} \quad (3.22)$$

During the Monte Carlo updates, several physical observables can be measured. One of the most important observables is the single-particle Green func-

tion,

$$G_\sigma(\tau, \tau') = \frac{1}{Z} \sum_k \sum_{\{s_i\}} \int_0^\beta d\tau_1 \cdots \int_{\tau_{k-1}}^\beta d\tau_k \left(\frac{K}{2N_c\beta} \right)^k Z_k(\{s_i, \tau_i\}) \times \tilde{G}_\sigma^{\{s_i, \tau_i\}}(\tau, \tau') , \quad (3.23)$$

where $\tilde{G}_\sigma^{\{s_i, \tau_i\}}(\tau, \tau')$ is the Green function for a given configuration $\{(s_i, \tau_i)\}$. After the Hubbard-Stratonovich transformation, the Green's function for a given configuration can be expressed by the noninteracting Green function using Wick's theorem,

$$\begin{aligned} \tilde{G}_\sigma^{\{s_i, \tau_i\}}(\tau, \tau') &= \mathcal{G}_\sigma^0(\tau, \tau') + \sum_{l,m=1}^k \mathcal{G}_\sigma^0(\tau, \tau_l) M_{lm} \mathcal{G}_\sigma^0(\tau_m, \tau') \\ M_{lm} &= [(e^{V_\sigma(\{s_i\})} - 1) \mathbf{N}_\sigma(\{s_i, \tau_i\})]_{lm} . \end{aligned} \quad (3.24)$$

Then we can measure $G_\sigma(\tau, \tau')$ by the Monte Carlo average of $\tilde{G}_\sigma^{\{s_i, \tau_i\}}(\tau, \tau')$,

$$G_\sigma(\tau, \tau') = \left\langle \tilde{G}_\sigma^{\{s_i, \tau_i\}}(\tau, \tau') \right\rangle_{\text{MC}} .$$

In addition to the Green function, we can also use Wick's theorem to obtain for higher point correlation functions, e.g. spin-spin, density-density correlation function, and etc.

3.3.2 Strong Coupling Algorithm

In the strong coupling algorithm, we take $\mathcal{H}_{\text{bath}} + \mathcal{H}_{\text{loc}}$ as an unperturbed Hamiltonian \mathcal{H}_0 and expand the full Hamiltonian to the order of $\mathcal{H}_1 = \mathcal{H}_{\text{hyb}}$. By recalling that $\mathcal{H}_{\text{hyb}} = \sum_\sigma (h_\sigma + h_\sigma^\dagger)$ with $h_\sigma \equiv \sum_{\mathbf{p}} V_{\mathbf{p}\sigma} a_{\mathbf{p}\sigma}^\dagger c_\sigma$, we can rewrite

Eqn. (3.13) in the form

$$\begin{aligned}
Z &= \text{Tr} \left[e^{-\beta \mathcal{H}_a} \prod_{\sigma} \sum_{k_{\sigma}=0}^{\infty} \right. \\
&\times \int_0^{\beta} d\tau_{1\sigma} \int_0^{\beta} d\tau'_{1\sigma} \cdots \int_{\tau_{k_{\sigma}-1}}^{\beta} d\tau_{k_{\sigma}} \int_{\tau'_{k_{\sigma}-1}}^{\beta} d\tau'_{k_{\sigma}} \\
&\times \left. \tilde{h}_{\sigma}(\tau_{k_{\sigma}}) \tilde{h}_{\sigma}^{\dagger}(\tau'_{k_{\sigma}}) \cdots \tilde{h}_{\sigma}(\tau_{1\sigma}) \tilde{h}_{\sigma}^{\dagger}(\tau'_{1\sigma}) \right]. \quad (3.25)
\end{aligned}$$

Here, we have used the fact that only the terms in which \tilde{h}_{σ} and $\tilde{h}_{\sigma}^{\dagger}$ appear alternately the same number of times produce nonzero traces due to the fermionic nature of electrons.

We use a bath partition function Z_{bath} defined by

$$Z_{\text{bath}} \equiv \text{Tr}_a [e^{-\beta \mathcal{H}_{\text{bath}}}] = \prod_{\mathbf{p}\sigma} (1 + e^{-\beta \varepsilon_{\mathbf{p}}}) \quad (3.26)$$

and apply the Wick theorem to the bath fermionic operators to obtain the expanded form of the partition function

$$\begin{aligned}
Z &= Z_{\text{bath}} \text{Tr}_c \left[e^{-\beta \mathcal{H}_{\text{loc}}} \prod_{\sigma} \sum_{k_{\sigma}=0}^{\infty} \int_0^{\infty} d\tau_{1\sigma} \int_0^{\infty} d\tau'_{1\sigma} \cdots \int_{\tau_{k_{\sigma}-1}}^{\infty} d\tau_{k_{\sigma}} \int_{\tau'_{k_{\sigma}-1}}^{\infty} d\tau'_{k_{\sigma}} \right. \\
&\times \left. \tilde{c}_{\sigma}(\tau_{k_{\sigma}}) \tilde{c}_{\sigma}^{\dagger}(\tau'_{k_{\sigma}}) \cdots \tilde{c}_{\sigma}(\tau_{1\sigma}) \tilde{c}_{\sigma}^{\dagger}(\tau'_{1\sigma}) \det \Delta_{\sigma} \right]. \quad (3.27)
\end{aligned}$$

Here, Δ_{σ} is a $k_{\sigma} \times k_{\sigma}$ matrix with elements

$$(\Delta_{\sigma})_{ij} \equiv \Delta_{\sigma}(\tau'_{i_{\sigma}} - \tau_{j_{\sigma}}),$$

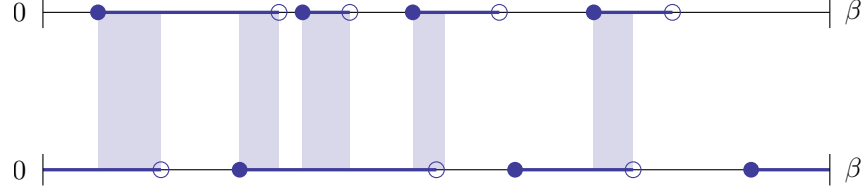


Figure 3.4: Configuration of the strong coupling algorithm. Upper (lower) horizontal line represents the imaginary-time axis of spin-up (down). Segment, which is explained in the text, starts at the time point of the closed symbol and ends at the time point of the open symbol. Overlap between the segments of the spin-up and down time-axis is marked by the shaded region.

with the antiperiodic hybridization function being given by

$$\Delta_{\sigma}(\tau) = [\theta(-\tau) - \theta(\tau)] \sum_{\mathbf{p}} \frac{|V_{\mathbf{p}\sigma}|^2}{e^{\beta\varepsilon_{\mathbf{p}}} + 1} e^{-\{\tau - \beta\theta(\tau)\}\varepsilon_{\mathbf{p}}} \quad (3.28)$$

and with $\theta(\tau)$ being a step function.

In the quantum impurity model, the occupation number operator at the impurity commutes with \mathcal{H}_0 , so we can give a systematic description of the local trace factor in terms of *segments* and *antisegments*; they represent time intervals during which an electron is present and absent at the impurity, respectively. Typical configuration is displayed in Fig. 3.4. In the segment description, the local weight factor for

$$x = \prod_{\sigma} \{(\tau_{1\sigma}, \tau'_{1\sigma}), \dots, (\tau_{k\sigma}, \tau'_{k\sigma})\} , \quad (3.29)$$

is given by

$$\begin{aligned}
\omega_{\text{loc}}(x) &\equiv \text{Tr}_c \left[e^{-\beta \mathcal{H}_{\text{loc}}} \right. \\
&\quad \times \prod_{\sigma} \tilde{c}_{\sigma}(\tau_{k_{\sigma}}) \tilde{c}_{\sigma}^{\dagger}(\tau'_{k_{\sigma}}) \cdots \tilde{c}_{\sigma}(\tau_{1_{\sigma}}) \tilde{c}_{\sigma}^{\dagger}(\tau'_{1_{\sigma}}) \left. \right] \\
&= s e^{\mu \sum_{n\sigma} L_{n\sigma}} e^{-U \sum_{nm} O_{nm}}, \tag{3.30}
\end{aligned}$$

where $L_{n\sigma}$ is the length of the n th segment of an electron with spin σ , O_{nm} is the overlap between the n th spin-up and the m th spin-down segments on the imaginary-time axis, and s is a sign determined by the sequence of operators. The main procedures in updating the configuration are the insertion and the removal of segments or antisegments. We have separated the proposal probability so that we can get rid of the factor $d\tau^2$ in the weight factor. We have also used self-balance and global updates, which can reduce the autocorrelation time significantly.

The above procedures enable us to evaluate the impurity Green function, $G_{\sigma}(\tau) \equiv -\langle T_{\tau} c_{\sigma}(\tau) c_{\sigma}^{\dagger}(0) \rangle$, by using the formula

$$G_{\sigma}(\tau) = -\frac{1}{\beta} \left\langle \sum_{ij}^{k_{\sigma}} (\mathbf{M}_{\sigma})_{ji} \tilde{\delta}(\tau, \tau_i - \tau_j') \right\rangle, \tag{3.31}$$

where the angular brackets denote the Monte Carlo average, $\mathbf{M}_{\sigma} \equiv \Delta_{\sigma}^{-1}$, and

$$\tilde{\delta}(\tau, \tau') \equiv [\theta(\tau') - \theta(-\tau')] \delta(\tau - \tau' - \beta \theta(-\tau')). \tag{3.32}$$

One advantage of the strong coupling is that we can measure directly some local quantities during Monte Carlo samplings. The average occupancy can be

evaluated by using the ratio of the Monte Carlo average of the total segment length to the length of the imaginary-time axis:

$$\langle n_\sigma \rangle = \frac{1}{\beta} \left\langle \sum_n L_{n\sigma} \right\rangle. \quad (3.33)$$

Similarly, the Monte Carlo average of the total overlap length gives the double occupancy through the formula

$$d_O \equiv \langle n_\uparrow n_\downarrow \rangle = \frac{1}{\beta} \left\langle \sum_{nm} O_{nm} \right\rangle. \quad (3.34)$$

In the strong coupling algorithm, we can also use the average perturbation order $\langle k_\sigma \rangle$ to evaluate the average kinetic energy of electrons with spin σ , $\varepsilon_{K\sigma}$ [11, 12]. We can show that the perturbation order estimates the average value of the perturbing action, which enables us to obtain the kinetic energy directly from the Monte Carlo average of the perturbation order:

$$\begin{aligned} \langle k_\sigma \rangle &= - \int_0^\beta d\tau \int_0^\beta d\tau' \Delta_\sigma(\tau - \tau') \langle c_\sigma^\dagger(\tau) c_\sigma(\tau') \rangle \\ &= -\text{Tr}[\Delta_\sigma G_\sigma] \\ &= -\beta \varepsilon_{K\sigma} . \end{aligned} \quad (3.35)$$

Chapter 4

Estimate of the Phase Transition Line in the Infinite-Dimensional Hubbard Model

4.1 Introduction

Over the past few decades, the dynamical mean-field theory (DMFT) [4, 13] and its extensions [14] have proven to be successful in describing the dynamic properties of strongly correlated systems. In DMFT, a lattice model is mapped onto a corresponding quantum impurity model such as the Anderson impurity model. The impurity self-energy, which is obtained by solving the quantum impurity model, is identified with that of the lattice model, imposing a self-consistency relation. Here, we assume that the self-energy is local; this is the case in infinite spatial dimensions and provides a good approximation in high

dimensions.

The efficiency of the DMFT depends strongly on the method of solving the quantum impurity problem, which is called *an impurity solver*. Some perturbative methods such as iterative perturbation theory [15] and the noncrossing approximation [16] were proposed and turned out to yield qualitatively correct results. For a quantitatively accurate description, however, non-perturbative methods must be developed. One of the reliable non-perturbative tools is the Hirsch-Fye quantum Monte Carlo method [17], which is useful at finite temperatures. In that method, however, the discretization of the imaginary-time axis raises difficulties in capturing the sharp variation of the imaginary-time Green function, particularly at low temperatures. Such a problem can be resolved by using the recently-developed CTQMC method, which performs a stochastic sampling of an expansion order in the imaginary-time axis without any discretization [12, 18–20].

We here intend to examine the finite-temperature Mott transition in the Hubbard model, which is well known to exhibit the characteristic features of the Mott transition [21, 22]. Previous extensive studies help us to understand the qualitative nature of the Mott transition in the Hubbard model: There exists a critical temperature above which only a smooth crossover occurs between a metal and a Mott insulator [23]. Below the critical temperature, in contrast, a coexistence region separates the metallic from the Mott insulating phase [23, 24], which implies that the system undergoes a first-order phase transition somewhere inside the coexistence region [4, 25].

Our work focuses on the numerical determination of a phase transition line

(PTL) of the first-order Mott transition. We can determine a thermodynamically-stable phase from the criterion of the lowest free energy. Also, at finite temperatures, the entropy makes important contributions. Although the QMC method is very useful at finite temperatures, obtaining the entropy directly from the QMC method is very difficult. Accordingly, numerical computation of the PTL has been a challenging problem. Only a few earlier studies made efforts to obtain the PTL by using exact diagonalization [26] or Hirsch-Fye QMC method [27], and a recent CTQMC study succeeded in locating a single transition point at a very low temperature [20].

In this chapter, we present a reliable numerical scheme for estimating the PTL of the Mott transition at low temperatures. We basically use the same differential equation as in Ref. [27]. However, in contrast to that previous study, where some fitting functions were introduced [27], we measure the quantities for the equation directly by using the CTQMC method without any additional manipulation. We show that our method results in the PTL which is fully consistent with earlier finite-temperature studies. We also demonstrate that our finite-temperature result approaches gradually the zero-temperature result when we systematically include low-temperature calculations. Finally, the resulting PTL is found not to be changed significantly by the next-order correction to some approximations that are made while solving the differential equation.

This chapter is organized as follows: Section 4.2 is devoted to the description of the Hubbard model and the DMFT combined with the CTQMC method. We present the results in Sec. 4.3: We display some physical quanti-

ties, such as the double occupancy and the energy density, from the CTQMC method, and we present a phase diagram constructed from the data. Particularly, we describe how we can construct the PTL from the QMC data and give some discussion on the resulting PTL. The results are summarized in Sec. 4.4.

4.2 Model and method

We begin with the one-band Hubbard model. Its Hamiltonian is given by

$$\mathcal{H} = -t \sum_{\langle ij \rangle \sigma} (c_{i\sigma}^\dagger c_{j\sigma} + c_{j\sigma}^\dagger c_{i\sigma}) + U \sum_i n_{i\uparrow} n_{i\downarrow} - \mu \sum_{i\sigma} n_{i\sigma} . \quad (4.1)$$

Here, $c_{i\sigma}$ ($c_{i\sigma}^\dagger$) is an annihilation (creation) operator for an electron with spin σ at site i , and $n_{i\sigma} \equiv c_{i\sigma}^\dagger c_{i\sigma}$. The parameters t and U denote the nearest-neighbor hopping amplitude and the on-site Coulomb repulsion, respectively. The chemical potential μ is set to $U/2$ so that the system is half-filled. We consider a Bethe lattice in infinite dimensions, which results in a semicircular density of state

$$\rho(\varepsilon) = \frac{2}{\pi D} \sqrt{1 - (\varepsilon/D)^2} \quad (4.2)$$

with a half bandwidth $D=2t$. We restrict our study to paramagnetic solutions, and throughout the chapter, we will represent all the energies in units of D .

In this work, we employ the single-site DMFT [4]. The central idea of the DMFT is to map a lattice model onto a quantum impurity model, which should satisfy a self-consistency relation imposed from the original lattice model. The

effective action of the quantum impurity model is written in the form of

$$\begin{aligned}
S_{\text{eff}} = & S_o \\
& + \sum_{\sigma} \int_0^{\beta} d\tau \int_0^{\beta} d\tau' c_{\sigma}^{\dagger}(\tau) \Delta_{\sigma}(\tau - \tau') c_{\sigma}(\tau') ,
\end{aligned} \tag{4.3}$$

where S_o is an action at the impurity site due to the local interaction, as well as the chemical potential, and $\beta \equiv 1/T$ is an inverse temperature. The hybridization function $\Delta_{\sigma}(\tau)$ in Eqn. (4.3) plays the role of a generalized Weiss field. We should note that it is a function of the imaginary time τ .

In infinite dimensions the self-energy is local, that is, independent of the momentum, and the local Green function with spin σ is given by

$$G_{\sigma}(i\omega_n) = \int_{-\infty}^{\infty} d\varepsilon \frac{\rho(\varepsilon)}{i\omega_n - \varepsilon + \mu - \Sigma_{\sigma}(i\omega_n)}. \tag{4.4}$$

The corresponding hybridization function Δ_{σ} can also be calculated as

$$\Delta_{\sigma}(i\omega_n) = i\omega_n + \mu - \Sigma_{\sigma}(i\omega_n) - G_{\sigma}^{-1}(i\omega_n). \tag{4.5}$$

In the DMFT, the local self-energy is assumed to be an impurity self-energy, yielding

$$\begin{aligned}
\left[\int_{-\infty}^{\infty} d\varepsilon \frac{\rho(\varepsilon)}{i\omega_n - \varepsilon + \mu - \Sigma_{\sigma}(i\omega_n)} \right]^{-1} \\
= i\omega_n + \mu - \Sigma_{\sigma}(i\omega_n) - \Delta_{\sigma}(i\omega_n).
\end{aligned} \tag{4.6}$$

This is the self-consistency relation that should be satisfied by the self-energy

of the quantum impurity with the hybridization function Δ_σ . By using a semicircular density of states for $\rho(\epsilon)$ in Eqn. (4.2), we can further simplify the above self-consistency relation to the form

$$\Delta_\sigma(\tau) = \frac{D^2}{4} G_\sigma(\tau) \quad (4.7)$$

in the infinite-dimensional Bethe lattice.

4.3 Results

4.3.1 Double occupancy and energy density

We first examine the double occupancy d_O defined in Eqn. (3.34). The double occupancy is well known to provide a good measure for the degree of correlation. As was explained in the Sec. 3.3, in the CTQMC method, it can be calculated directly from the total overlap length of the segments. Figure 4.1(a) presents the calculated double occupancy at the temperature $T=1/128$. As U increases, the system becomes more correlated, and the double occupancy decreases. At a certain interaction strength $U_{c2}(T)$, the double occupancy shows a discontinuous jump to a lower value, and the system becomes insulating. On the other hand, when the interaction strength is decreased from that for the insulating solutions, the system exhibits a discontinuous jump in the double occupancy at the interaction strength $U_{c1}(T)$, which is lower than $U_{c2}(T)$. Accordingly, we have a finite region $U_{c1} < U < U_{c2}$ where both metallic and insulating phases coexist; this demonstrates clearly the first-order nature of the

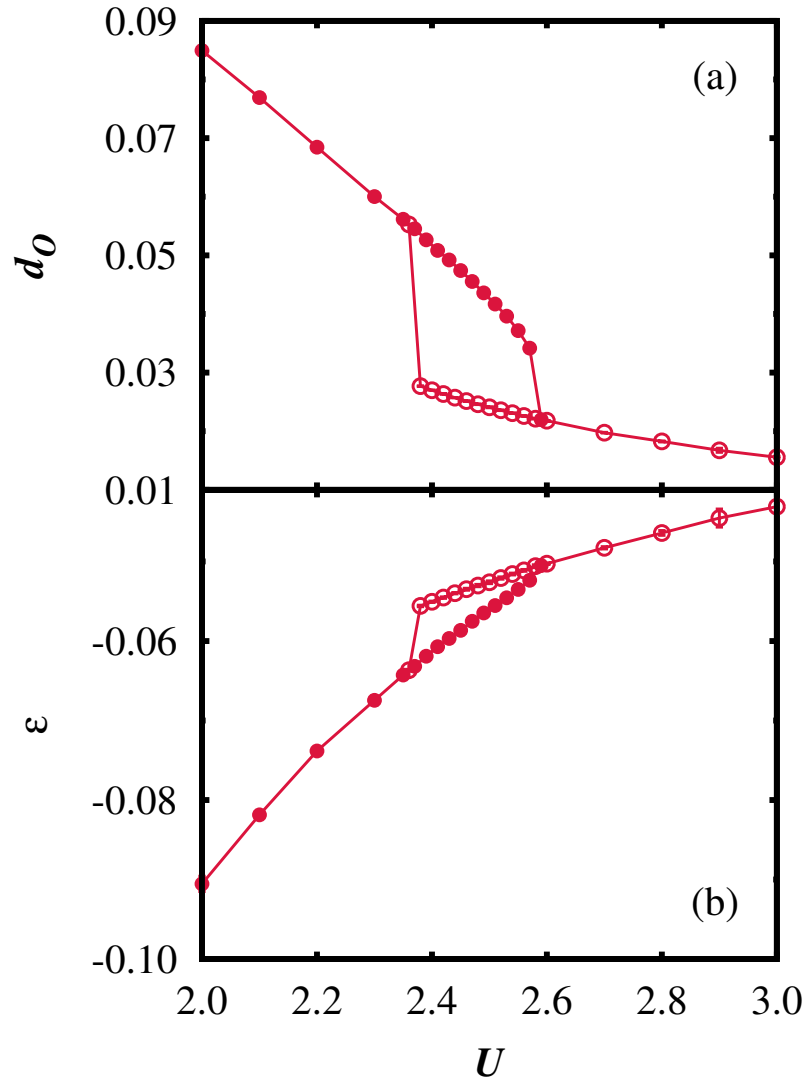


Figure 4.1: (a) Double occupancy d_O and (b) energy density ε as functions of U at the temperature $T=1/128$. The data from the DMFT solutions obtained by increasing and decreasing U are marked by solid and empty circles, respectively.

metal-insulator transition in the Hubbard model for infinite dimensions. Such a first-order nature of the transition is also demonstrated in the variation of the energy density. We have calculated the energy per lattice site ε as

$$\varepsilon = \varepsilon_K + \varepsilon_U, \quad (4.8)$$

where we can compute the kinetic energy ε_K and the interaction energy ε_U directly from the average quantities in the CTQMC method:

$$\varepsilon_K \equiv -T \sum_{\sigma} \langle k_{\sigma} \rangle, \quad (4.9)$$

$$\varepsilon_U \equiv U d_O. \quad (4.10)$$

We observe a clear hysteresis between the metallic and the insulating solutions in the energy density as in the double occupancy. In the coexistence region, the metallic phase always has a lower energy density than the insulating phase at $T=1/128$, which is consistent with earlier DMFT results [4, 28].

4.3.2 Phase diagram and critical point

We can determine two transition points, $U_{c1}(T)$ and $U_{c2}(T)$, from the interaction strengths at which the double occupancy or the energy density shows discontinuous jumps at temperature T . In Fig. 4.2 we plot U_{c1} and U_{c2} as functions of the temperature T , displaying the phase diagram for metal-insulator transitions on the plane of T and U . Both U_{c1} and U_{c2} increase monotonically as the temperature is lowered. With decreasing T , the rate of increase of U_{c1}

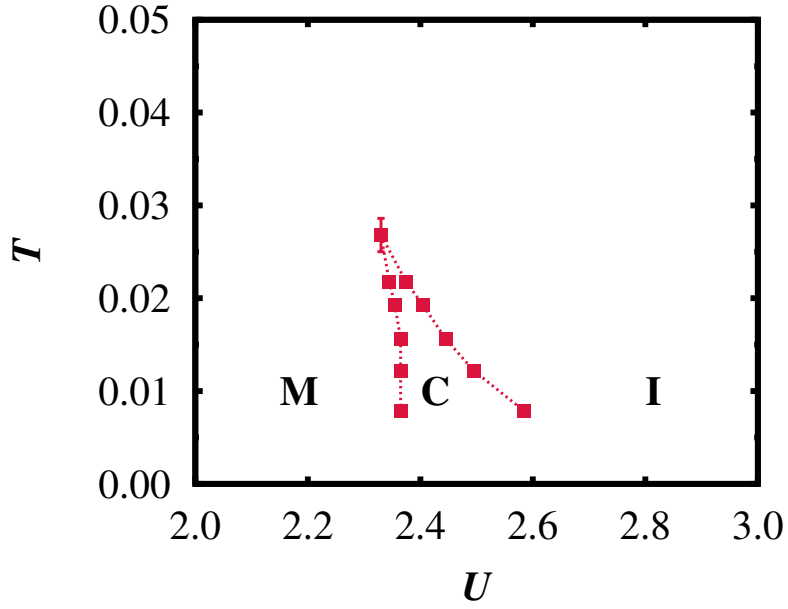


Figure 4.2: Phase diagram for the Mott transition in the infinite-dimensional Hubbard model. The transition interaction strengths U_{c1} and U_{c2} (see the text for definitions) are plotted for various temperatures, and the lines are merely guides to the eye. The regions of the metallic and the insulating phases and their coexisting regions are denoted by the labels M, I, and C, respectively.

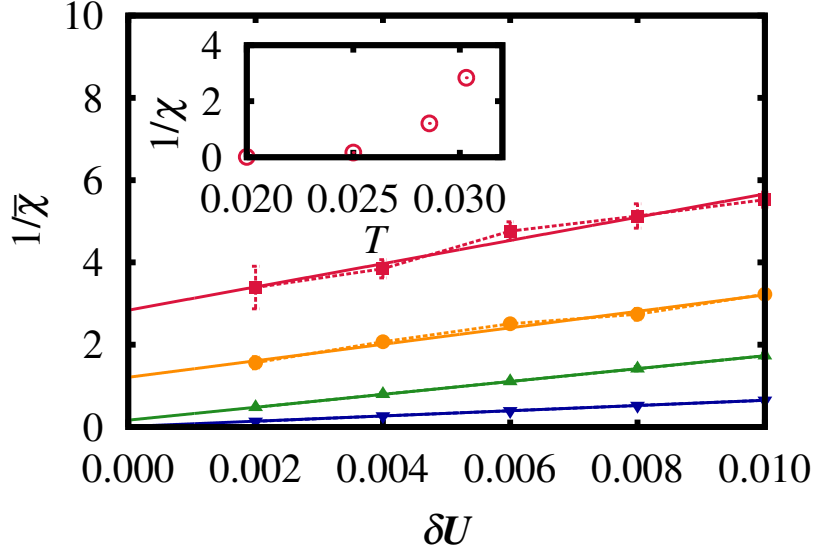


Figure 4.3: Inverse susceptibility $1/\bar{\chi}$ estimated by using numerical derivatives with a finite interval δU for various temperatures. The data for $T = 1/33, 1/35, 1/40$, and $1/50$ are marked by squares, circles, triangles, and inverted triangles, respectively (from top to bottom). The solid lines represent the best linear fits for each temperature. The inset shows the inverse susceptibility $1/\chi$, which is estimated by extrapolating to $\delta U=0$.

diminishes while it is enhanced for U_{c2} . The two transition lines merge at the critical temperature T_c , which gives an upper bound on the temperature of the coexistence region denoted by C in Fig. 4.2. Above T_c , insulating and metallic phases are connected gradually without any abrupt change.

By using the liquid-gas analogy [29], we define the susceptibility [23] as

$$\chi \equiv \lim_{\delta U \rightarrow 0} \bar{\chi}(\delta U) , \quad (4.11)$$

with

$$\bar{\chi}(\delta U) \equiv \max_U \left(-\frac{d_O(U + \delta U) - d_O(U)}{\delta U} \right). \quad (4.12)$$

Because the susceptibility χ diverges at the critical temperature T_c , we can use χ to estimate the critical point precisely. In Fig. 4.3, we plot the inverse of $\bar{\chi}$ as a function of δU . We can then estimate $1/\chi(T)$ by extrapolating the best linear fit to the data at the temperature T to the y -axis. As is demonstrated in the inset of Fig. 4.3, the critical temperature T_c is estimated to be in the range $1/40 < T_c < 1/35$, which is consistent with earlier results from DMFT combined with QMC [23, 27] and the exact diagonalization [26]. It is slightly smaller than the estimate from the DMFT combined with the numerical renormalization group (NRG) [24]. The corresponding critical interaction strength $U_c(T_c) \equiv U^*$ is $U^* = 2.33 \pm 0.01$.

4.3.3 Phase transition line

In the thermodynamic limit, the system in equilibrium resides in the phase with the lowest free energy, and the phase transition between the two coexisting phases occurs on the line where the free energies of the two phases are the same. In this section, we will construct the PTL inside the coexistence region by means of the DMFT combined with the CTQMC method, which will be sketched below.

The free energy density f of the system is defined by

$$f \equiv \varepsilon - Ts, \quad (4.13)$$

where s is the entropy density, and the change in the free energy density is given by

$$df = -sdT + d_O dU. \quad (4.14)$$

Although this form is a standard one, it is not useful in our method because computing the entropy by using the QMC method is very difficult. Recalling the relation

$$\left. \frac{\partial(\beta f)}{\partial \beta} \right|_U = \varepsilon, \quad (4.15)$$

we can consider an alternative form

$$d(\beta f) = \varepsilon d\beta + \beta d_O dU, \quad (4.16)$$

which is convenient to use because we can obtain the energy density directly from the QMC average.

In the coexistence region, we take the difference in the free energy densities between the metallic and the insulating phases, $\Delta f \equiv f_M - f_I$, and the change of that difference is given by

$$d(\beta \Delta f) = \Delta \varepsilon d\beta + \beta \Delta d_O dU, \quad (4.17)$$

where the subscripts M and I denote the quantities of the metallic and the insulating phases, respectively. On the PTL, the free energies of the two phase are the same, $\Delta f=0$; accordingly, the change in $\beta \Delta f$ vanishes when the

parameters change along the PTL, yielding

$$\begin{aligned} d[\beta\Delta f(\beta, U_c(\beta))] \\ = \Delta\varepsilon(\beta, U_c(\beta))d\beta + \beta\Delta d_O(\beta, U_c(\beta))dU_c(\beta) = 0, \end{aligned} \quad (4.18)$$

where $U_c(\beta)$ is the interaction strength at which the thermodynamic transition occurs at the temperature $T=1/\beta$. The resulting differential equation for the PTL is

$$\frac{dU_c(\beta)}{d\beta} = -\frac{\Delta\varepsilon(\beta, U_c(\beta))}{\beta\Delta d_O(\beta, U_c(\beta))}, \quad (4.19)$$

which can be transformed to a differential equation in temperature T :

$$\frac{dU_c(T)}{dT} = F(T, U_c(T)) \quad (4.20)$$

with

$$F(T, U) = \frac{\Delta\varepsilon(T, U)}{T\Delta d_O(T, U)}. \quad (4.21)$$

In principle, the integration of Eqn. (4.20) with an initial condition $U_c(T_c) = U^*$ yields the PTL.

Indeed, Eqn. (4.20) was employed to study the PTL by using the DMFT with the Hirsch-Fye QMC method [27]. In this study, however, some model-specific fitting functions were introduced in evaluating $F(T, U)$ to manage inevitable Trotter errors and the lack of data points, which may limit the applicability of the method. In contrast, within the CTQMC method employed in this work, such Trotter errors are absent. Furthermore, the kinetic energy and the double occupancy can be measured directly from Monte Carlo sampling.

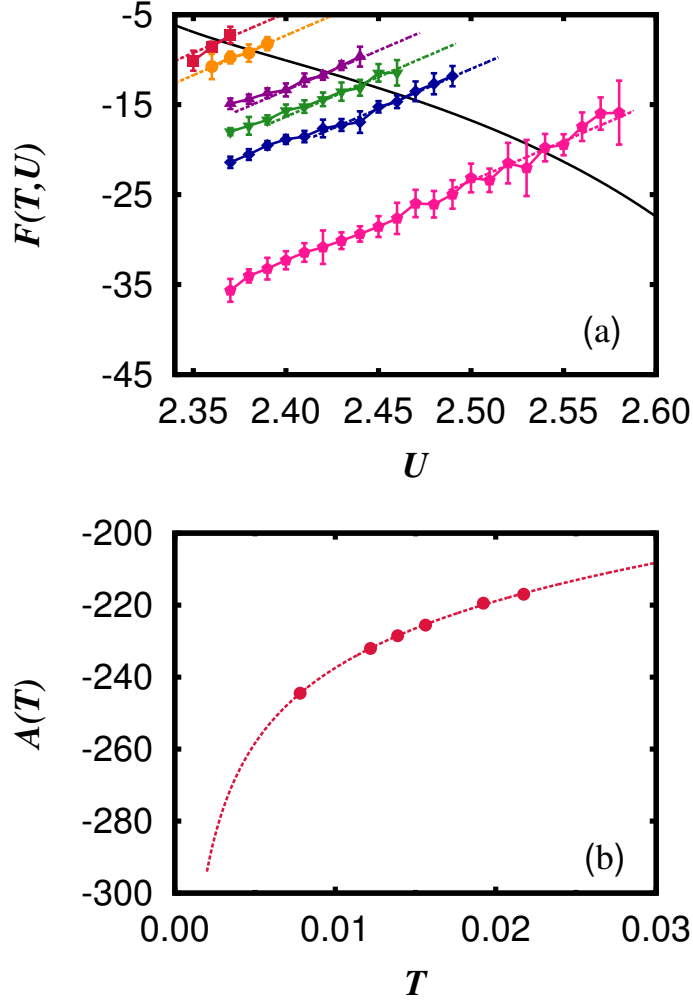


Figure 4.4: (a) $F(T, U)$ as a function of the interaction strength U for various temperatures and (b) $A(T)$ as a function of the temperature T . In panel (a), the data for $T=1/46, 1/52, 1/64, 1/72, 1/82$, and $1/128$ are marked by squares, circles, triangles, inverted triangles, diamonds, and pentagons, respectively (from top to bottom). The curve of $(U_c(T), F(T, U_c(T)))$ is also presented by the solid line. In panel (b), the dashed line represents the best-fit curve to Eqn. (4.23).

Thus, we can prepare $F(T, U)$ for Eqn. (4.20) from the raw data obtained with the CTQMC method by using Eqn. (4.21) without any additional treatment.

In Fig. 4.4(a), we plot $F(T, U)$ calculated directly by using the CTQMC method for various temperatures. We can observe that around the PTL, the data for all temperatures agree well with the function

$$F(T, U) = A(T) + bU \quad (4.22)$$

with $b=88.4$. These functions are denoted by the linear dotted lines in Fig. 4.4(a). We have obtained the value of b from the best linear fit at $T=1/82$. The constant $A(T)$ is also obtained from the intercept of the fitting line at temperature T on $U=0$ axis. According to the Fermi-liquid theory, $A(T)$ can be approximated by using the three leading-order terms,

$$A(T) = \frac{\alpha}{\sqrt{T}} + \gamma + \eta\sqrt{T} , \quad (4.23)$$

at low temperatures, where we can determine α, γ and η from the least-square fits. The integration of Eqn. (4.20) yields an analytic expression for the PTL:

$$\begin{aligned} U_c(T) &= U^* e^{b(T-T_c)} + e^{bT} \int_{T_c}^T dT' A(T') e^{-bT'} \\ &= \left[U^* + \frac{\gamma + \eta\sqrt{T_c}}{b} \right] e^{b(T-T_c)} - \frac{\gamma + \eta\sqrt{T}}{b} \\ &\quad + \frac{\sqrt{\pi}(2\alpha b + \eta)}{2b\sqrt{b}} e^{bT} [\text{erf}(\sqrt{bT}) - \text{erf}(\sqrt{bT_c})], \end{aligned} \quad (4.24)$$

where $T < T_c$ and $\text{erf}(x)$ is the error function defined by

$$\text{erf}(x) \equiv \frac{2}{\sqrt{\pi}} \int_0^x dt e^{-t^2}. \quad (4.25)$$

In fact, $A(T)$ is sensitive to the set of data points that we use to obtain the best fit to Eqn. (4.22). Initially, we guess the PTL $U_c(T)$ and calculate $F(T, U)$ for the data points around the line, which, in turn, yields a new PTL $U_c(T)$ from the best fit to Eqn. (4.22). We have repeated the procedure until the data points used for the fitting reasonably overlap with the resulting PTL. All the fitting results presented in Fig. 4.4 are those obtained using the self-consistent parameters. As can be seen in Fig. 4.4(b), the values of the self-consistent $A(T)$ are well approximated by the expression derived from the Fermi-liquid theory.

In Fig. 4.5(a), we have shown the resulting PTL. Clearly, the slope of PTL is in good agreement with the inverse of $F(T, U(T))$ near the PTL, which demonstrates the full self-consistency of the PTL. We have also examined the dependence of the PTL on the variation in the position of the critical point. We have obtained PTLs for different critical points that were varied maximally within the numerical errors. The resulting PTLs shown in Fig. 4.5(a) show little difference particularly at low temperatures, which indicates that the PTLs estimated at low temperatures are robust against any small variation in the position of the critical point.

In Fig. 4.5(b), we have also compared the PTL obtained in this work with those from earlier DMFT works. The comparison shows that our results are

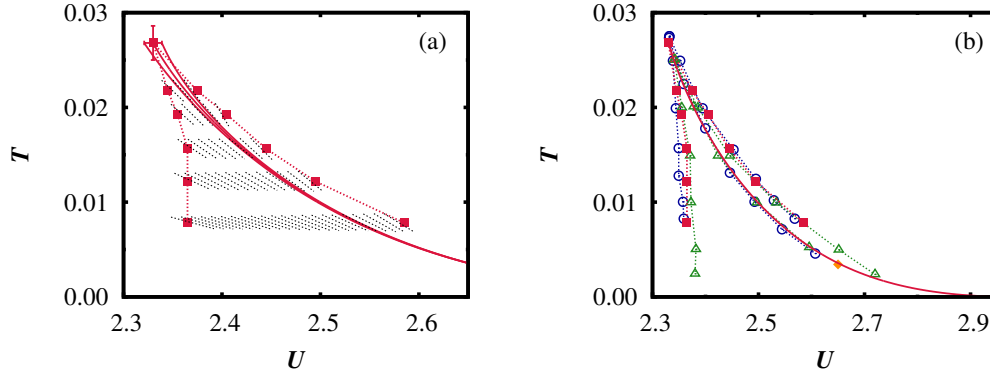


Figure 4.5: (a) Phase transition line (PTL) of the infinite-dimensional Hubbard model and (b) comparison with earlier DMFT results. In panel (a), short dotted-line segments represent the lines with the slope $1/F(T, U)$ at the point (T, U) . The solid lines are PTLs resulting from three different critical points that are varied maximally within the numerical errors. In panel (b), the transition interaction strengths U_{c1} and U_{c2} , and the PTL obtained in this work are denoted by squares and a solid line, respectively. The earlier results obtained by using the Hirsch-Fye quantum Monte Carlo [27], and exact diagonalization [26] are shown as empty circles and triangles, respectively. The diamond represents an earlier CTQMC result [20].

fairly consistent with earlier results up to the lowest temperature that the earlier works examined. Particularly, the agreement with the results obtained from Hirsch-Fye QMC method [27] implies that our method is accurate enough to reproduce the low-temperature transition nature without any knowledge of the preceding zero-temperature results. Notably, our estimated PTL shows excellent agreement with the result obtained from earlier CTQMC calculation at the temperature $T \approx 0.0034$ [20], which is much lower than the lowest temperature $T = 1/128$ for which we were able to obtain raw data from the CTQMC method, indicating the efficiency of our method.

4.3.4 Transition interaction strength at zero temperature

From the PTL in Eqn. (4.24), we can easily estimate the transition interaction strength at zero temperature, which yields $U_c(T=0) \approx 3.04$; this value is slightly higher than the zero-temperature NRG result $U_c \approx 2.94$ [28]. We have also examined the dependence of the estimated $U_c(T=0)$ on the temperature range of the CTQMC data used in the procedure. In determining the PTL, we have used the CTQMC data in the range of $T_L < T < T_H$, where we have fixed the upper-limit temperature as $T_H = 1/46$ and varied the lower-limit temperature T_L . Figure 4.6 shows $U_c(T=0)$ as a function of T_L . As T_L is lowered, the estimated $U_c(T=0)$ shows a monotonic decrease and rapidly approaches the zero-temperature NRG result, which is denoted by the dotted line in the figure. Such a rapid monotonic approach implies that the CTQMC results at

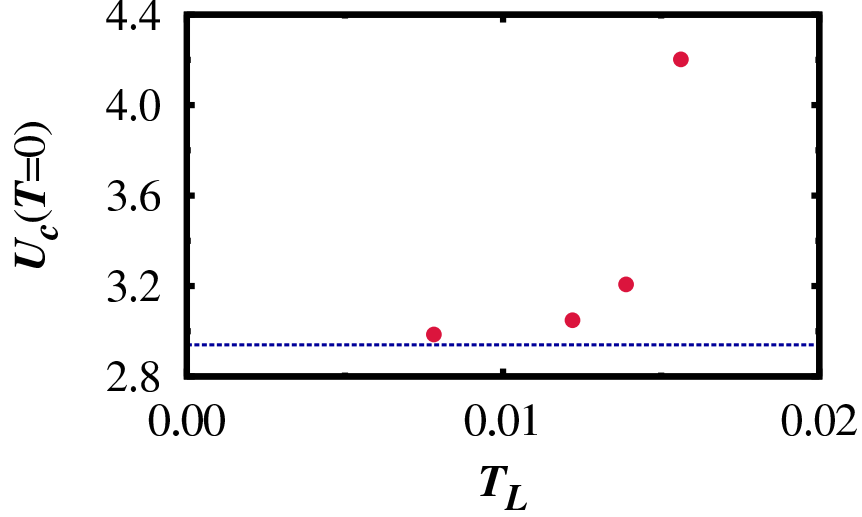


Figure 4.6: $U_c(T=0)$ obtained from the CTQMC data in the temperature range of $T_L < T < T_H$. We have fixed $T_H = 1/46$. The dotted line indicates the zero-temperature NRG result $U_c(T=0) = 2.94$ [28].

finite temperatures are fully consistent with those from the zero-temperature approaches. Here, we should note that our method does not use any knowledge of previous zero-temperature results; this implies that our results in the zero-temperature limit provide an independent check on the zero-temperature result.

4.3.5 Next-order correction

Finally, we check out the validity of the assumption in Eqn. (4.22) that $F(T, U)$ is linear in U . To include the next-order correction, we try the nonlinear function

$$F(T, U) = \frac{A(T) + bU(1 + \zeta U)}{1 + 2\zeta U}, \quad (4.26)$$

which includes a second-order correction in U and allows an analytic solution for the differential equation in Eqn. (4.20). Although this form can include the curvature of data, the singularity in the denominator, which is introduced to allow an analytic solution for the differential equation, limits the range of the parameter ζ . We have varied ζ in the range between -0.1 and 0.1 and found that $U_c(T=0)$ changes only by an amount 0.01, indicating that our low-temperature results are also robust against the small corrections to Eqn. (4.22) arising from next-order terms in U .

4.4 Summary

In summary, we have examined the Mott transition of the Hubbard model at finite temperatures in infinite dimensions by using the DMFT with CTQMC method being an impurity solver. We have measured the double occupancy and the energy density, which yields a critical point, as well as a coexistence region, in the phase diagram. We have determined the PTL of the first-order Mott transition by integrating the differential equation of the transition interaction strength. The PTL constructed in this way has been shown to be in good agreement with earlier results. We have also shown that higher-order corrections do not have much effect on the low-temperature PTL.

Chapter 5

Correlation Effects in Band Insulator

5.1 Introduction

The effects of correlations between electrons have been one of the most fascinating topics in modern condensed matter physics. A variety of remarkable phenomena such as superconductors with high critical temperatures [30] and interaction-driven metal-insulator transitions [31] is well known to arise from electron correlations. In describing such electron correlations, the Hubbard model (HM) opened a new paradigm. It has proved to be successful in capturing the essential physics of correlation-induced phenomena by incorporating just a few simple ingredients: tight-binding electrons with the local Coulomb interaction. Interesting variants of the HM have been proposed to investigate correlation effects in the band insulator (BI). One of the popular examples is the ionic Hubbard model (IHM), where tight-binding electrons interact via the

local Coulomb interaction under a staggered lattice potential [32–34]. It was first applied to the study of the neutral-ionic transition in a charge-transfer organic chain [35–44] and also suggested as a model for the polarization phenomena of ferroelectric perovskite materials [45–50] and Kondo insulators such as FeSi and FeSb₂ [51].

On a bipartite lattice, the staggered lattice potential of the IHM doubles the periodicity of the system, giving rise to a gap at the zone boundary. Accordingly, in the noninteracting limit the system prefers a band insulating phase where most electrons stay on a sublattice with lower potential. The resulting BI competes with a Mott insulator (MI) with one electron per lattice site, which is driven by local interactions. This competition is expected to enrich the physics in the transition between the two phases, which has been studied theoretically for decades.

The emergence of an intermediate phase has been studied in one dimension [37–39, 52–67] and in two dimensions [68–71]. In one dimension, it was revealed by the bosonization method that a spontaneously dimerized insulating phase shows up between the BI and the MI [52, 59–62], which was confirmed subsequently in numerical studies [53, 63–67]. Some peculiar spectral properties such as spin-charge separation were also studied by the cellular dynamical mean-field theory (DMFT) [54, 55]. Extensive investigations have also been made into the effects of additional degrees of freedom on the one-dimensional IHM, including electron-lattice coupling [36, 37, 41], spin-density wave [41, 42, 56, 72], next-nearest-neighbor interaction [36–38, 42, 50, 57], asymmetry in electron hopping [38, 39], alternating Hubbard interaction [56],

periodicity of the lattice [62], coupling with conducting leads [73], and next-nearest neighbor hopping [60]. As to the nature of the intermediate phase in two dimensions, there is some controversy: The determinant quantum Monte Carlo study [68, 69] predicted a metallic phase, while an insulating phase was observed via the cellular DMFT or the variational cluster approach [70?]

In infinite dimensions, on the other hand, the single-site DMFT has revealed two successive metal-insulator transitions at zero temperature [74–77]. Weak interactions tend to reduce the single-particle gap, driving the system into a metallic phase. The system eventually becomes an MI, caused by the further increase in the interaction strength. Here it is remarkable that a metallic phase emerges due to correlation effects of Coulomb interactions; this is in sharp contrast with the intermediate insulating phase, which is confirmed in the one-dimensional IHM. The effects of antiferromagnetic ordering induced by local interactions have also been studied in the IHM [76, 78].

In this chapter, we focus on the finite-temperature properties of the transitions between paramagnetic phases in the infinite-dimensional IHM at half-filling. We adopt the DMFT combined with the continuous-time quantum Monte Carlo (CTQMC) method [12, 18, 20, 79]. First, the spectral properties of the IHM are examined at finite temperatures. The Fermi-level spectral weight, which can be estimated from the imaginary-time Green function, demonstrates that with an increase in the local interaction the system exhibits a crossover from BI to metal, which is followed by a discontinuous transition to an MI. The spectral function as well as local quantities such as double occupancy and staggered charge also supports the above description of the tran-

sition behaviors. The energy density, which can be measured directly from the CTQMC method, shows that the metallic phase always has a lower energy than the Mott insulating phase within the coexistence region as in the standard HM. The resulting finite-temperature phase diagram illustrates that the crossover interaction strength between metal and MI decreases with the temperature. It is also found that the metal-MI transition is similar to that in the HM while the critical temperature tends to increase as the staggered lattice potential becomes stronger. The dependence of the total energy density on the temperature indicates that the correlation-driven metallic phase is a Fermi liquid. The phase diagram at very low temperatures shows that the metallic phase persists for very strong staggered lattice potentials.

This chapter is organized as follows: In Sec. 5.2 we introduce the IHM and describe how to deal with the model by the single-site DMFT with the CTQMC as an impurity solver. Section 5.3 presents the results of our numerical calculations. We examine spectral properties, local quantities, and several components of energy densities, based on which the phase diagram is constructed. We also investigate the nature of the intermediate metallic phase and the dependence of the transition on the strength of the staggered lattice potential. Finally, we conclude the chapter by summarizing the results in Sec. 5.4.

5.2 Model and methods

We consider the IHM on a bipartite lattice, the Hamiltonian of which is given by

$$\begin{aligned}\mathcal{H} = & -t \sum_{\langle ij \rangle \sigma} (c_{j\sigma}^\dagger c_{i\sigma} + c_{i\sigma}^\dagger c_{j\sigma}) + U \sum_i n_{i\uparrow} n_{i\downarrow} \\ & + \sum_{i\sigma} \epsilon_i n_{i\sigma} - \mu \sum_{i\sigma} n_{i\sigma},\end{aligned}\tag{5.1}$$

where $c_{i\sigma}$ ($c_{i\sigma}^\dagger$) is the annihilation (creation) operator of an electron with spin σ at the i th lattice site. The corresponding number operator is defined to be $n_{i\sigma} \equiv c_{i\sigma}^\dagger c_{i\sigma}$. The parameters t and U represent the nearest-neighbor hopping amplitude and the Hubbard interaction, respectively. The lattice is a bipartite one composed of two sublattices, A and B , and the local lattice potential energy ϵ_i is given by

$$\epsilon_i = \begin{cases} \Delta & \text{for } i \in A, \\ -\Delta & \text{for } i \in B. \end{cases}\tag{5.2}$$

In this work we adopt the single-site DMFT, which is exact in infinite dimensions [4]. Within the DMFT, the original lattice model is mapped onto a single-impurity Anderson model, which is described by the Hamiltonian

$$\begin{aligned}\mathcal{H}_{\text{SIAM}}^\alpha = & (\varepsilon_\alpha - \mu) n_{\alpha\sigma} + \sum_k (V_{k\alpha\sigma} c_{\alpha\sigma}^\dagger a_{k\sigma} + h.c.) \\ & + U n_{\alpha\uparrow} n_{\alpha\downarrow} + \sum_k \varepsilon_{k\sigma} a_{k\sigma}^\dagger a_{k\sigma}.\end{aligned}\tag{5.3}$$

Here $c_{\alpha\sigma}$ ($c_{\alpha\sigma}^\dagger$) is the annihilation (creation) operator of an electron at the impurity corresponding to sublattice α , and $a_{k\sigma}$ ($a_{k\sigma}^\dagger$) is the annihilation (cre-

ation) operator of an electron at the k th bath site which has on-site energy $\varepsilon_{k\sigma}$ and is coupled with the impurity via the hybridization matrix element $V_{k\alpha\sigma}$.

The structure of a bipartite lattice leads to an impurity Green function of the form

$$G_{\alpha}(i\omega_n) = \zeta_{\bar{\alpha}} \int_{-\infty}^{\infty} d\varepsilon \frac{\rho_0(\varepsilon)}{\zeta_{\alpha}\zeta_{\bar{\alpha}} - \varepsilon^2} \quad (5.4)$$

for $(\alpha, \bar{\alpha}) = (A, B)$ and (B, A) , where $\rho_0(\varepsilon)$ is the bare density of states (DOS) of the lattice and $\zeta_{\alpha} \equiv i\omega_n - \varepsilon_{\alpha} + \mu - \Sigma_{\alpha}(i\omega_n)$ with the self-energy Σ_{α} and Matsubara frequency ω_n . The calculation is performed on the Bethe lattice, where the DOS is given in the semicircular form: $\rho_0(\varepsilon) = (2/\pi D)\sqrt{1 - (\varepsilon/D)^2}$. Through this chapter we use the half-band width $D = 2t$ as the unit of energy.

The DOS of a semicircular form allows analytic integration of Eqn. (5.4), which yields

$$G_{\alpha}^{-1}(i\omega_n) = \zeta_{\alpha} - \frac{D^2}{4} G_{\bar{\alpha}}(i\omega_n). \quad (5.5)$$

With the help of the particle-hole symmetry, we have the following relations:

$$\begin{aligned} \Sigma_{\alpha}(i\omega_n) &= U - \Sigma_{\bar{\alpha}}(-i\omega_n), \\ G_{\alpha}(i\omega_n) &= -G_{\bar{\alpha}}(-i\omega_n). \end{aligned} \quad (5.6)$$

Then the Dyson's equation, $\mathcal{G}_{0\alpha}^{-1} = \Sigma_{\alpha}(i\omega_n) + G_{\alpha}^{-1}(i\omega_n)$, reduces to

$$\mathcal{G}_{0\alpha}^{-1}(i\omega_n) = i\omega_n - \varepsilon_{\alpha} + \mu + \frac{D^2}{4} G_{\alpha}(-i\omega_n), \quad (5.7)$$

which imposes the self-consistency relation on the impurity problem.

We solve the impurity problem only in sublattice A to obtain $G_A(i\omega_n)$ from

$\mathcal{G}_{0A}(i\omega_n)$ by means of the CTQMC method based on the hybridization expansion, which has proven to be efficient particularly in the strong-interaction regime. We typically use 10^8 Monte Carlo steps for each DMFT iteration, which turns out to be sufficient to achieve the required accuracy of the Green function at the lowest temperature, $T = 1/128$. The self-consistency loop is iterated 50 times for the convergence of the solution within the DMFT.

5.3 Results

5.3.1 Spectral properties

To probe the metal-insulator transitions, we consider the Fermi-level spectral weight:

$$\begin{aligned}\tilde{A}_\alpha &\equiv -\frac{1}{\pi T} G_\alpha(\tau=1/2T) \\ &= \frac{1}{2\pi T} \int_{-\infty}^{\infty} d\omega \frac{1}{\cosh(\omega/2T)} A_\alpha(\omega),\end{aligned}\tag{5.8}$$

where $A_\alpha(\omega) \equiv -(1/\pi)\text{Im}G_\alpha(\omega+i0^+)$ is the spectral function of sublattice α . At very low temperatures \tilde{A}_α is approximately the same as the Fermi-level spectral function $A_\alpha(\omega=0)$. Since the imaginary-time Green function can be measured directly from Monte Carlo sampling, it is frequently used to examine the metal-insulator transition [79–81].

In Fig. 5.1, we present the Fermi-level spectral weight as a function of the temperature T and the interaction strength U . The colored plot on the plane of U and T clearly demonstrates that two insulating phases (dark regions) are

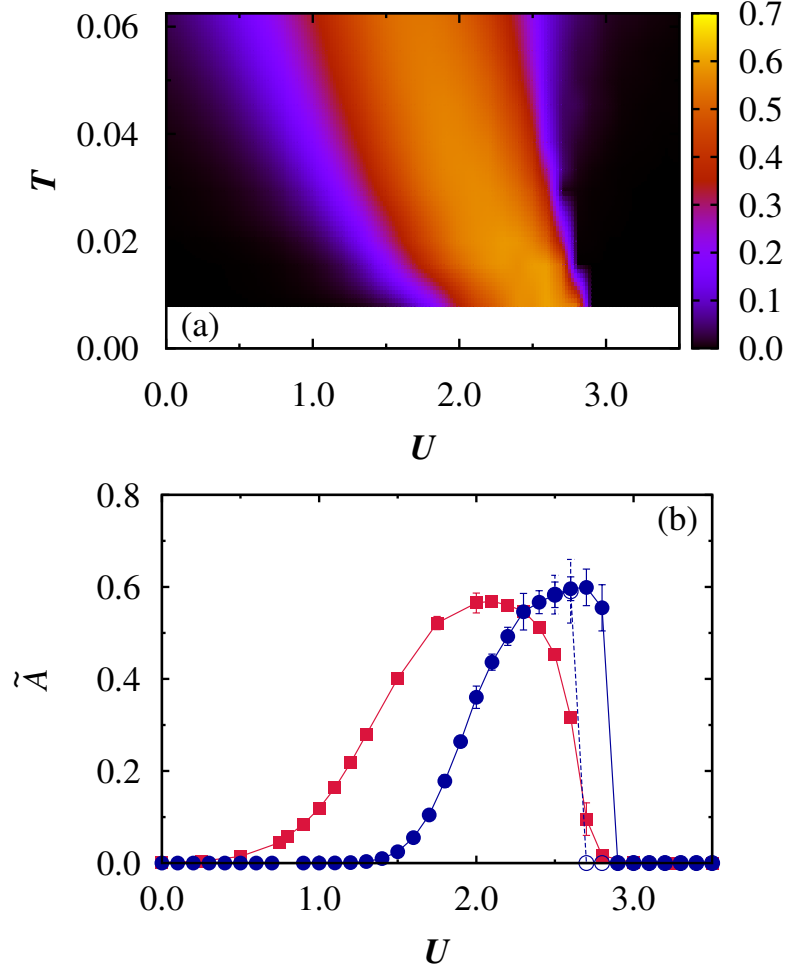


Figure 5.1: Fermi-level spectral weight \tilde{A}_α for $\Delta = 0.5$. (a) The colored plot displays \tilde{A}_α on the plane of the interaction strength U and temperature T , obtained via increasing U . (b) \tilde{A}_α at temperatures $T = 1/32$ [squares] and $1/128$ [circles]. Filled and open symbols for $T = 1/128$ represent data obtained via increasing and decreasing U , respectively.

separated by an intermediate metallic phase (bright region). As clarified in the existing zero-temperature studies [74–76], the insulating phase for weak interactions correspond to a BI, while that at strong interactions represents an MI.

The BI connects smoothly with the metallic phase via a finite-width crossover region at finite temperatures. As the temperature is lowered, the onset value of \tilde{A} becomes steeper and the size of the crossover region decreases appreciably; this is consistent with the continuous transition observed at zero temperature.

For strong interactions, on the other hand, we observe a rather steeper transition between the metal and the MI at finite temperatures. Below a certain critical temperature, the Mott transition turns out to be of first order, which is evidenced by the presence of the hysteretic behavior displayed at $T = 1/128$ in Fig. 5.1(b). Accordingly, we have lower and upper transition interaction strengths, U_{c1} and U_{c2} , at which MI and metallic phases become unstable, respectively. Thermodynamic phase transitions occur between U_{c1} and U_{c2} at finite temperatures; the determination of the phase transition line is discussed later. Above the critical temperature, the boundary between the metal and the MI also appears as a crossover, and the crossover region expands as the temperature is increased.

We use the maximum entropy method (MEM) for analytic continuation of the Matsubara Green function to the real frequency domain and obtain the spectral function $A(\omega)$. The resulting spectral function is presented in Fig. 5.2. In the region of weak interactions, the single-particle gap is formed around the

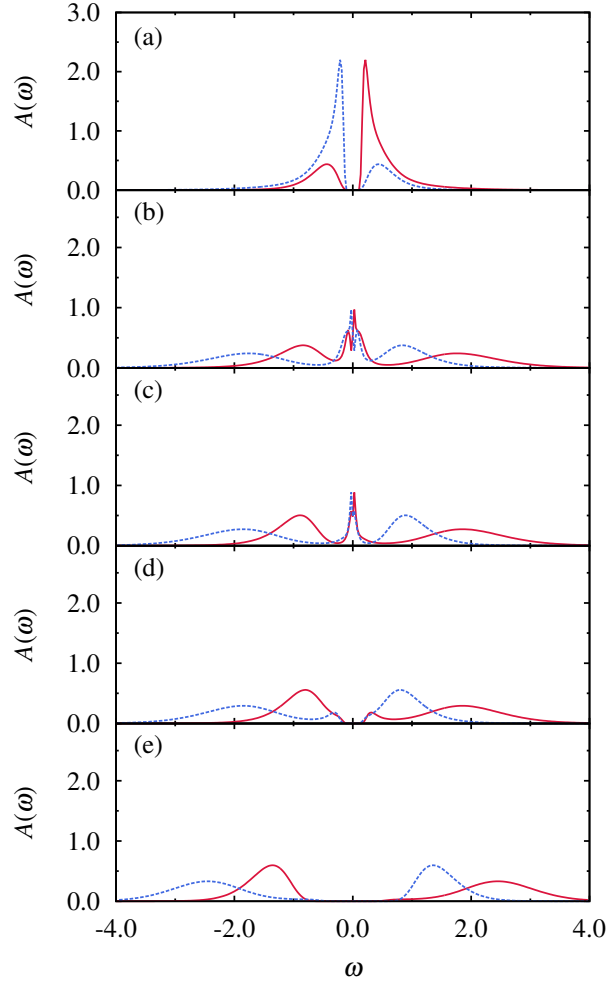


Figure 5.2: Spectral function $A(\omega)$ for $\Delta = 0.5$ and $T = 1/128$. Corresponding interaction strengths are (a) 1.0, (b) 2.5, (c) 2.8 (increasing U), (d) 2.8 (decreasing U), and (e) 4.0. Solid and dotted lines represent the spectral function at sublattices A and B , respectively.

Fermi level with singular behavior at the band edge, which is reminiscent of the noninteracting DOS with a van Hove singularity. We also observe that in the occupation of each sublattice there is a significant imbalance between A and B sublattices, which is a characteristic feature of the BI.

On the other hand, the Mott gap emerges with a prominent four-peak structure for strong interactions. For a given sublattice, two peaks correspond to the upper and the lower Hubbard bands, respectively. The upper or lower Hubbard bands on different sublattices are separated by the staggered lattice potential Δ . Both Hubbard bands on sublattice B , having the lower lattice potential, are located at a lower energy compared with those on sublattice A .

In the intermediate-interaction region, we observe a metallic phase with a finite spectral weight at the Fermi level. In this phase a quasi-particle peak near the Fermi level is surrounded by four Hubbard bands, and the disappearance of the quasi-particle peak signifies the onset of a Mott phase. The quasi-particle peak also shows pseudogap-like behavior around the Fermi level, which is discussed in the zero-temperature study [75]. At temperature $T = 1/128$, there exists a coexistence region where both metal and MI are locally stable. Figures 5.2(c) and 5.2(d) correspond to metallic and insulating solutions, respectively. The overall features of the spectral functions are in good agreement with the previous zero-temperature results obtained via NRG [76].

Before going on to the next section, we make some comments on the stability of our MEM procedure. The stability investigation shows that our MEM procedure is reliable enough to characterize the fine structures of spectral function. For example, the pseudogap-like behavior around the Fermi level in

Fig. 5.2(b) is robust against the statistical fluctuations of the imaginary-time Green function. In our calculations the statistical error of the imaginary-time Green function is around order 10^{-4} . We have also checked the stability of the MEM procedure by examining the dependence on the model function and the scaling parameter selection, which turns out to have negligible effects on the resulting spectral function.

5.3.2 Local quantities

The staggered charge density is given by the difference between the number densities at two sublattices, $n_A - n_B$, with the sublattice number density defined to be $n_\alpha \equiv \sum_\sigma \langle n_{\alpha\sigma} \rangle$ for $\alpha = A$ and B . We also compute the double occupancy d_O given by

$$d_O \equiv \frac{1}{2} \sum_\alpha \langle n_{\alpha\uparrow} n_{\alpha\downarrow} \rangle. \quad (5.9)$$

The results for the double occupancy and the staggered charge density are shown in Figs. 5.3 and 5.4. In the IHM, the interaction strength U competes with the staggered lattice potential Δ due to different favorable electron configurations. While the staggered lattice potential forces electrons to stay at the lower potential sites on sublattice B , the interaction, giving rise to energy cost, tends to prevent two electrons from occupying the same site. In the weak-interaction region, electrons prefer to gather on sublattice B and the system experiences an imbalance between the two sublattices, resulting in a higher double occupancy, compared with the HM, corresponding to $\Delta = 0$,

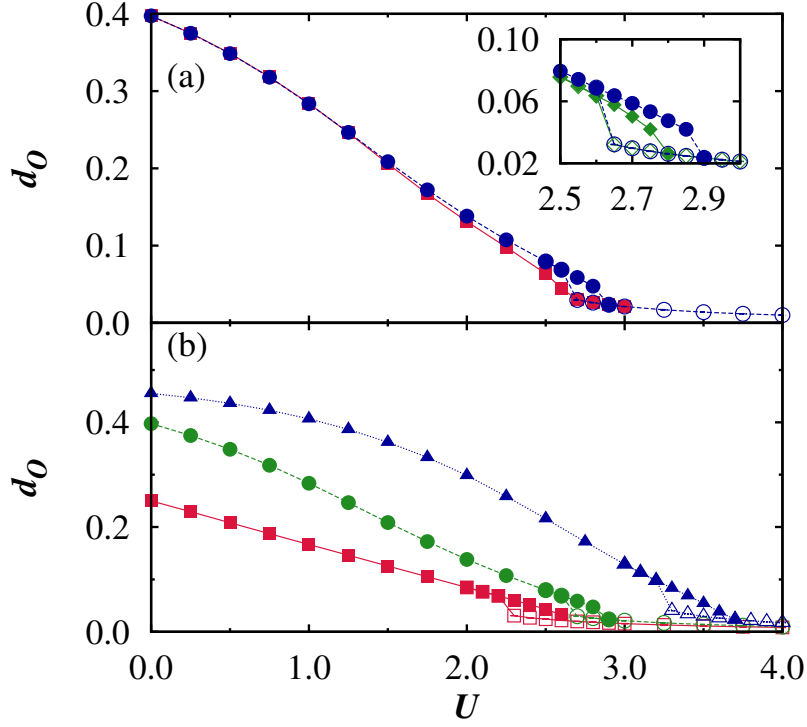


Figure 5.3: Double-occupancy d_O as a function of U : (a) for staggered lattice potential $\Delta = 0.5$ at temperatures $T = 1/32$ [squares] and $T = 1/128$ [circles] and (b) at temperature $T = 1/128$ for various values of the staggered lattice potential—from top to bottom, $\Delta = 1.0, 0.5$, and 0.0 . The inset in (a): Detailed behavior in the coexistence region. Data for $T = 1/64$, diamonds; $T = 1/128$, circles. Data obtained via increasing U , filled symbols; via decreasing U , open symbols.

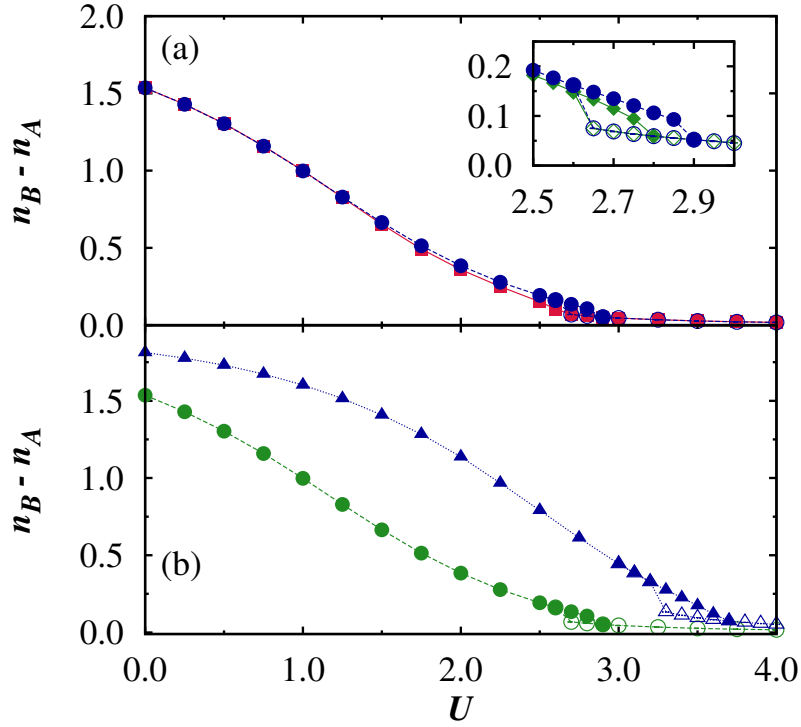


Figure 5.4: Staggered charge density, $n_B - n_A$ as a function of U : (a) for staggered lattice potential $\Delta = 0.5$ at temperatures $T = 1/32$ [squares] and $T = 1/128$ [circles] and (b) at $T = 1/128$ for $\Delta = 0.5$ [circles] and 1.0 [triangles]. Inset in (a): Details in the coexistence region. Data for $T = 1/64$, diamonds; $T = 1/128$, circles. Data obtained via increasing U , filled symbols; decreasing U , open symbols.

and a nonzero staggered charge density. Such tendencies become stronger as Δ grows.

As the interaction strength is increased, both the double-occupancy and the staggered charge density decrease monotonically with the imbalance between the two sublattices becoming weaker. In the MI phase, the staggered charge density is close to 0. However, the sublattice symmetry is broken in the Hamiltonian of the IHM and the staggered charge density does not exactly vanish for any finite U .

In the coexistence region, the metallic phase always exhibits higher values of the staggered charge density and double-occupancy than those in the MI phase. The data at two temperatures, $T = 1/64$ and $1/128$, are compared in the insets in Figs. 5.3 and 5.4. It is observed that the coexisting region widens as the temperature is lowered. Further, the critical interaction strength is shown to increase with the staggered lattice potential.

5.3.3 Energy density

Here we attempt to analyze the competition of the phases in terms of energy densities. At finite temperatures the free energy will also have the contribution of the entropy. We expect that the energy analysis given below is still valid for explaining the qualitative behaviors at low temperatures considered. The DMFT solution gives the total, kinetic, lattice potential, and interaction

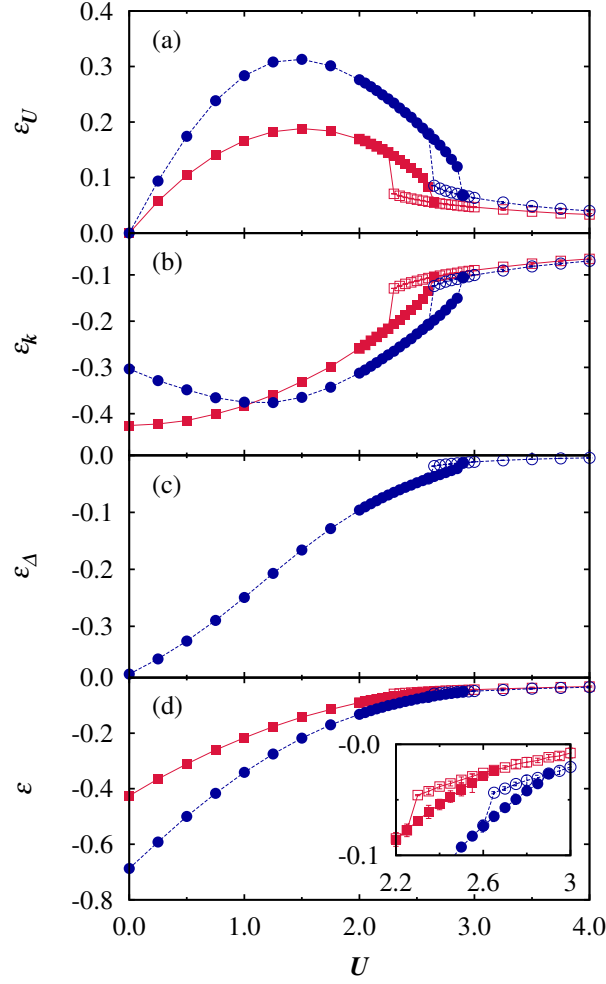


Figure 5.5: Energy densities as functions of U at temperature $T = 1/128$ and $\Delta = 0.5$. (a) Interaction energy ε_U , (b) kinetic energy ε_k , (c) staggered lattice potential energy ε_Δ , and (d) total energy ε (see text for definitions). The circles and squares represent data for the IHM and the HM, respectively. Inset in (d): Total energy density in the coexisting region; DMFT solutions obtained via increasing U (filled symbols) and decreasing U (open symbols).

energies per site in the forms:

$$\begin{aligned}
\varepsilon &= \varepsilon_k + \varepsilon_\Delta + \varepsilon_U, \\
\varepsilon_k &= \frac{T}{2} \sum_{\alpha\sigma} \langle k_{\alpha\sigma} \rangle, \\
\varepsilon_\Delta &= \frac{\Delta}{2} (n_A - n_B), \\
\varepsilon_U &= U d_O,
\end{aligned} \tag{5.10}$$

where $\langle k_{\alpha\sigma} \rangle$ is the average perturbation order of the spin σ electron at the impurity of sublattice α . This can be directly measured from CTQMC simulations [11, 20, 82].

In Fig. 5.5 we plot all four energy densities for $\Delta = 0.5$, together with those in the HM. Comparison between HM and IHM results indicates that for weak interactions, the gain in the staggered lattice potential energy exceeds the sum of the loss of both interaction and kinetic energies. In consequence, the total energy of the IHM is lower than that of the HM, which agrees with the characteristic behavior of the BI.

In the metallic region, the kinetic and interaction energies of the IHM behave qualitatively the same as those of the HM. Quantitatively, the kinetic energy of the IHM is, in general, lower than that of the HM with the same interaction strength. We also observe that the kinetic energy increases with the interaction strength U , which is in sharp contrast to the generally decreasing behavior in the BI. Such different behaviors of the metal and the BI give rise to a minimum of the kinetic energy at the interaction strength which generally coincides with the boundary between the BI and the metal.

In the MI phase, the staggered lattice potential energy becomes negligible; as a result, the total energy difference between the HM and the IHM decreases significantly and monotonically as the interaction strength U is increased. At the boundary between the MI and the metal, a first-order Mott transition is also present in the IHM. The critical interaction strength increases when the staggered lattice potential is introduced. In the coexistence region, the total energy density in the metallic phase is always lower than that in the MI phase, which also holds in the case of the HM [4]. We expect that at zero temperature the IHM also undergoes a continuous phase transition between the MI and the metal at the critical strength U_{c2} .

5.3.4 Finite-temperature phase transition

Based on the spectral properties as well as the local quantities, we may now construct the phase diagram of the IHM. Figure 5.6 exhibits the phase diagram for $\Delta = 0.5$ on the plane of the temperature T and the interaction strength U . There exist three phases: metal, BI, and MI. The BI and metal are connected through a crossover region while a first-order Mott transition separates the metal from the MI.

As shown in Fig. 5.1(b), the onset of \tilde{A} becomes steeper as the temperature is lowered. Accordingly, at zero temperature, the transition between the BI and the metal is expected to be continuous with a kink in \tilde{A} . In order to estimate the crossover interaction strength U_{co} at low temperatures, we obtain a best linear fit of the area in which \tilde{A} grows rather linearly in the metallic region.

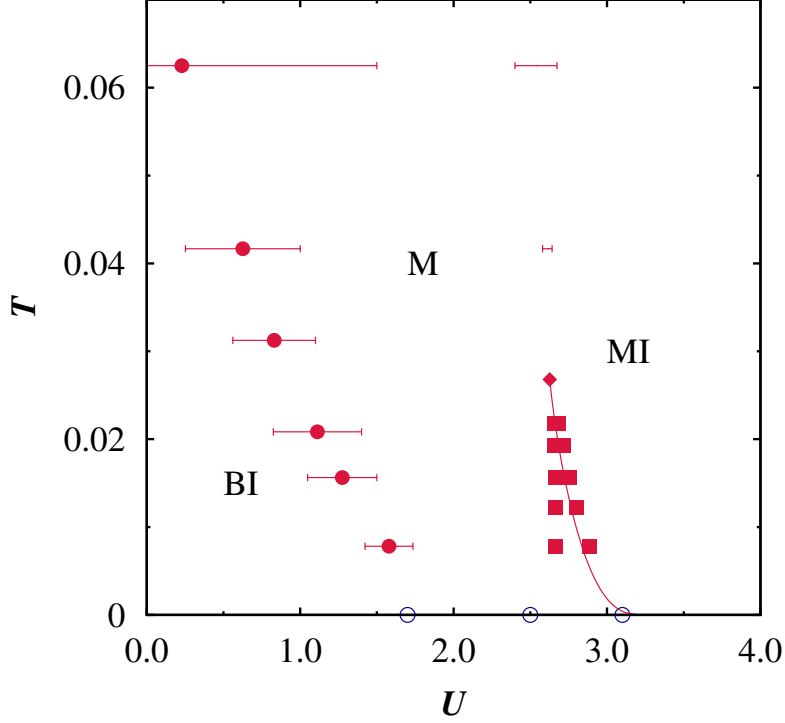


Figure 5.6: Phase diagram for $\Delta = 0.5$ on the plane of T and U . Filled circles and surrounding horizontal bars indicate the crossover strength U_{co} and estimated crossover regions, respectively. Two transition points for the Mott transition, U_{c1} and U_{c2} , are plotted by squares for various temperatures. The critical point of the Mott transition is represented by diamonds, along with the first-order transition line. Regions of the band insulator (BI), metal (M), and Mott insulator (MI) phases. The three open circles on the horizontal axis correspond to U_{co} , U_{c1} , and U_{c2} , respectively, obtained from NRG-DMFT at zero temperature (Ref. [76]).

We then estimate U_{co} by the intersection point of the fitting line and $\tilde{A}=0$. The half-width of the crossover region is also identified as the distance from U_{co} to the linear region. As the temperature is raised, the resulting U_{co} tends to decrease and the width of the crossover-region increases. It is also notable that U_{co} estimated via CTQMC-DMFT in this work gradually approaches the zero-temperature value obtained via NRG-DMFT [76].

At low temperatures we observe the coexistence region of the BI and metal between U_{c1} and U_{c2} , which can be identified by spectral functions and local quantities such as double-occupancy and staggered charge densities. With an increase in the temperature, U_{c1} and U_{c2} become closer, and the coexistence region ceases to exist at a certain critical temperature, above which the transition between the MI and the metal also appears as a crossover. These general features are rather similar to those of the Mott transition in the HM. Further, the extrapolation of U_{c1} and U_{c2} to zero temperature is quite consistent with that of NRG-DMFT results [76].

By solving the differential equations constructed from the free-energy analysis, we can obtain the first-order phase transition line, which is denoted by the solid line in Fig. 5.6. Using the thermodynamic relation

$$\left. \frac{\partial(\beta f)}{\partial \beta} \right|_U = \varepsilon , \quad (5.11)$$

we construct the differential equation of the interaction strength U_c of the

first-order transition as a function of T ,

$$\frac{dU_c(T)}{dT} = \frac{\delta\varepsilon(T, U)}{T\delta d_O(T, U)} , \quad (5.12)$$

with Δ being fixed. Here f is the free-energy density and $\delta\varepsilon$ and δd_O are the differences in the energy and the double-occupancy between metal and MI in the coexistence region, respectively. The numerical integration of Eqn. (5.12) gives the first-order transition line. The CTQMC procedure has the advantage that one can obtain the quantities necessary for the differential equations directly from Monte Carlo sampling without any further approximation. The details of the method can be found in Ref. [82], where the HM is investigated by the same method. The resulting transition line is plotted by the solid line in Fig. 5.6. The phase transition point at zero temperature is very close to U_{c2} obtained from NRG-DMFT, implying that the transition is continuous at zero temperature; this is also the case in the HM without a staggered lattice potential.

5.3.5 Nature of the intermediate metallic phase

One interesting issue is the nature of the metallic phase present in the region of intermediate interaction strengths. The metallic phase, which is driven by correlations from the BI, displays a peculiar pseudo-gap-like structure in the spectral function near the Fermi level, as demonstrated in Fig. 5.2. Such features raise the question whether the phase exhibits Fermi-liquid behavior.

According to the Fermi-liquid theory, the total energy density ε is propor-

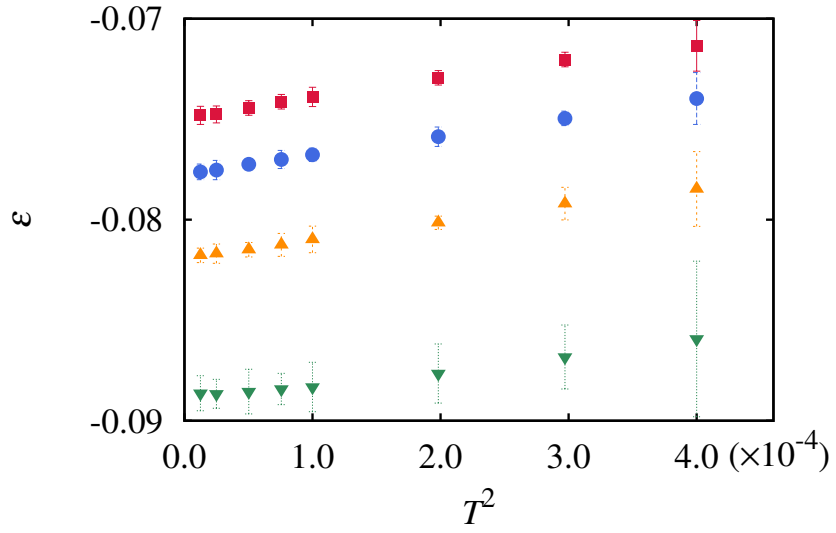


Figure 5.7: Total energy density ε as a function of temperature T . From top to bottom, the staggered lattice potential and interaction strength are given by $(\Delta, U) = (0, 2.2)$ (squares), $(0.5, 2.5)$ (circles), $(1, 3.2)$ (triangles), and $(3, 6.9)$ (inverted triangles). The horizontal axis is drawn on the scale of T^2 .

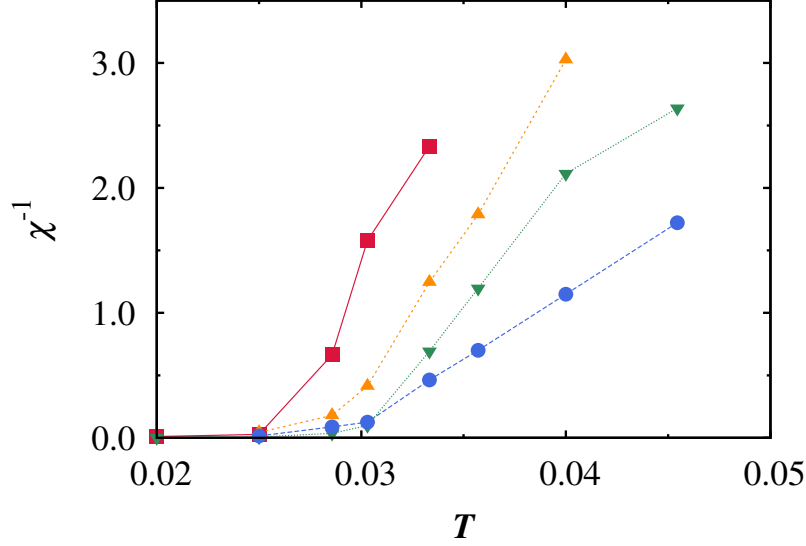


Figure 5.8: Inverse susceptibility χ^{-1} versus temperature T for the staggered lattice potential $\Delta = 0.5$ [squares], 1.0 [triangles], 3.0 [inverted triangles], and 5.0 [circles].

tional to T^2 at low temperatures. As a relevant check, we calculate the total energy density at various temperatures and show the results in Fig. 5.7 for various values of Δ . Indeed ε appears to be proportional to T^2 within statistical errors for all values of Δ examined and we presume that the metallic phase appearing in the IHM is a Fermi liquid. In addition, we have also computed the imaginary part of the self-energy, to find that the quasi-particle has an infinite lifetime at the Fermi level; this is also consistent with the Fermi-liquid picture.

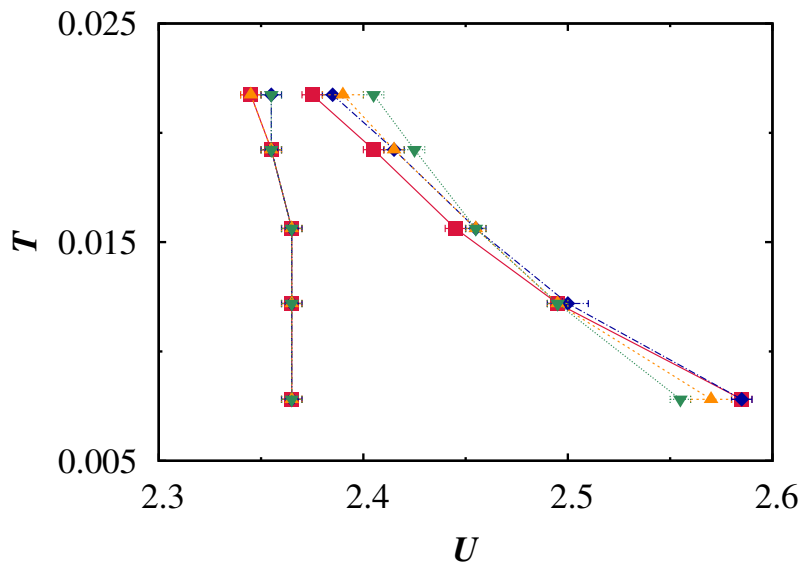


Figure 5.9: Coexistence region for $\Delta = 0.5$ (diamonds), 1.0 (triangles), and 3.0 (inverted triangles). For clear comparison with the Hubbard model [represented by squares], data for $\Delta = 0.5, 1.0$, and 3.0 are shifted to the left by the amount $\delta U = 0.3, 1.0$, and 4.69, respectively.

5.3.6 Critical point of the Mott transition

In this subsection, we consider how the phase diagram depends on the staggered lattice potential Δ . Specifically, we compute the critical temperature T_c of the Mott-Hubbard transition for various values of Δ . One way of obtaining T_c is to utilize the divergence of the susceptibility at the critical point. By analogy with a fluid system [23], we define the susceptibility as

$$\chi \equiv \text{Max}_U \left| \frac{\partial d_O}{\partial U} \right| \quad (5.13)$$

at given temperature T . In view of the divergence at the critical point, one can identify the critical temperature as the temperature where the inverse susceptibility vanishes. In Fig. 5.8 we plot the inverse susceptibility χ^{-1} versus temperature T for several values of Δ . For given Δ , as the temperature is lowered, the inverse susceptibility decreases and eventually vanishes, from which the critical temperature can be estimated. Figure 5.8 illustrates that the critical temperature generally increases with the strength of the staggered lattice potential.

We can reach a similar conclusion when we consider the critical interaction strengths U_{c1} and U_{c2} directly. As demonstrated in Fig. 5.9, variations in U_{c1} with temperature T are rather insensitive to the value of Δ , while the increase in Δ suppresses the change in U_{c2} with the temperature. This implies that the critical point is located at higher temperatures for larger values of Δ .

5.3.7 Phase diagram at low temperatures

Figure 5.10 depicts three regions, corresponding to the BI, metal, and MI phases on the plane of Δ and U at temperature $T=1/128$, which is the lowest temperature examined. We can observe two prominent differences between the resulting phase diagram and the two zero-temperature phase diagrams obtained in IPT-DMFT studies [74, 75].

First, in our phase diagram the crossover interaction strength U_{co} increases gradually from 0 as Δ is turned on. This is quite in contrast with the rather drastic increase for small Δ in Ref. [74]. Further, here the width of the metallic

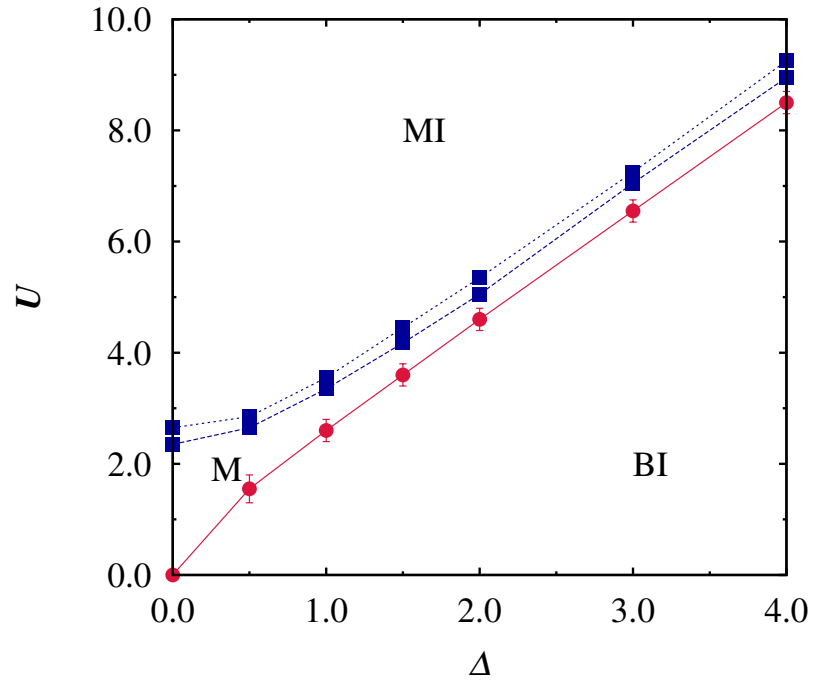


Figure 5.10: Phase diagram on the plane of Δ and U at temperature $T = 1/128$. band insulator (BI), metal (M), and Mott insulator (MI) phases. The squares represent U_{c1} and U_{c2} of the Mott transition. The circles and vertical bars describe U_{co} and the crossover region between the BI and the metal.

region apparently remains constant above $\Delta = 2$, which suggests that the metallic phase should extend to high values of Δ . We have indeed confirmed its existence even for $\Delta = 8$. This qualitatively contradicts the existing prediction that the metallic phase would cease to exist around $\Delta = 1.5$, beyond which a coexistence region between the BI and the MI develops [75]. At this stage the origin of the discrepancy is not clear and its resolution may require further study.

5.4 Summary

We have studied the IHM in infinite dimensions by means of the DMFT combined with the CTQMC method. The dependence of the double-occupancy and the staggered charge density on the interaction strength as well as the Fermi-level spectral weight exhibits crossover behavior from a BI to a metal and, subsequently, a transition to an MI. The transition to an MI is of the first order, and the critical temperature has been found to be higher for stronger staggered lattice potentials. Analyzing the temperature dependence of the energy density, we have shown that the intermediate metallic phase is a Fermi liquid. Finally, when the staggered lattice potential is strong, this metallic phase has been found to persist even at very low temperatures.

Chapter 6

Orbital Selective Mott Phase and Finite Temperature Transitions

6.1 Introduction

Coexistence of strongly and weakly correlated electrons has been one of the intriguing subjects in condensed matter physics. Materials in which more than one orbital are active near the Fermi level have exhibited interesting properties and their main origin is believed to be the coexistence of electrons with different degrees of correlations [83]. In the multi-orbital system, electron correlations and Hund's coupling have been known to show rich phenomena in the presence of the orbital degree of freedom. In case that the degeneracy between active orbitals is lifted by the difference of their bandwidths [84–94] or crystal-field splitting [95–99], the degree of effective correlations in each orbital becomes different. One prominent consequence of different degrees of correlations is

the orbital-selective Mott phase (OSMP), where electrons in some orbitals are totally localized due to the Mott physics while other orbitals are still occupied by itinerant electrons [100, 101]. Here Hund’s coupling tends to intensify the difference between orbitals [83, 102].

The coexistence of strongly and weakly correlated electrons is also believed to play an important role in two-dimensional materials including strong spatial fluctuations [103, 104]. In such a system spatial correlations and corresponding momentum-space anisotropy of correlations are the key elements to host the coexistence [81]. Thanks to the recent numerical developments in the cluster dynamical mean-field theory (DMFT) [14, 105–108], it is known that the spatial fluctuations modify qualitatively finite-temperature behaviors of the correlation-driven metal-insulator transitions; this has been revealed by the comparison with the single-site DMFT [4] neglecting spatial fluctuations. The spatial correlations turn out to reduce greatly the ground-state entropy of the paramagnetic Mott insulator (MI) at low temperatures and accordingly, the itinerant bad metallic phase dominates in the region of relatively high temperatures near the transition [109].

It is natural to anticipate such prominent changes in finite-temperature transitions for multi-orbital systems. In spite of extensive studies [92–97, 110–113], the temperature dependence of the transitions in the two-orbital Hubbard model still lacks a thorough understanding. The principal purpose of this work is to investigate the finite-temperature nature of the transitions in two-orbital systems with emphasis on the effects of Hund’s coupling.

In this chapter we investigate the two-orbital Hubbard model by the dy-

namical mean-field theory combined with the continuous Monte Carlo method. In the model we find the reverse-sloped Mott transition in the presence of Ising-type Hund's coupling for two orbitals of different bandwidths. We also observe that the drastic changes in the phase transition between the OSMP and the MI phase are induced by the variation of the Hund's coupling strength. The analysis of the hysteresis behavior of local magnetic moments determines the location of the critical end points, which reveals that the critical temperature tends to reduce as the Hund's coupling is increased. Eventually the hysteretic behavior disappears at a certain value of Hund's coupling and the system exhibits only a crossover between the OSMP and the MI phase.

This chapter is organized as follows: In Sec. 6.2 we give a brief description of the two-orbital Hubbard model and the numerical method. Section 6.3 is devoted to the presentation of the numerical results, which include finite-temperature phase diagrams, spectral functions, hysteresis of local magnetic moments, and effects of Hund's coupling. The results are summarized in Sec. 6.4.

6.2 Model and methods

We consider the Hamiltonian

$$\begin{aligned} \mathcal{H} = & - \sum_{\langle ij \rangle \alpha \sigma} t_{\alpha} (c_{i\alpha\sigma}^{\dagger} c_{j\alpha\sigma} + h.c.) - \mu \sum_{i\alpha\sigma} n_{i\alpha\sigma} \\ & + U \sum_{i\alpha} n_{i\alpha\uparrow} n_{i\alpha\downarrow} + \sum_{i\sigma\sigma'} (U' - J\delta_{\sigma\sigma'}) n_{i1\sigma} n_{i2\sigma'}, \end{aligned} \quad (6.1)$$

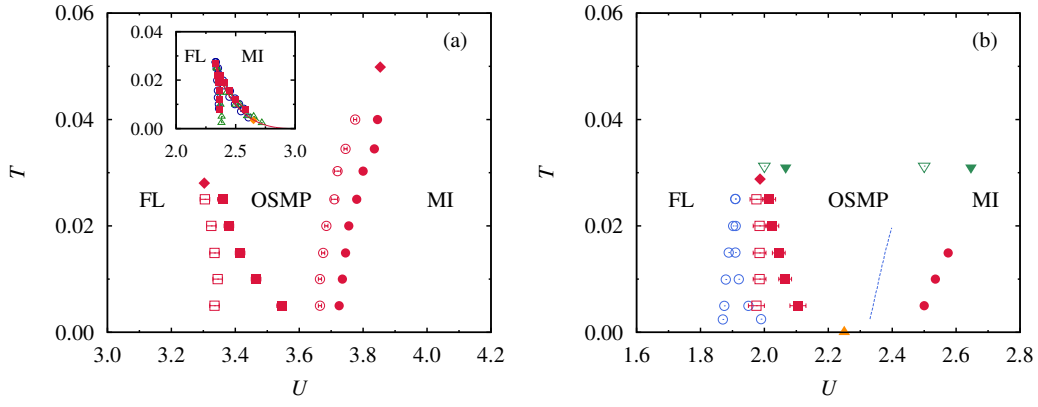


Figure 6.1: Phase diagrams on the plane of temperature T and interaction strength U for (a) $J = U/16$ and (b) $J = U/4$. (a) Open and filled symbols correspond to lower and upper critical interaction strengths, respectively. The transitions for narrow and wide orbitals are denoted by squares and circles, respectively. The inset in (a) exhibits the critical interaction strength of the single-orbital Hubbard model. (b) Lower [open squares] and upper [filled squares] critical interaction strengths of the narrow orbital transition and the phase boundary [filled circles] within the crossover region between the OSMP and the MI phase. The open circles as well as the dashed line represent the result of finite-temperature ED (Ref. [94]) while that of zero-temperature ED (Ref. [88]) is represented by the filled triangle. The results from the HF-QMC method in Refs. [92] and [110] are marked by open and filled inverted triangles, respectively. The diamonds in both (a) and (b) represent the critical end points of first-order transitions.

for two orbitals $\alpha = 1$ and 2 . Here, $c_{i\alpha\sigma}$ ($c_{i\alpha\sigma}^\dagger$) is the annihilation (creation) operator of an electron with spin σ at site i and orbital α . In each orbital electrons move on the infinite-dimensional Bethe lattice corresponding to a noninteracting semi-circular density of states (DOS), $\rho_\alpha^0(\omega) = (2/\pi D_\alpha)\sqrt{1 - (\omega/D_\alpha)^2}$, with the half bandwidth $D_\alpha = 2t_\alpha$ and interact with each other via the intra- and inter-orbital Coulomb interactions U and U' and Hund's coupling J . We investigate the half-filled system with chemical potential $\mu = 3U/2 - 5J/2$, and also choose $D_2 = 2D_1$ and $U' = U - 2J$. Here we disregard spin-flip and pair-hopping terms, which is appropriate for the study of the anisotropic Hund's coupling model.

We employ the DMFT combined with the continuous-time quantum Monte Carlo (CTQMC) method through the hybridization expansion algorithm [11, 12, 96]. Typically, the statistical sampling of 10^8 Monte Carlo steps is performed, which turns out to be sufficient for statistically reliable numerical results.

6.3 Results

6.3.1 Finite-temperature phase diagram

The main result of this work is the appearance of a *reverse-sloped* Mott transition accompanied by the drastic change in the behavior of finite-temperature phase transitions, which is driven by the variation in Hund's coupling. Figures 6.1(a) and (b) show phase diagrams on the temperature versus interaction strength plane for two typical values of Hund's coupling. In both cases two

successive phase transitions with the intermediate OSMP appear in the presence of orbital degrees of freedom. The transition between the Fermi liquid (FL) phase and the OSMP inherits the shape and energy scale of the coexistence region in the single-orbital model. In Fig. 6.1(a), on the other hand, the coexistence region of the OSMP-to-MI phase transition is quite interesting. First of all, the slope of the phase-transition line is opposite to that in the single-orbital case shown in the inset of Fig. 6.1(a). The reverse-sloped Mott transition was reported in the two-dimensional systems and its origin was attributed to spatial modulations [109]. Here it is noted that our system is an infinite-dimensional one without any spatial fluctuations. We can also find that the critical temperature associated with the reverse-sloped transition is considerably enhanced.

The effects of Hund's coupling are rather drastic on the reverse-sloped Mott transition. When we increase the Hund's coupling strength to $J = U/4$, the reverse-sloped Mott transition becomes a finite-temperature crossover, implying a continuous transition at zero temperature. Such a change in the zero-temperature transition was reported in an effective low-energy model [114]; our result reveals that it reflects the change from the reverse-sloped transition to a crossover at finite temperatures. In addition, the region of the OSMP, which is present between the two transitions, becomes wider for larger Hund's coupling strength, from which we can infer that Hund's coupling plays the role of a 'band decoupler' [102]. In Fig. 6.1(b) we also plot the existing results obtained from exact diagonalization (ED) [88, 94] and Hirsch-Fye quantum Monte Carlo (HF-QMC) [92, 110], which are reasonably consistent with our

data.

The reversed slope of the phase-transition line is a distinctive feature. In a conventional Mott transition the localized MI phase dominates the itinerant FL phase in the region of high temperatures near the phase transition; this is mainly due to the extensive entropic contribution of the MI phase compared with the very small ground-state entropy in the FL phase. Similarly to the reverse-sloped transition in two-dimensional systems, the origin of which is the significant reduction of the MI phase by the short-range correlations [109], the reverse-sloped Mott transition in the two-orbital system can be understood in terms of the entropy of the MI phase: It is expected to reduce considerably through ferromagnetic correlations between electrons in different orbitals by Hund's coupling. Another important aspect in the two-orbital system is that instead of the FL phase, the OSMP competes with the MI phase near the transition. The OSMP, in which electrons are partly localized, has higher entropy than the FL, and accordingly it is more likely to dominate the MI phase at high temperatures to yield the reversed slope of the transition line.

6.3.2 Spectral function and self-energy

The local spectral function of each orbital, which can be evaluated via an analytic continuation to the real-frequency domain by the maximum entropy method (MEM), characterizes conveniently the feature of each phase in the phase diagram. In the left panel of Fig. 6.2, the spectral functions of three different phases are shown for $J = U/16$. In the FL phase with $U = 3.0$, the

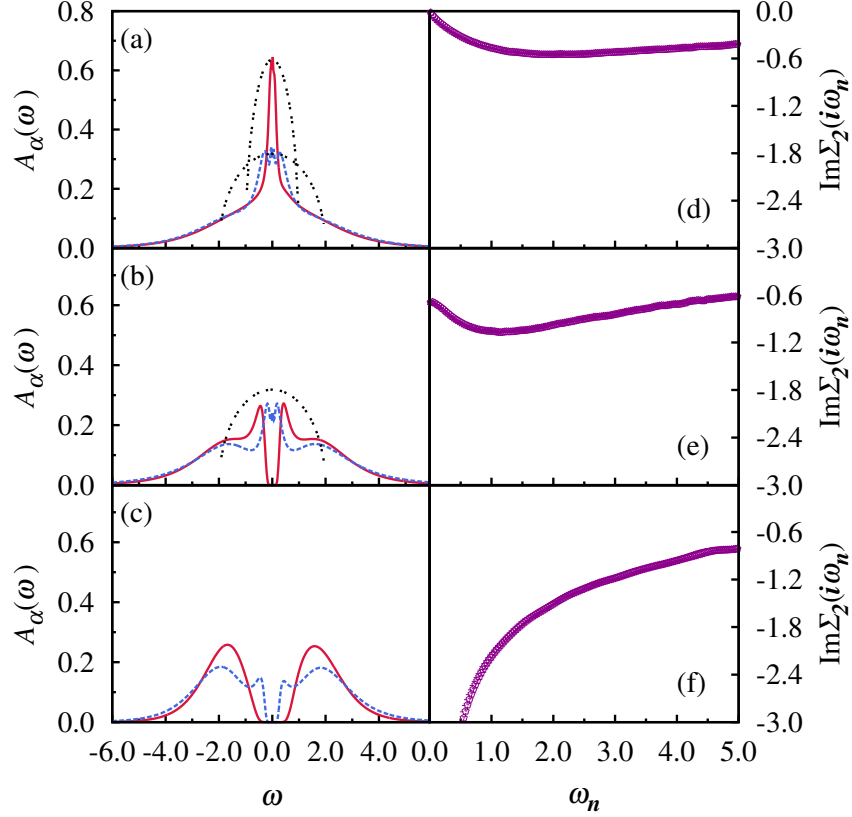


Figure 6.2: Spectral functions calculated via the maximum entropy method [(a) to (c)] and imaginary-part self-energies of wide-orbital electrons [(d) to (f)] at $T = 1/200$ for $J/U = 1/16$. From top to bottom, the interaction strength corresponds to $U = 3.00$ [(a) and (d)], 3.60 [(b) and (e)], and 4.00 [(c) and (f)]. In (a) to (c), the solid and dashed lines represent the spectral functions of narrow and wide orbitals, respectively. For comparison, the noninteracting density of states, marked with the dot-dashed line, is also shown in (a) (both orbitals) and (b) (wide orbital).

spectral function exhibits clearly a coherent peak, which satisfies the Luttinger theorem. On the other hand, the coherent peak disappears and Mott gaps develop for both orbitals in the MI phase. For the intermediate interaction strength corresponding to OSMP, the narrow orbital is gapped while the wide one still remains itinerant. It is remarkable that the spectral function of the wide orbital deviates substantially from the noninteracting DOS at the Fermi level. The violation of the Luttinger theorem implies the finite lifetime of wide-orbital electrons at the Fermi level. The finite-scattering amplitude of the wide-orbital electron at the Fermi level can be verified by the finite offset in the imaginary-part of the self-energy, as shown in Fig. 6.2(e). Similar evidences were also reported for the non-Fermi-liquid nature of the OSMP which crosses over to the MI phase [112, 113].

6.3.3 Local magnetic moments

The first-order transition between the MI and the OSMP is demonstrated by the hysteresis behavior of physical quantities such as the local magnetic moment. In Fig. 6.3 we plot the local magnetic moment of the wide orbital as a function of U for different temperatures. As the interaction strength is increased, electrons become more localized and the average local moment increases monotonically. Over a finite region of the interaction strength we can observe the hysteresis of the local spin magnetic moment, which implies the coexistence of the two phases. As shown in Fig. 6.3, we can estimate two critical interaction strengths U_{c1} and U_{c2} from the minimum and the maximum values

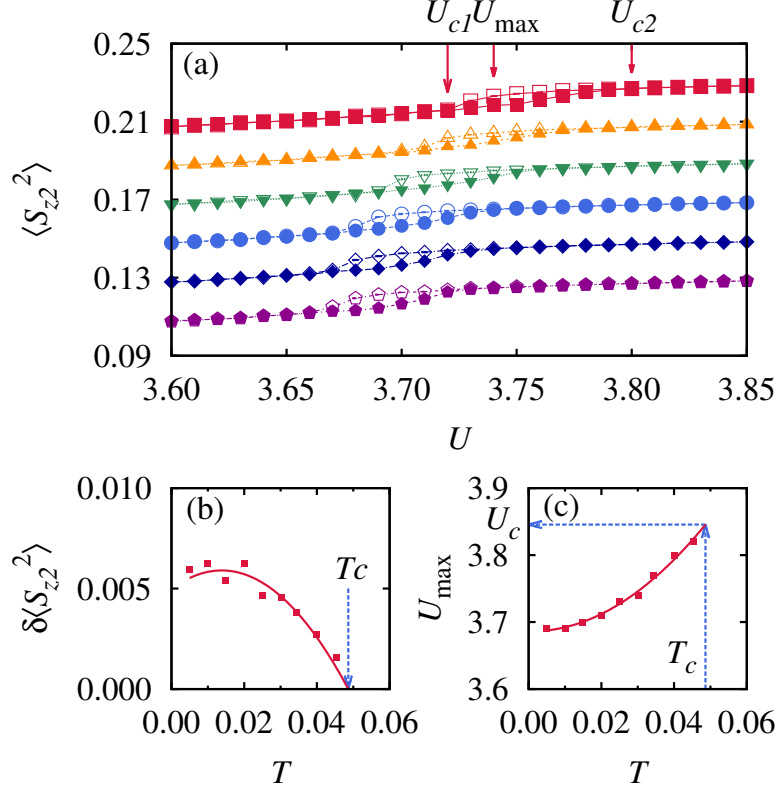


Figure 6.3: (a) Squared magnetic moments of wide-orbital electron as a function of the interaction strength at various temperatures for $J/U = 1/16$. From top to bottom, corresponding temperatures are $T = 1/33, 1/40, 1/50, 1/67, 1/100$, and $1/200$. For better comparison, the data for $T = 1/40, 1/50, 1/67, 1/100$, and $1/200$ are shifted downward by 0.02, 0.04, 0.06, 0.08, and 0.10, respectively. Lines are guides to the eye. (b) Maximum differences of the squared magnetic moments between two solutions in the coexistence region at given temperatures. The solid line corresponds to the least-square fit of the data. The critical temperature T_c is estimated by the T -axis cut of the extrapolated line, which is denoted by the dotted arrow. (c) Interaction strength U_{\max} at which the difference reaches the maximum. The critical interaction strength U_c is estimated by the extrapolation of the least-square fit [solid line] to the critical temperature [dotted vertical arrow].

of U , respectively, showing the coexistence. The coexistence region shifts to the stronger interaction region with the increase of the temperature, resulting in the reversed slope of the phase-transition line.

Using the above hysteresis, we can also estimate the position of the critical end point of the reverse-sloped Mott transition. From the numerical data, we obtain the maximum difference of the local moments for the two solutions (MI and OSMP) in the coexistence region

$$\delta\langle S_{z2}^2 \rangle \equiv \text{Max}_U [\langle S_{z2}^2 \rangle_{\text{MI}} - \langle S_{z2}^2 \rangle_{\text{OSMP}}] \quad (6.2)$$

at each temperature. In the plot of $\delta\langle S_{z2}^2 \rangle$ as a function of T , the T -axis cut gives the critical temperature T_c , as shown in Fig. 6.3(b). The hysteresis data provide the interaction strength U_{max} , where $\delta\langle S_{z2}^2 \rangle$ reaches the maximum, and the extrapolated value of U_{max} to $T = T_c$ gives the interaction strength of the critical end point. [See Fig. 6.3(c).] We have thus determined the location of the critical end points for both first-order transitions, which are plotted in Fig. 6.1(a).

6.3.4 Effects of Hund's coupling

In Fig. 6.4 we summarize the effects of Hund's coupling on the transitions by plotting various transition interaction strengths versus J/U at $T = 1/200$, which is the lowest temperature considered. For $J/U = 1/64$, the system appears to undergo a single transition without the OSMP. For larger values of J/U , we can observe two separate transitions, and the region of OSMP

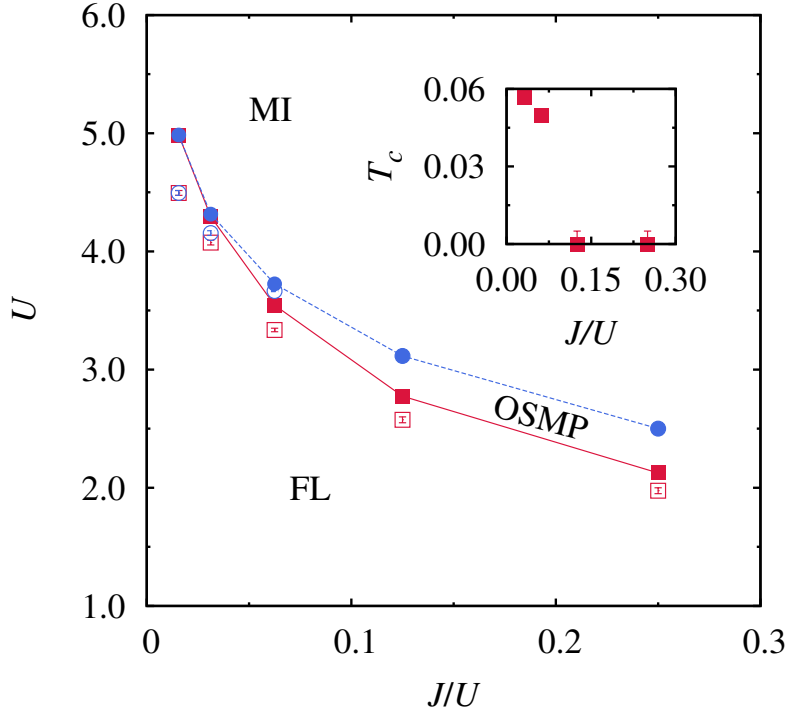


Figure 6.4: Phase diagram on the plane of the interaction strength U and the Hund's coupling strength J/U at temperature $T = 1/200$. Filled and open squares indicate upper and lower critical interaction strengths, respectively, of the narrow-orbital transition. For $J/U < 0.1$, the filled and open circles represent upper and lower critical interaction strengths of the wide-orbital transition. For $J/U > 0.1$, the crossover points between the OSMP and the MI phase are marked by the filled circles. Lines are guides to the eye. Inset: Critical temperature of the wide-orbital transition versus J/U .

expands gradually with the increase of J/U . It is also notable that the critical interaction strengths associated with both orbitals tend to decrease as Hund's coupling grows. As J/U is increased, the critical temperature of the wide-orbital first-order transition reduces. Above a certain value of J/U , which turns out to be between $1/16$ and $1/8$, we cannot find the transition down to $T = 1/200$, the lowest temperature considered, only to observe crossover phenomena.

6.4 Summary

In summary, we have found the reverse-sloped Mott transition in the two-orbital Hubbard model with Ising-type Hund's coupling, in which two orbitals have different bandwidths. The reversed slope of the phase-transition line between the OSMP and the MI phase can be understood in terms of entropy contributions. We have also observed drastic changes in transition nature between the OSMP and the MI as the Hund's coupling strength is varied. As the Hund's coupling strength increases, the first-order transition turns into a finite-temperature crossover, implying a quantum phase transition at zero temperature. The diminishing critical temperature of the first-order transition is presumed to be the underlying mechanism of the drastic change in transition nature.

Chapter 7

Magnetic Properties in the Bilayer Hubbard Model

7.1 Introduction

Two-dimensional bilayer Hubbard model is known to be relevant to several high- T_c superconducting materials such as $\text{Bi}_2\text{Sr}_2\text{CaCu}_2\text{O}_8$ and $\text{YBa}_2\text{Cu}_3\text{O}_7$ [115–117]. Since these materials are antiferromagnetic insulators in the undoped case, the bilayer effects on the magnetic properties are of great interest to understand the high- T_c superconductivity. The existence of magnetic ground state, however, is highly controversial due to the difficulties in numerical calculation of the system. Early cellular DMFT (CDMFT) [118] and determinant quantum Monte Carlo method (DQMC) [119] studies predicted the existence of paramagnetic metallic ground state in the weak interaction region while recent results from variational Monte Carlo method (VMC) [120], functional renormalization group (fRG), and projective DQMC (PDQMC) [121] showed

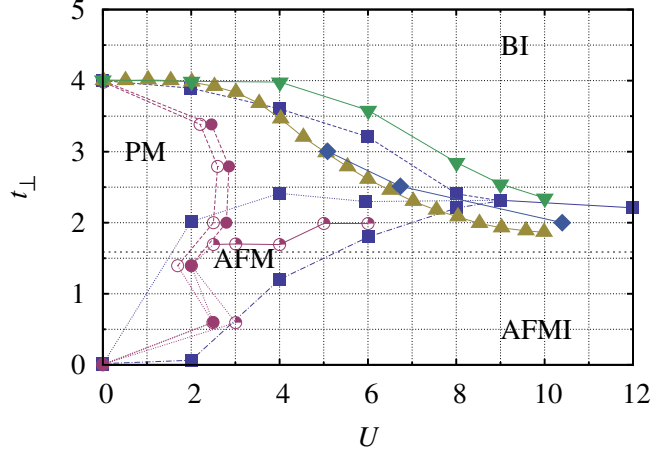


Figure 7.1: Phase diagrams obtained from previous studies. Squares and circles represent the CDMFT [118] and DQMC [119] results, respectively. Triangles, inverted triangles, and diamonds are obtained from VMC [120], fRG [121], and PDQMC [121], respectively. Band/singlet insulator (BI) and antiferromagnetic Mott insulator (AFMI) phase are observed by all previous results. The boundary between BI and AFMI is marked by solid lines. The CDMFT and DQMC results show the paramagnetic metal (PM) phase. Only CDMFT results shows the antiferromagnetic metal (AFM). The dashed lines represent the boundary between PM and AFMI. The dotted lines show the PM-to-AFM transition line in CDMFT results and the PM-to-AFMI transition line in DQMC results. The boundary between AFM and AFMI is marked by the dash-dotted line.

that the paramagnetic metal was absent. Figure 7.1 shows the phase diagrams obtained from previous studies.

Since the spatial fluctuation is believed to be the crucial factor in two dimensions, early DMFT studies employed its cluster extension, especially the cellular DMFT [118]. However, due to the high numerical cost of the calculation, this study can use only the 4-site cluster (2 sites for each layer)

which intrinsically breaks the rotational symmetry of the underlying lattice; this may give the uncontrolled effects in the calculation. As a resolution to this effect, we perform 8-site cluster study under the DCA which preserves the rotational symmetry in the underlying lattice. We concentrate on investigating the existence of the paramagnetic metal phase which is the central issue in the controversy.

7.2 Model

The bilayer Hubbard model is described by the Hamiltonian,

$$\begin{aligned}
\mathcal{H} &= \mathcal{H}_t + \mathcal{H}_U \\
&= -t \sum_{\langle ij \rangle l \sigma} (c_{il\sigma}^\dagger c_{il\sigma} + h.c.) - t_\perp \sum_{i\sigma} (c_{i1\sigma}^\dagger c_{i2\sigma} + c_{i2\sigma}^\dagger c_{i1\sigma}) - \mu \sum_{il\sigma} n_{il\sigma} \\
&\quad + U \sum_{il} n_{il\uparrow} n_{il\downarrow} ,
\end{aligned} \tag{7.1}$$

where $c_{il\sigma}$ ($c_{il\sigma}^\dagger$) is an annihilation (creation) operator of a σ -spin electron at the i th site in the l th layer ($l = 1, 2$). Here, t , t_\perp , and U represent the intra-, inter-layer hopping amplitude, and the on-site Coulomb interaction, respectively. Throughout this chapter, we use t as an energy unit. By the use of Fourier transformation

$$c_{\mathbf{k}l\sigma} = \frac{1}{\sqrt{N}} \sum_i c_{il\sigma} e^{-i\mathbf{k} \cdot \mathbf{x}_i} \tag{7.2}$$

with N being the number of sites of a single layer, the Hamiltonian can be expressed in the form of

$$\begin{aligned} \mathcal{H} = & \sum_{\mathbf{k}\alpha\sigma} \xi_{\mathbf{k}\alpha} c_{\mathbf{k}\alpha\sigma}^\dagger c_{\mathbf{k}\alpha\sigma} \\ & + \frac{U}{2N} \sum_{\alpha_1\alpha_2} \sum_{\mathbf{k}_1\mathbf{k}_2\mathbf{q}} \left(c_{\mathbf{k}_1\alpha_1\bar{\sigma}}^\dagger c_{\mathbf{k}_1+\mathbf{q}\alpha_1\bar{\sigma}} c_{\mathbf{k}_2\alpha_2\sigma}^\dagger c_{\mathbf{k}_2-\mathbf{q}\alpha_2\sigma} \right. \\ & \left. + c_{\mathbf{k}_1\alpha_1\bar{\sigma}}^\dagger c_{\mathbf{k}_1+\mathbf{q}\bar{\alpha}_1\bar{\sigma}} c_{\mathbf{k}_2\alpha_2\sigma}^\dagger c_{\mathbf{k}_2-\mathbf{q}\bar{\alpha}_2\sigma} \right) , \end{aligned} \quad (7.3)$$

where α is ± 1 corresponding to the bonding ($-$) and antibonding ($+$) index, and $\xi_{\mathbf{k}\alpha} = -2t(\cos k_x + \cos k_y) + \alpha t_\perp - \mu$. The bonding and anti-bonding operators are defined by

$$\begin{pmatrix} c_{i-} \\ c_{i+} \end{pmatrix} = \frac{1}{\sqrt{2}} \begin{pmatrix} c_{i1} + c_{i2} \\ c_{i1} - c_{i2} \end{pmatrix} . \quad (7.4)$$

Figure 7.2(a) shows a noninteracting band dispersion for $U = 0$ and $t_\perp = 0.8$. In this dispersion, the energy difference between the bonding and anti-bonding band for a given momentum is $2t_\perp$. As t_\perp increases, the system undergoes a metal-to-insulator transition at $t_\perp = 4t$. When $t_\perp > 4t$, the energy gap develops at the Fermi level and the system shows an insulating phase, called a singlet insulator. The corresponding Fermi surface in Brillouin zone is represented in Fig. 7.2(b). The Fermi surface shows a perfect nesting between the bonding and anti-bonding bands with the nesting wavevector $\mathbf{Q} = (\pi, \pi)$.

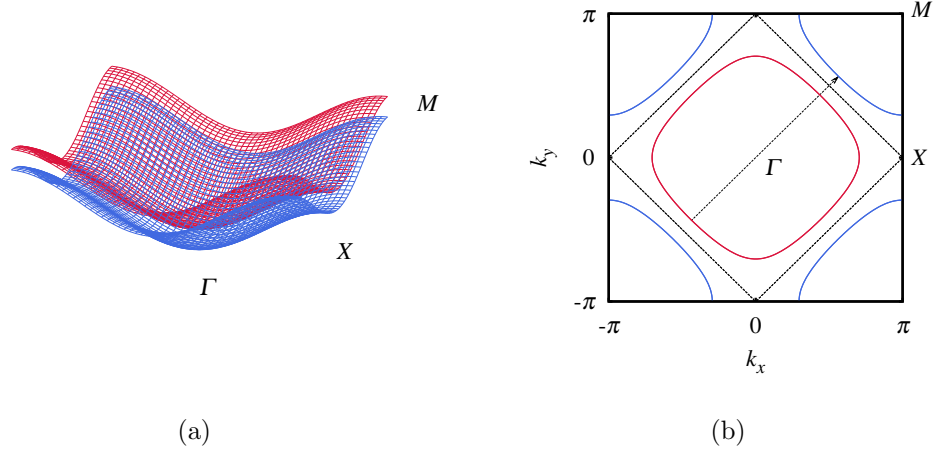


Figure 7.2: (a) Noninteracting energy dispersions of the bilayer Hubbard model for $t_{\perp} = 0.8$. Lower (upper) sheet corresponds to the bonding (anti-bonding) energy band. Γ , X , and M correspond to the high symmetry momentum point, $(0, 0)$, $(\pi, 0)$, and (π, π) , respectively. (b) Fermi surfaces of the noninteracting bilayer Hubbard model for $t_{\perp} = 0.8$. Outer (inner) line corresponds to the Fermi surface of the bonding (anti-bonding) band. The dotted arrow represents the nesting vector, $\mathbf{Q} = (\pi, \pi)$. The dashed line is the Fermi surface of the decoupled model, $t_{\perp} = 0.0$.

7.3 Results

7.3.1 Staggered magnetization

Figure 7.3 shows the staggered magnetization as a function of t_{\perp} . The staggered magnetization is defined by

$$m \equiv \frac{1}{2N} \sum_{il} (-1)^{i+l} (\langle n_{il\uparrow} \rangle - \langle n_{il\downarrow} \rangle) / 2, \quad (7.5)$$

For a given interaction strength U and temperature T , the staggered magnetization monotonically decreases as t_{\perp} increases and finally vanishes for a certain

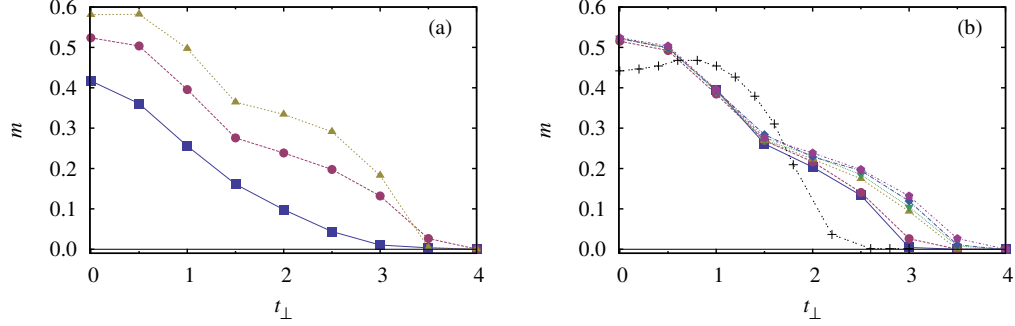


Figure 7.3: The staggered magnetization as a function of t_{\perp} for (a) $T = 0.05$ (b) $U = 4.0$. (a) From top to bottom, corresponding interaction strength values are 5.0, 4.0, and 3.0. (b) From top to bottom, corresponding temperatures are 0.05, 0.06, 0.07, 0.08, 0.09, and 0.10. Black cross-symbols denote to the CDMFT results at zero temperature.

critical value t_{\perp}^c . The critical interlayer hopping t_{\perp}^c tends to increase as the temperature decreases. In addition, we find that the temperature dependence of staggered magnetization is stronger in the region $1.5 < t_{\perp} \leq 3.0$ than that in the region $0 \leq t_{\perp} < 1.5$. The previous results obtained using the cellular DMFT [118] are qualitatively different from our results. In contrast to our monotonic decrease of staggered magnetization, the staggered magnetization exhibits a maximum at finite t_{\perp} . On the other hand, for a given interlayer hopping t_{\perp} and temperature T , the larger staggered magnetization is obtained for the larger interaction strength U .

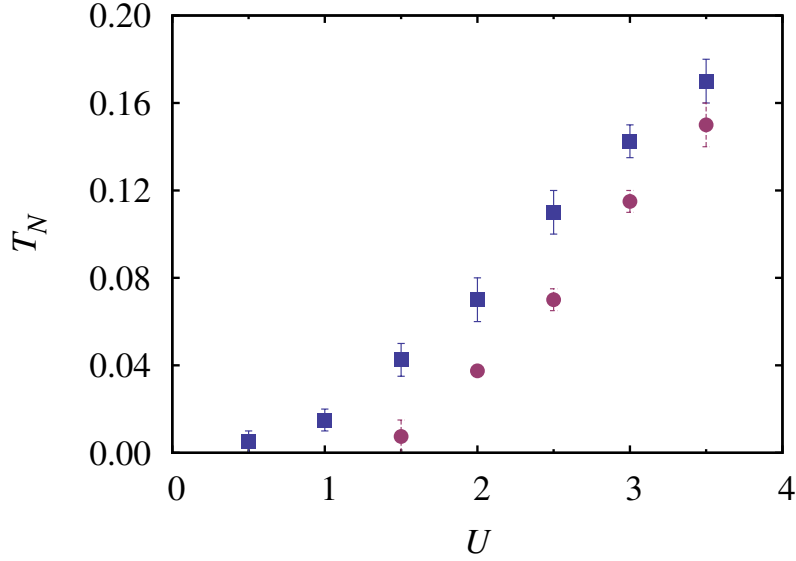


Figure 7.4: The Néel temperature as a function of U . From top to bottom, the corresponding t_{\perp} values are 0.0, and 1.5.

7.3.2 Néel temperatures

The Néel temperatures as a function of interaction strength are shown in Fig. 7.4. For the decoupled layer system, $t_{\perp} = 0$, starting from nonmagnetic limit for $U = 0.0$, the Néel temperature monotonically increases as interaction strength increases. When the interlayer hopping, however, is introduced, the Néel temperature is clearly suppressed. We find that the Néel temperature for $U \leq 1.5$ is smaller than $T = 1/50$ when $t_{\perp} = 1.5$ suggesting the existence of paramagnetic metal at zero temperature. We cannot rule out the possibility that the Néel temperature is exponentially small in this region.

7.3.3 Spin-resolved local spectral function

The spin-resolved local spectral functions are shown in Fig. 7.5 for $T = 0.05$ and $U = 4.0$. When $t_{\perp} \leq 2.5$, the spectral gap appears and the asymmetry between the up and down spin is clearly shown, which are characteristics of the antiferromagnetic insulator. As t_{\perp} increases, the size of magnetic gap monotonically reduces. At the certain critical value t_{\perp}^c , the magnetic insulator-to-band insulator transition occurs. For $t_{\perp} > t_{\perp}^c$, the band gap without the spin asymmetry appears, which is a signature of the singlet insulator.

7.4 Summary

We have investigated the magnetic properties of the bilayer Hubbard model on two-dimensional square lattice. We have adopted the dynamical cluster approximation combined with the continuous-time quantum Monte Carlo method. Compared with the single-layer model, the inter-layer hopping suppresses the Néel temperature. For the intermediate interaction strength, the AFMI-to-BI transition occurs at the certain critical inter-layer hopping amplitude. The value of the critical inter-layer hopping amplitude decreases as temperature increases. It will be interesting to investigate the doping effects in this system. The superconducting instability and the possibility of the exciton condensation upon doping were previously investigated within the DQMC scheme. Since the cluster DMFT could be the complementary method to the finite-lattice calculation, we expect that the results will add more interesting

physics to the existing results.

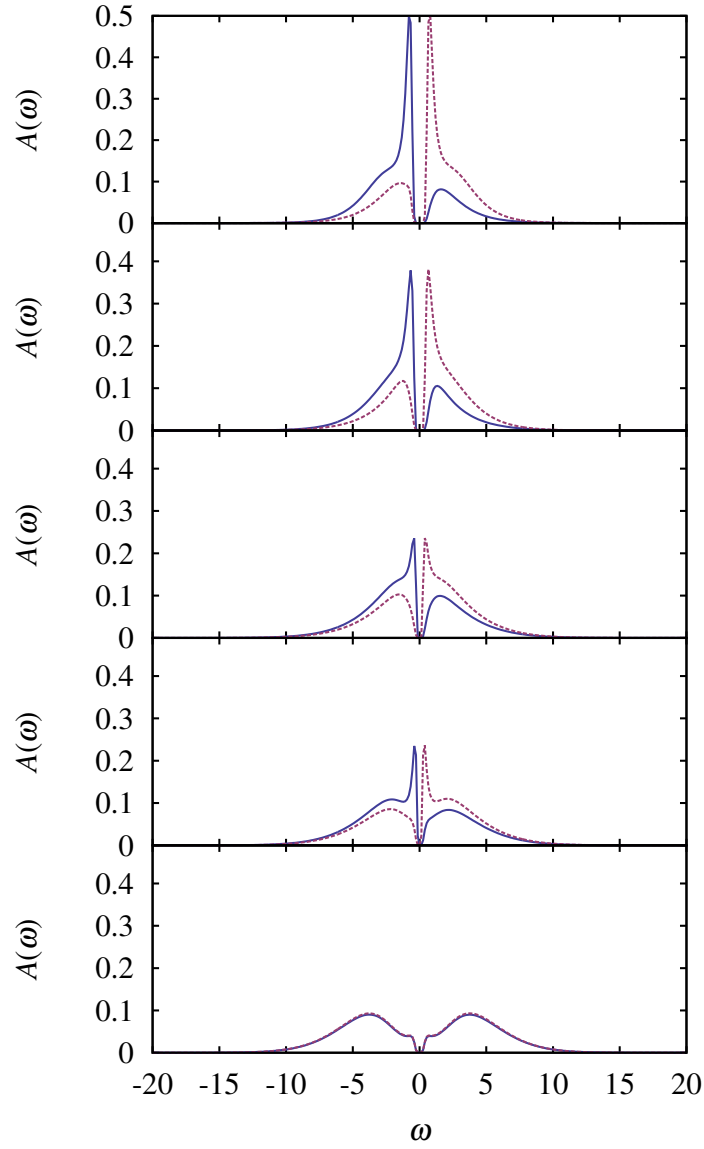


Figure 7.5: Spin-resolved local spectral functions for $U = 4.0$ and $T = 0.05$. Solid (dashed) line represents the spin-up (spin-down) components of A sublattice. From top to bottom, corresponding t_{\perp} values are 1.0, 1.5, 2.0, 2.5, and 4.0.

Chapter 8

Strongly Correlated Superconductivity

8.1 Introduction

In the high- T_c superconductors, the relation between antiferromagnetism and superconductivity is one of the central issues. It is regarded that the strong repulsive Coulomb interaction between electrons is important in both phenomena. Particularly in cuprate materials, the microscopic model to deal with the Coulomb interaction is the Hubbard model in the two-dimensional square lattice. In the strong interaction limit, the Hubbard model can be transformed into the t - J model which naturally shows antiferromagnetism via the exchange interaction. The other approach starts from the phenomenological consideration of the d -wave pairing in the cuprate superconductors. In this approach, the d -wave pairing is explicitly included in the BCS Hamiltonian and the effect of strong repulsive interaction is considered via the Gutzwiller projection. The

Gutzwiller-projected BCS model with d -wave pairing is a natural model.

The direct connection between these two seemingly different starting points had been explicitly shown in previous exact diagonalization studies [122, 123]. In these studies, the overlap between the ground states of two different models appears to be very high even in finite doping regions. The BCS+ U model is the natural generalization of the Gutzwiller projected BCS Hamiltonian, which spans more realistic parameter spaces. Even though previous DMFT studies of this model successfully showed the superconductor-to-insulator transition at half filling and the reemergence of superconductivity upon hole-doping [124], the non-local correlation effects were ignored within the assumption of the single-site DMFT. We now discuss the non-local correlation effects within the DCA. In addition, the effect of thermal fluctuations on the superconductivity is also being investigated. We expect that this study can enhance the comprehensive understanding of the correlation effect in the high- T_c superconductivity and its connection to antiferromagnetism.

8.2 Model

The BCS+ U model is defined by

$$\begin{aligned}
\mathcal{H} &= \mathcal{H}_t + \mathcal{H}_\Delta + \mathcal{H}_U \\
&= -t \sum_{\langle ij \rangle \sigma} (c_{i\sigma}^\dagger c_{j\sigma} + h.c.) - \mu \sum_{i\sigma} n_{i\sigma} \\
&\quad + \sum_{\langle ij \rangle} \Delta_{ij} (c_{i\uparrow}^\dagger c_{j\downarrow}^\dagger + c_{j\uparrow}^\dagger c_{i\downarrow}^\dagger + h.c.) \\
&\quad + U \sum_i n_{i\uparrow} n_{i\downarrow}, \tag{8.1}
\end{aligned}$$

where $\Delta_{ij} = +\Delta$ for $j = i + \hat{x}$ and $\Delta_{ij} = -\Delta$ for $j = i + \hat{y}$. Throughout this chapter, t is set to be an energy unit.

After Fourier transform, the Hamiltonian leads to

$$\begin{aligned}
\mathcal{H} &= \mathcal{H}_0 + \mathcal{H}_U \\
&= \sum_{\mathbf{k}} \begin{pmatrix} c_{\mathbf{k}\uparrow}^\dagger & c_{-\mathbf{k}\downarrow} \end{pmatrix} \begin{pmatrix} \xi_{\mathbf{k}} & \Delta_{\mathbf{k}} \\ \Delta_{\mathbf{k}} & -\xi_{-\mathbf{k}} \end{pmatrix} \begin{pmatrix} c_{\mathbf{k}\uparrow} \\ c_{-\mathbf{k}\downarrow}^\dagger \end{pmatrix} \\
&\quad + \frac{U}{N} \sum_{\mathbf{k}_1 \mathbf{k}_2 \mathbf{q}} c_{\mathbf{k}_1\uparrow}^\dagger c_{\mathbf{k}_1+\mathbf{q}\uparrow} c_{\mathbf{k}_2\downarrow}^\dagger c_{\mathbf{k}_2-\mathbf{q}\downarrow} \tag{8.2}
\end{aligned}$$

where $\xi_{\mathbf{k}} = -2t(\cos(k_x) + \cos(k_y)) - \mu$ and $\Delta_{\mathbf{k}} = 2\Delta(\cos(k_x) - \cos(k_y))$.

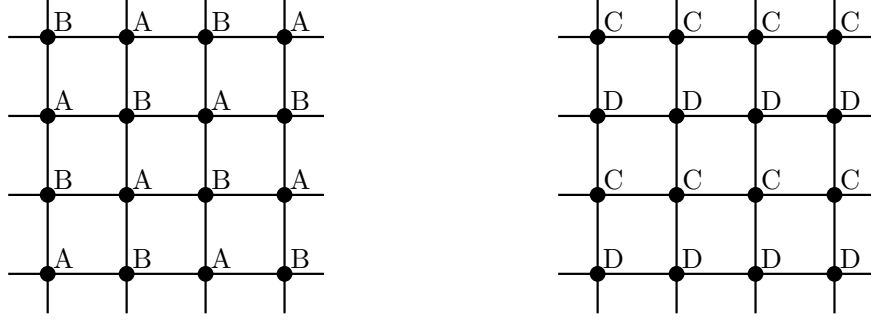


Figure 8.1: sublattice index for 2-dimensional square lattice.

8.3 Results

8.3.1 Duality of local Green function

We can find the dual character of the model Hamiltonian. Let's start by defining two unitary transforms \mathcal{T}_a :

$$\begin{pmatrix} c_{A\uparrow} \\ c_{A\downarrow} \\ c_{B\uparrow} \\ c_{B\downarrow} \end{pmatrix} \rightarrow \begin{pmatrix} c_{A\uparrow} \\ c_{A\downarrow} \\ -c_{B\downarrow}^\dagger \\ -c_{B\uparrow}^\dagger \end{pmatrix} \quad (8.3)$$

and \mathcal{T}_b :

$$\begin{pmatrix} c_{C\uparrow} \\ c_{C\downarrow} \\ c_{D\uparrow} \\ c_{D\downarrow} \end{pmatrix} \rightarrow \begin{pmatrix} c_{C\uparrow} \\ c_{C\downarrow} \\ -c_{D\uparrow} \\ -c_{D\downarrow} \end{pmatrix}, \quad (8.4)$$

where A, B, C, D are the sublattice indices shown in Fig. 8.1. For the half-filled system, the Hamiltonian $\mathcal{H}(t, \Delta, U)$ transforms by the successive unitary

transform, $\mathcal{T} \equiv \mathcal{T}_b \mathcal{T}_a$ as

$$\mathcal{H}(t, \Delta, U) \rightarrow \mathcal{H}(\Delta, t, U) . \quad (8.5)$$

Then the normal part of the local Green function can be represented by

$$\begin{aligned} G_{\uparrow}(i, \tau) \Big|_{\mathcal{H}(t, \Delta, U)} &= \frac{1}{Z} \text{tr} \left[e^{-\beta \mathcal{H}(t, \Delta, U)} c_{i\uparrow}(\tau) c_{i\uparrow}^{\dagger} \right] \\ &= \frac{1}{Z} \text{tr} \left[\mathcal{T}^{-1} \mathcal{T} e^{-\beta \mathcal{H}(t, \Delta, U)} \mathcal{T}^{-1} \mathcal{T} c_{i\uparrow}(\tau) \mathcal{T}^{-1} \mathcal{T} c_{i\uparrow}^{\dagger} \mathcal{T}^{-1} \mathcal{T} \right] \\ &= \begin{cases} G_{\uparrow}(i, \tau) \Big|_{\mathcal{H}(\Delta, t, U)} & i \in A \\ G_{\downarrow}(i, \beta - \tau) \Big|_{\mathcal{H}(\Delta, t, U)} & i \in B \end{cases} \\ &= G(i, \tau) \Big|_{\mathcal{H}(\Delta, t, U)} . \end{aligned} \quad (8.6)$$

On the forth line of Eqn. (8.6), we use the particle-hole symmetry of the Green function and assume that the system is in the paramagnetic phase.

Figures 8.2 and 8.3 represent the normal part of the Green functions computed from two different Hamiltonians which are dual to each other. The duality is valid within the numerical accuracy for every parameter set which we investigate. We can see that our numerical results reproduce well the local duality of the system.

8.3.2 Local Spectral Function for half-filled system

Using the maximum entropy method, we study the properties of the local spectral function (LSF) for the half-filled system. Figures 8.4 and 8.5 show the

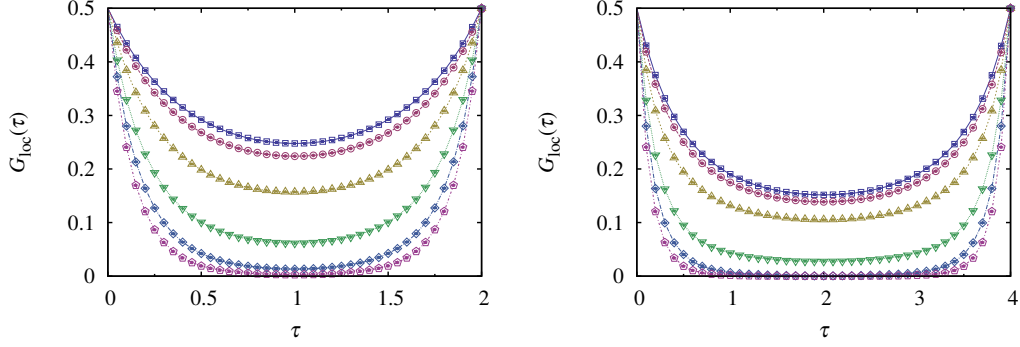


Figure 8.2: Imaginary-time local Green's function which displays the local duality of BCS+ U model for $N_c = 1$. The system is half-filled and the temperature of left (right) panel is $1/2$ ($1/4$). Open (closed) symbol represent the $t = 0$, $\Delta = 1$ ($t = 1$, $\Delta = 0$) case. From top to bottom, the corresponding interaction strengths are 0.0, 3.0, 6.0, 9.0, 12.0. and 15.0

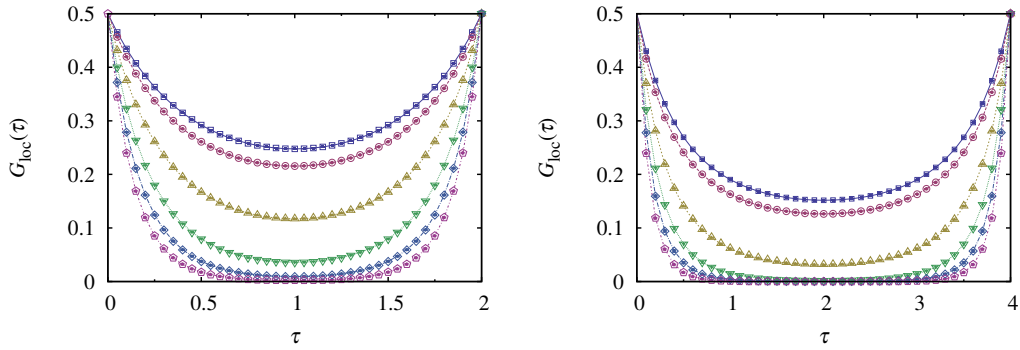


Figure 8.3: Imaginary-time local Green's function which displays the local duality of BCS+ U model for $N_c = 4$. The system is half-filled and the temperature of left (right) panel is $1/2$ ($1/4$). Open (closed) symbol represent the $t = 0$, $\Delta = 1$ ($t = 1$, $\Delta = 0$) case. From top to bottom, the corresponding interaction strengths are 0.0, 3.0, 6.0, 9.0, 12.0. and 15.0

LSF for $N_c = 1$ and 4, respectively. When $\Delta = 0$, the BCS+ U model becomes the Hubbard model. It is well-known that the metal-insulator transition (MIT) occurs in the Hubbard model. For $N_c = 1$ calculation, the coherent peak at Fermi-level remains before the MIT occurs while the pseudogap appears in the $N_c = 4$ case. The origin of the pseudogap is the strong renormalization of electron mass in anti-nodal momentum sector. The quasi-particle weight of each momentum sector is shown in Fig. 8.7.

For non-zero Δ , the system is a superconductor in the noninteracting limit. The characteristic V-shape gap of d -wave superconductor appears in both clusters of sizes $N_c = 1$ and 4. As the interaction strength becomes larger, the size of gap, which is estimated by peak-to-peak distance, decreases for $N_c = 1$ calculation. And finally the superconductor-to-Mott insulator transition occurs. Within the superconductor phase, the coherent peaks are well-defined.

However, the results for $N_c = 4$ are qualitatively different from those for $N_c = 1$. As the interaction strength increases, the size of the superconducting gap increases. And the superconducting coherent peaks continuously smear into the emergent Hubbard peaks. No signature for the superconductor-to-Mott insulator transition is found in the LSF.

8.3.3 Local spectral function for hole-doped system

We also investigate the spectral properties of the system away from the half-filling. Figure 8.6 shows the LSF for the hole-doped system calculated by $N_c = 1$ and 4. The doping-concentration is controlled by the chemical potential

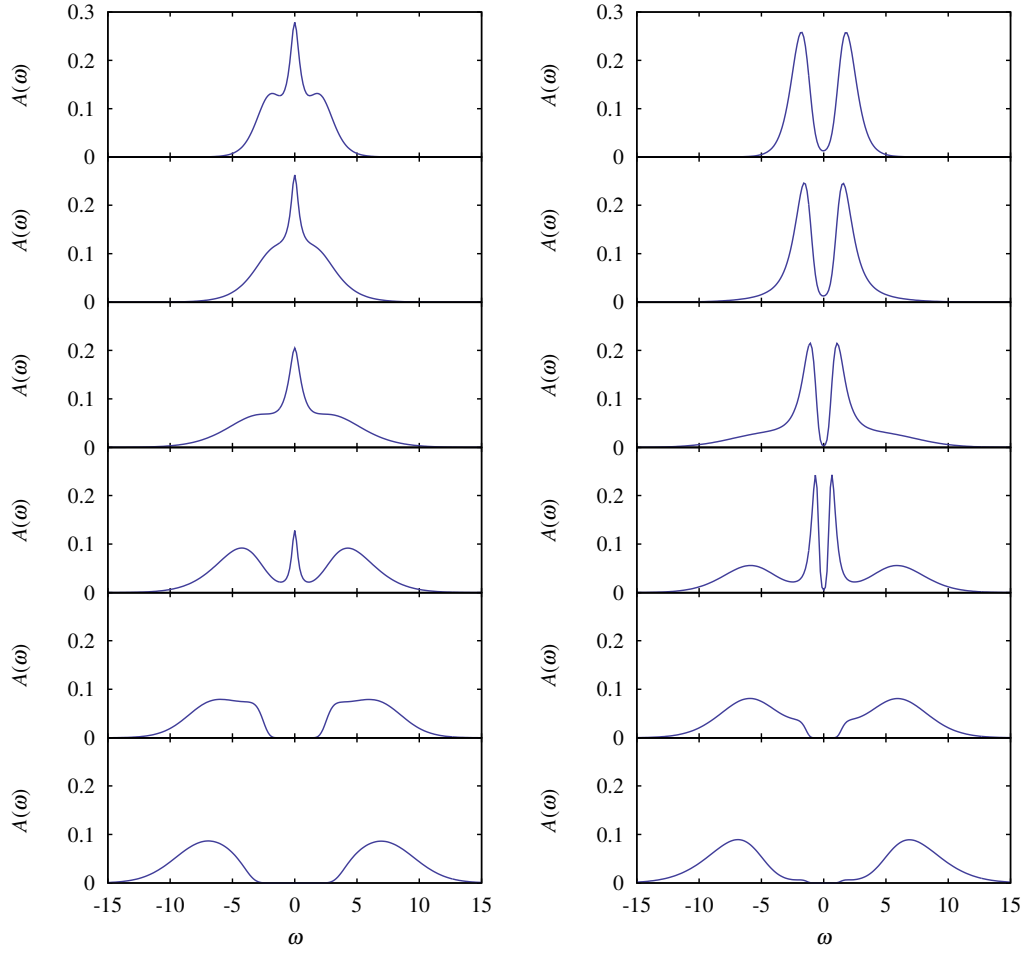


Figure 8.4: Local spectral function in the half-filled system for $N_c = 1$. The left (right) figure represents the $\Delta = 0.0$ (0.5) results at $T = 1/8$. From top to bottom, the corresponding interaction strengths are 0.0 , 3.0 , 6.0 , 9.0 , 12.0 , and 15.0 .

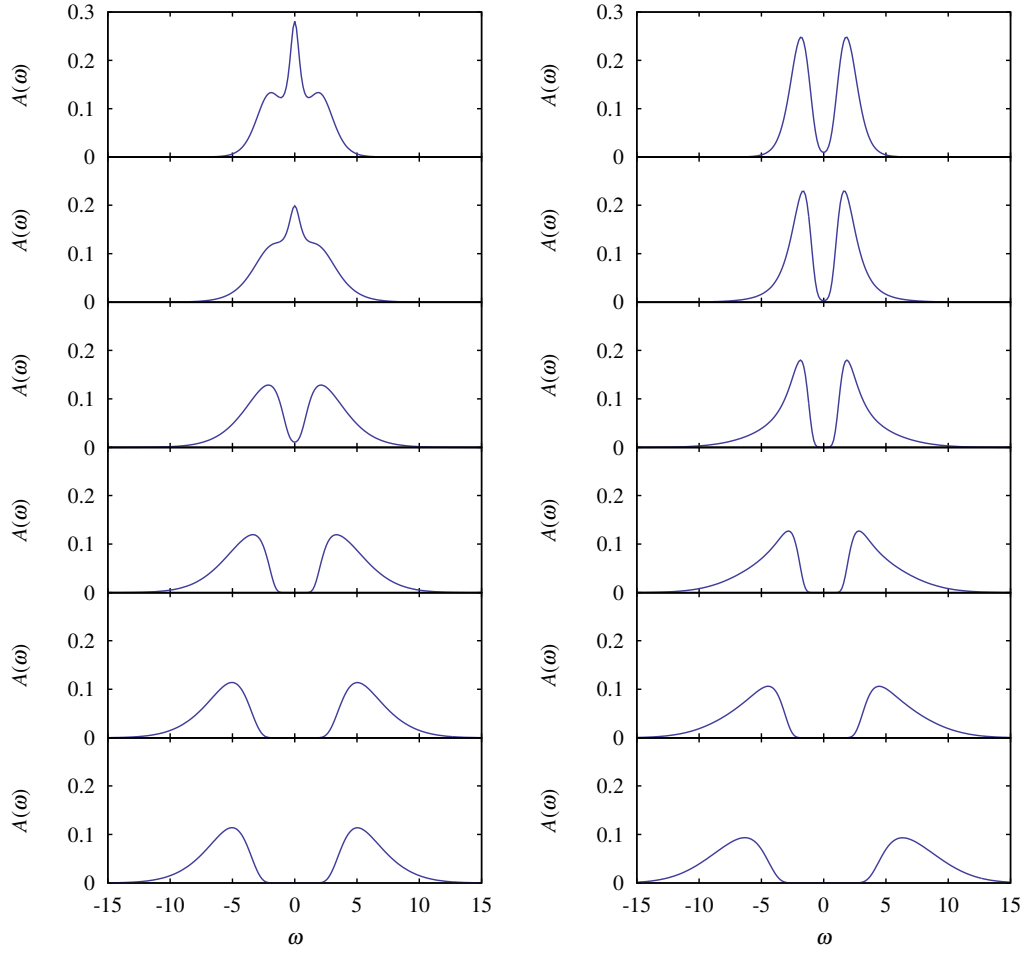


Figure 8.5: Local spectral function in the half-filled system for $N_c = 4$. The left (right) figure represents the $\Delta = 0.0$ (0.5) case at $T = 1/4$. From top to bottom, the corresponding interaction strengths are 0.0, 3.0, 6.0, 9.0, 12.0, and 15.0.

and the interaction strength is fixed to be $U = 12$. In the case of $N_c = 1$, the superconducting coherent peaks reemerge when $\mu \lesssim 0.6\mu_0$ where μ_0 is the value of the chemical potential at half-filling, $\mu_0 = U/2$. These coherent peaks are well-separated from the upper and the lower Hubbard bands, resulting in a four-peak structure in the LSF.

On the other hand, for $N_c = 4$, the smeared superconducting coherent peaks become sharper as the doping concentration increases. In this case, the lower coherent peak is not separated from the lower Hubbard band up to the high doping concentration while the upper coherent peak emerges inside the Mott gap. Thus the three-peak spectral function is found in $N_c = 4$ calculation.

For both $N_c = 1$ and 4, the superconducting coherent peaks become more prominent as the temperature decreases.

8.3.4 Quasi-particle weight for half-filled system

Figure 8.7 shows the quasi-particle weight as a function of the interaction strength for the half-filled system. The quasi-particle weight is defined as

$$Z_{\mathbf{K}} = \left(1 - \frac{\partial \text{Re}\Sigma_N(\mathbf{K}, \omega)}{\partial \omega} \bigg|_{\omega=0+} \right)^{-1}, \quad (8.7)$$

and can be approximated as

$$Z_{\mathbf{K}} \simeq \left(1 - \frac{\text{Im}\Sigma_N(\mathbf{K}, i\omega_0)}{\omega_0} \right)^{-1}, \quad (8.8)$$

within the Matsubara space at low temperatures. Since the self-energy can vary in the momentum space within DCA, we can observe the momentum-tile

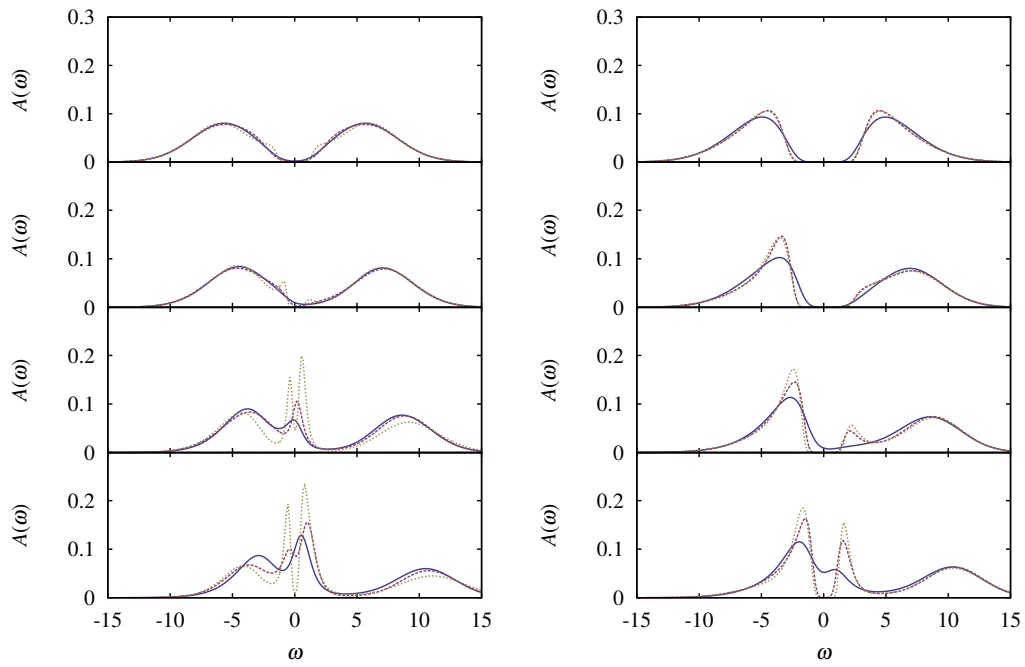


Figure 8.6: Local spectral function in the hole-doped system. The left (right) figure shows the $N_c = 1$ ($N_c = 4$) results for three different temperatures. The interaction strength U is fixed to be 12. From top to bottom, the chemical potential is adjusted to the value of $1.0\mu_0$, $0.8\mu_0$, $0.6\mu_0$, and $0.4\mu_0$, where $\mu_0 = U/2 = 6.0$. Solid, dashed, and dotted line correspond to $T = 1/2$, $1/4$, and $1/8$, respectively.

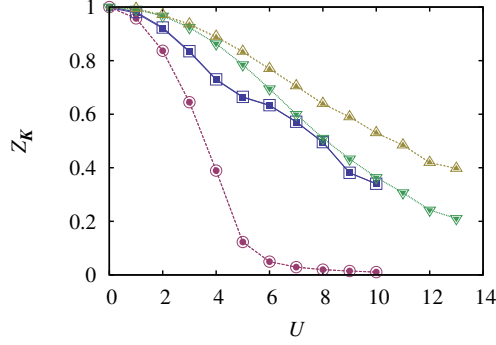


Figure 8.7: Quasi-particle weight of the half-filled system as a function of the interaction strength U , estimated by Eqn. (8.8). Closed squares and circles represent $\mathbf{K} = (0,0)$ and $(\pi,0)$ for $\Delta = 0.0$, respectively. Closed triangles and inverted-triangles show $\mathbf{K} = (0,0)$ and $(\pi,0)$ for $\Delta = 0.5$. Open symbols represent quasi-particle weight of $\mathbf{K} + (\pi, \pi)$ tile where \mathbf{K} is the momentum of tile corresponding to the closed symbols.

dependent quasi-particle weight.

For the $\Delta = 0$ case, the quasi-particle weights in $(\pi, 0)$ and $(0, \pi)$ sectors show the stronger mass renormalization than those for $(0, 0)$ and (π, π) . These momentum dependent trends also appear when the finite Δ is introduced. However, in the presence of the finite superconducting pairing the overall mass renormalization is less severe.

8.3.5 Renormalized superconducting gap

Figure 8.8 presents the coarse-grained superconducting pairing as a function of the interaction strength and the doping concentration. The renormalization of the superconducting gap can be estimated by the coarse-grained anomalous

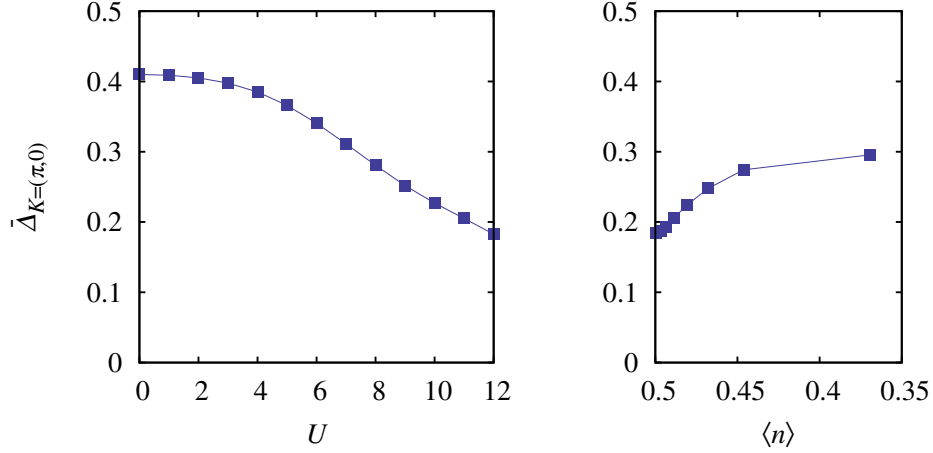


Figure 8.8: Coarse-grained superconducting pairing as a function of the interaction strength and the hole-doping concentration at the temperature $T = 1/8$ for the pairing amplitude $\Delta = 0.5$. The left figure shows the results of the half-filled system. And the right figure shows the doping-dependence of the coarse-grained pairing for a given interaction strength $U = 12$.

Green function,

$$\bar{\Delta}_{\mathbf{K}=(\pi,0)} = G_{\mathbf{K}=(\pi,0)}^A(0^+) . \quad (8.9)$$

As the interaction strength increases the coarse-grained superconducting pairing decreases monotonically. In contrast to $N_c = 1$ calculation, however, the renormalized pairing remains finite up to very high interaction strength $U = 15$ for $N_c = 4$ calculation.

When the hole-doping is introduced to the system, the coarse-grained superconducting pairing increases monotonically. This indicates that the hole-doping and the decrease in the interaction strength have the similar effects on the coarse-grained superconducting pairing.

8.4 Summary

We have investigated the BCS+ U model in the dynamical cluster approximation combined with the continuous-time quantum Monte Carlo method. We have confirmed the dual character of the Hamiltonian by the numerical calculations. By analyzing the local spectral properties, we have found the common features of the model independent of the cluster size; the suppression of the superconductivity when the strong mutual interaction is introduced and the reemergence when the system is hole-doped. For the hole-doped strong interaction region, the coherent superconducting peak develops well as the temperature decreases. The transition nature, however, is qualitatively different depending on the cluster size N_c , indicating that the spatial fluctuations have crucial effects in the system.

Appendix A

High-frequency Expansion of Green Function

In this appendix, we present the high-frequency expansion of the general Green function and extract the expansion coefficients of the specific models of the previous chapters. For two reasons, this high-frequency expansion of Green function is very useful in the dynamical mean-field theory and continuous-time quantum Monte Carlo method. First, it gives the information about the high-frequency tail of Green function which is very difficult to access due to the limited number of the numerical data. In addition, using the high-frequency tail, we can avoid the numerical Fourier transformation of the singular parts of Green function. The most singular terms are subtracted from the Green function and can be Fourier-transformed analytically. The remaining part of Green function is well-behaved during the numerical Fourier transformation.

The general Matsubara Green function is the Fourier transformation of the imaginary-time Green function. By the successive integration by parts, we

can obtain the $1/i\omega_n$ -expansion. The Green function can be represented by the infinite series

$$\begin{aligned}
G_{\mu\nu}(i\omega_n) &= \int_0^\beta d\tau G(\tau) e^{i\omega_n \tau} \\
&= \frac{-G(\beta) - G(0)}{i\omega_n} - \frac{-G'(\beta) - G'(0)}{(i\omega_n)^2} + \frac{-G''(\beta) - G''(0)}{(i\omega_n)^3} + \dots \\
&= -\sum_{k \geq 0} (-1)^k \frac{G^{(k)}(0^+) - G^{(k)}(0^-)}{(i\omega_n)^k} .
\end{aligned} \tag{A.1}$$

Here, $G^{(k)}(\tau)$ is the k -th derivative by the imaginary-time and we use the property that $G(\beta^-) = -G(0^-)$ on the third line.

For a general index μ , the Green function is defined by

$$G_\mu(\tau) = -\frac{1}{Z} \text{tr} \left[e^{-\beta \mathcal{H}} \mathcal{T}_\tau (c_\mu(\tau) c_\mu^\dagger) \right] , \tag{A.2}$$

where $c_\mu(\tau) = e^{\tau \mathcal{H}} c_\mu e^{-\tau \mathcal{H}}$, and the derivatives of the Green function at $\tau = 0^+$ and 0^- are expressed in terms of the commutation relation

$$\begin{aligned}
\partial_\tau G_\mu(0^+) &= -\langle \mathcal{T}_\tau ([\mathcal{H}, c_\mu] c_\mu^\dagger) \rangle , \\
\partial_\tau G_\mu(0^-) &= \langle \mathcal{T}_\tau (c_\mu^\dagger [\mathcal{H}, c_\mu]) \rangle .
\end{aligned} \tag{A.3}$$

It can be easily generalized to the k -th derivatives,

$$\begin{aligned}
G_\mu^{(k)}(0^+) - G_\mu^{(k)}(0^-) &= -\left\langle \mathcal{T}_\tau \left\{ \overbrace{[\mathcal{H}, [\mathcal{H}, \dots [\mathcal{H}, c_\mu] \dots]]}^{k \text{ times}}, c_\mu^\dagger \right\} \right\rangle \\
&\equiv \langle \mathcal{T}_\tau \{ [\mathcal{H}, c_\mu]_{\{k\}}, c_\mu^\dagger \} \rangle .
\end{aligned} \tag{A.4}$$

with $G_\mu^{(k)}(\tau) \equiv \partial_\tau^k G_\mu(\tau)$. Then, the Matsubara Green function is written in

the form

$$\begin{aligned}
G_\mu(i\omega_n) &= \sum_{k \geq 0} (-1)^k \frac{\langle \mathcal{T}_\tau \{ [\mathcal{H}, c_\mu]_{\{k\}}, c_\nu^\dagger \} \rangle}{(i\omega_n)^k} \\
&\equiv \sum_{k \geq 0} \frac{G_{\mu,k}}{(i\omega_n)^k} .
\end{aligned} \tag{A.5}$$

In the following sections, we show how to determine the coefficients of the expansion, $G_{\mu,k}$, for various models.

A.1 Hubbard model

In the momentum space, the Hubbard model is described by

$$\mathcal{H} = \sum_{\mathbf{k}\sigma} (\epsilon_{\mathbf{k}} - \mu) c_{\mathbf{k}\sigma}^\dagger c_{\mathbf{k}\sigma} + \frac{U}{N} \sum_{\mathbf{q}} n_{\mathbf{q}\uparrow} n_{-\mathbf{q}\downarrow} , \tag{A.6}$$

where $n_{\mathbf{q}\sigma} = \sum_{\mathbf{k}} c_{\mathbf{k}\sigma}^\dagger c_{\mathbf{k}+\mathbf{q}\sigma}$. By evaluating the commutation relations, we can obtain the coefficients of the high-frequency expansion and the first three coefficients are

$$\begin{aligned}
G_{\mathbf{k}\sigma,1} &= \langle \{ c_{\mathbf{k}\sigma}, c_{\mathbf{k}\sigma}^\dagger \} \rangle = 1 , \\
G_{\mathbf{k}\sigma,2} &= -\langle \{ [\mathcal{H}, c_{\mathbf{k}\sigma}], c_{\mathbf{k}\sigma}^\dagger \} \rangle \\
&= \epsilon_{\mathbf{k}} - \mu + U \langle n_{\bar{\sigma}} \rangle , \\
G_{\mathbf{k}\sigma,3} &= \langle \{ [\mathcal{H}, [\mathcal{H}, c_{\mathbf{k}\sigma}]], c_{\mathbf{k}\sigma}^\dagger \} \rangle \\
&= (\epsilon_{\mathbf{k}} - \mu)^2 + 2(\epsilon_{\mathbf{k}} - \mu)U \langle n_{\bar{\sigma}} \rangle + U^2 \langle n_{\bar{\sigma}} \rangle .
\end{aligned} \tag{A.7}$$

For the Bethe lattice in the infinite dimensions at half-filling, the local Green function is

$$\begin{aligned}
G_\sigma(i\omega_n) &= \frac{1}{N} \sum_{\mathbf{k}} G_{\mathbf{k}\sigma}(i\omega_n) \\
&= \frac{1}{i\omega_n} + \frac{U\langle n_{\bar{\sigma}} \rangle - \mu}{(i\omega_n)^2} + \frac{t^2 + \mu^2 - 2\mu U\langle n_{\bar{\sigma}} \rangle + U^2\langle n_{\bar{\sigma}} \rangle}{(i\omega_n)^3} + \mathcal{O}\left(\frac{1}{(i\omega_n)^4}\right).
\end{aligned} \tag{A.8}$$

Here, we use the properties of half-filled Bethe lattice

$$\begin{aligned}
\frac{1}{N} \sum_{\mathbf{k}} \epsilon_{\mathbf{k}} &= \int_{-\infty}^{\infty} d\epsilon \epsilon \rho(\epsilon) = 0, \\
\frac{1}{N} \sum_{\mathbf{k}} \epsilon_{\mathbf{k}}^2 &= \int_{-\infty}^{\infty} d\epsilon \epsilon^2 \rho(\epsilon) = t^2.
\end{aligned} \tag{A.9}$$

Here, $\rho(\epsilon)$ is the semi-circular density of states and t is the next-nearest neighbor hopping amplitude.

A.2 Ionic Hubbard model

In the momentum space, the Hamiltonian of the ionic Hubbard model is given by

$$\mathcal{H} = \sum_{\mathbf{k}\sigma} \epsilon_{\mathbf{k}} (c_{\mathbf{k}A\sigma}^\dagger c_{\mathbf{k}B\sigma} + c_{\mathbf{k}B\sigma}^\dagger c_{\mathbf{k}A\sigma}) + \sum_{\mathbf{k}\alpha\sigma} (\Delta_\alpha - \mu) c_{\mathbf{k}\alpha\sigma}^\dagger c_{\mathbf{k}\alpha\sigma} + \frac{U}{N} \sum_{\mathbf{q}\alpha} n_{\mathbf{q}\alpha\uparrow} n_{-\mathbf{q}\alpha\downarrow}, \tag{A.10}$$

where α is the sublattice index, A or B , $\Delta_\alpha = (-1)^\alpha \Delta$ and $n_{\mathbf{q}\alpha\sigma} = \sum_{\mathbf{k}} c_{\mathbf{k}\alpha\sigma}^\dagger c_{\mathbf{k}+\mathbf{q}\alpha\sigma}$. Note that $(-1)^A = +1$ and $(-1)^B = -1$. Using the commutation relations,

the coefficients of the expansion are

$$\begin{aligned}
G_{\mathbf{k}\alpha\sigma,1} &= \langle \{c_{\mathbf{k}\alpha\sigma}, c_{\mathbf{k}\alpha\sigma}^\dagger\} \rangle = 1 , \\
G_{\mathbf{k}\alpha\sigma,2} &= -\langle \{[\mathcal{H}, c_{\mathbf{k}\alpha\sigma}], c_{\mathbf{k}\alpha\sigma}^\dagger\} \rangle \\
&= \Delta_\alpha - \mu + U \langle n_{\alpha\bar{\sigma}} \rangle , \\
G_{\mathbf{k}\alpha\sigma,3} &= \langle \{[\mathcal{H}, [\mathcal{H}, c_{\mathbf{k}\alpha\sigma}]], c_{\mathbf{k}\alpha\sigma}^\dagger\} \rangle \\
&= \epsilon_{\mathbf{k}}^2 + (\Delta_\alpha - \mu)^2 + 2(\Delta_\alpha - \mu)U \langle n_{\alpha\bar{\sigma}} \rangle + U^2 \langle n_{\alpha\bar{\sigma}} \rangle . \quad (\text{A.11})
\end{aligned}$$

For half-filled Bethe lattice in the infinite dimensions, the local Green function of sublattice α leads to

$$\begin{aligned}
G_{\alpha\sigma}(i\omega_n) &= \frac{1}{N} \sum_{\mathbf{k}} G_{\mathbf{k}\alpha\sigma}(i\omega_n) \\
&= \frac{1}{i\omega_n} + \frac{U \langle n_{\bar{\sigma}} \rangle + \Delta_\alpha - \mu}{(i\omega_n)^2} + \frac{t^2 + (\Delta_\alpha - \mu)^2 + 2(\Delta_\alpha - \mu)U \langle n_{\alpha\bar{\sigma}} \rangle + U^2 \langle n_{\alpha\bar{\sigma}} \rangle}{(i\omega_n)^3} \\
&\quad + \mathcal{O}\left(\frac{1}{(i\omega_n)^4}\right) . \quad (\text{A.12})
\end{aligned}$$

A.3 Two-orbital Hubbard model

The two-orbital Hubbard model with the Ising-type Hund's coupling is

$$\begin{aligned}
\mathcal{H} &= \sum_{\mathbf{k}\alpha\sigma} (\epsilon_{\mathbf{k}\alpha} - \mu) c_{\mathbf{k}\alpha\sigma}^\dagger c_{\mathbf{k}\alpha\sigma} + \frac{U}{N} \sum_{\mathbf{q}\alpha} n_{\mathbf{q}\alpha\uparrow} n_{-\mathbf{q}\alpha\downarrow} \\
&\quad + \frac{U' - J}{N} \sum_{\mathbf{q}\sigma} n_{\mathbf{q}1\sigma} n_{-\mathbf{q}2\sigma} + \frac{U'}{N} \sum_{\mathbf{q}\sigma} n_{\mathbf{q}1\sigma} n_{-\mathbf{q}2\bar{\sigma}} , \quad (\text{A.13})
\end{aligned}$$

where α is the orbital index, 1 or 2. Using the commutation relations, the coefficients of the expansion become

$$\begin{aligned}
G_{\mathbf{k}\alpha\sigma,1} &= \langle \{c_{\mathbf{k}\alpha\sigma}, c_{\mathbf{k}\alpha\sigma}^\dagger\} \rangle = 1 , \\
G_{\mathbf{k}\alpha\sigma,2} &= -\langle \{[\mathcal{H}, c_{\mathbf{k}\alpha\sigma}], c_{\mathbf{k}\alpha\sigma}^\dagger\} \rangle \\
&= \epsilon_{\mathbf{k}\alpha} - \mu + U\langle n_{\alpha\bar{\sigma}} \rangle + (U' - J)\langle n_{\bar{\alpha}\sigma} \rangle + U'\langle n_{\bar{\alpha}\bar{\sigma}} \rangle , \\
G_{\mathbf{k}\alpha\sigma,3} &= \langle \{[\mathcal{H}, [\mathcal{H}, c_{\mathbf{k}\alpha\sigma}]], c_{\mathbf{k}\alpha\sigma}^\dagger\} \rangle \\
&= (\epsilon_{\mathbf{k}\alpha} - \mu)^2 + 2(\epsilon_{\mathbf{k}\alpha} - \mu) [U\langle n_{\alpha\bar{\sigma}} \rangle + (U' - J)\langle n_{\bar{\alpha}\sigma} \rangle + U'\langle n_{\bar{\alpha}\bar{\sigma}} \rangle] \\
&\quad + U^2\langle n_{\alpha\bar{\sigma}} \rangle + (U' - J)^2\langle n_{\bar{\alpha}\sigma} \rangle + U'^2\langle n_{\bar{\alpha}\bar{\sigma}} \rangle \\
&\quad + 2[U(U' - J)\langle n_{\alpha\bar{\sigma}} n_{\bar{\alpha}\sigma} \rangle + UU'\langle n_{\alpha\bar{\sigma}} n_{\bar{\alpha}\bar{\sigma}} \rangle + U'(U' - J)\langle n_{\bar{\alpha}\bar{\sigma}} n_{\bar{\alpha}\sigma} \rangle] .
\end{aligned} \tag{A.14}$$

For half-filled Bethe lattice in the infinite dimensions, the local Green function of orbital α leads to

$$\begin{aligned}
G_{\alpha\sigma}(i\omega_n) &= \frac{1}{N} \sum_{\mathbf{k}} G_{\mathbf{k}\alpha\sigma}(i\omega_n) \\
&= \frac{G_{\alpha\sigma,1}}{i\omega_n} + \frac{G_{\alpha\sigma,2}}{(i\omega_n)^2} + \frac{G_{\alpha\sigma,3}}{(i\omega_n)^3} + \mathcal{O}\left(\frac{1}{(i\omega_n)^4}\right) , \tag{A.15}
\end{aligned}$$

where

$$\begin{aligned}
G_{\alpha\sigma,1} &= 1 , \\
G_{\alpha\sigma,2} &= -\mu + U\langle n_{\alpha\bar{\sigma}} \rangle + (U' - J)\langle n_{\bar{\alpha}\sigma} \rangle + U'\langle n_{\bar{\alpha}\bar{\sigma}} \rangle , \\
G_{\alpha\sigma,3} &= t_{\alpha}^2 + \mu^2 - 2\mu [U\langle n_{\alpha\bar{\sigma}} \rangle + (U' - J)\langle n_{\bar{\alpha}\sigma} \rangle + U'\langle n_{\bar{\alpha}\bar{\sigma}} \rangle] \\
&\quad + U^2\langle n_{\alpha\bar{\sigma}} \rangle + (U' - J)^2\langle n_{\bar{\alpha}\sigma} \rangle + U'^2\langle n_{\bar{\alpha}\bar{\sigma}} \rangle \\
&\quad + 2[U(U' - J)\langle n_{\alpha\bar{\sigma}} n_{\bar{\alpha}\sigma} \rangle + UU'\langle n_{\alpha\bar{\sigma}} n_{\bar{\alpha}\bar{\sigma}} \rangle + U'(U' - J)\langle n_{\bar{\alpha}\bar{\sigma}} n_{\bar{\alpha}\sigma} \rangle] .
\end{aligned}
\tag{A.16}$$

Here t_{α} is the next-nearest hopping amplitude of α -orbital.

Bibliography

- [1] J. Hubbard, Proc. R. Soc. Lond. A **276**, 238 (1963).
- [2] J. Kanamori, Prog. Theor. Phys. **30**, 275 (1963).
- [3] M. C. Gutzwiller, Phys. Rev. Lett. **10**, 159 (1963).
- [4] A. Georges, G. Kotliar, W. Krauth, and M. Rozenberg, Rev. Mod. Phys. **68**, 13 (1996).
- [5] D. B. McWhan, J. P. Remeika, T. M. Rice, W. F. Brinkman, J. P. Maita, and A. Menth, Phys. Rev. Lett. **27**, 941 (1971).
- [6] W. F. Brinkman and T. M. Rice, Phys. Rev. B **2**, 4302 (1970).
- [7] J. Hubbard, Proc. R. Soc. Lond. A **281**, 401 (1964).
- [8] J. C. Slater, Phys. Rev. **82**, 538 (1951).
- [9] P. W. Anderson, Science **235**, 1196 (1987).
- [10] P. W. Anderson, J. Phys. C **3**, 2436 (1970).
- [11] K. Haule, Phys. Rev. B **75**, 155113 (2007).

- [12] E. Gull, A. J. Millis, A. I. Lichtenstein, A. N. Rubtsov, M. Troyer, and P. Werner, Rev. Mod. Phys. **83**, 349 (2011).
- [13] W. Metzner and D. Vollhardt, Phys. Rev. Lett. **62**, 324 (1989).
- [14] T. Maier, M. Jarrell, T. Pruschke, and M. H. Hettler, Rev. Mod. Phys. **77**, 1027 (2005).
- [15] A. Georges and G. Kotliar, Phys. Rev. B **45**, 6479 (1992).
- [16] T. Pruschke, D. L. Cox, and M. Jarrell, Phys. Rev. B **47**, 3553 (1993).
- [17] J. E. Hirsch and R. M. Fye, Phys. Rev. Lett. **56**, 2521 (1986).
- [18] A. N. Rubtsov, V. V. Savkin, and A. I. Lichtenstein, Phys. Rev. B **72**, 035122 (2005).
- [19] E. Gull, P. Werner, O. Parcollet, and M. Troyer, Europhys Lett. **82**, 57003 (2008).
- [20] P. Werner, A. Comanac, L. de' Medici, M. Troyer, and A. J. Millis, Phys. Rev. Lett. **97**, 076405 (2006).
- [21] N. F. Mott, Proc. Phys. Soc. A **62**, 416 (1949).
- [22] F. Gebhard, *The Mott Metal-Insulator Transition* (Springer, New York, 1997) p. 317.
- [23] M. J. Rozenberg, R. Chitra, and G. Kotliar, Phys. Rev. Lett. **83**, 3498 (1999).

- [24] R. Bulla, T. A. Costi, and D. Vollhardt, Phys. Rev. B **64**, 45103 (2001).
- [25] M. J. Rozenberg, G. Kotliar, and X. Y. Zhang, Phys. Rev. B **49**, 10181 (1994).
- [26] N.-H. Tong, S.-Q. Shen, and F.-C. Pu, Phys. Rev. B **64**, 235109 (2001).
- [27] N. Blümer, *Mott-Hubbard Metal-Insulator Transition and Optical Conductivity in High Dimensions*, Ph.D. thesis, Universität Augsburg (2002).
- [28] R. Bulla, Phys. Rev. Lett. **83**, 136 (1999).
- [29] C. Castellani, C. Di Castro, D. Feinberg, and J. Ranninger, Phys. Rev. Lett. **43**, 1957 (1979).
- [30] E. Dagotto, Rev. Mod. Phys. **66**, 763 (1994).
- [31] M. Imada, A. Fujimori, and Y. Tokura, Rev. Mod. Phys. **70**, 1039 (1998).
- [32] J. Hubbard and J. B. Torrance, Phys. Rev. Lett. **47**, 1750 (1981).
- [33] J. B. Torrance, J. E. Vazquez, J. J. Mayerle, and V. Y. Lee, Phys. Rev. Lett. **46**, 253 (1981).
- [34] J. B. Torrance, A. Girlando, J. J. Mayerle, J. I. Crowley, V. Y. Lee, P. Batail, and S. J. LaPlaca, Phys. Rev. Lett. **47**, 1747 (1981).
- [35] N. Nagaosa and J. Takimoto, J. Phys. Soc. Jpn. **55**, 2735 (1986).

- [36] M. Avignon, C. A. Balseiro, C. R. Proetto, and B. Alascio, Phys. Rev. B **33**, 205 (1986).
- [37] T. Luty and B. Kuchta, Phys. Rev. B **35**, 8542 (1987).
- [38] K. Yonemitsu, Phys. Rev. B **65**, 205105 (2002).
- [39] T. Wilkens and R. M. Martin, Phys. Rev. B **63**, 235108 (2001).
- [40] M. Lemée-Cailleau, M. Le Cointe, H. Cailleau, T. Luty, F. Moussa, J. Roos, D. Brinkmann, B. Toudic, C. Ayache, and N. Karl, Phys. Rev. Lett. **79**, 1690 (1997).
- [41] S. Caprara, M. Avignon, and O. Navarro, Phys. Rev. B **61**, 15667 (2000).
- [42] S. Caprara, Int. J. Mod. Phys. B **14**, 3392 (2000).
- [43] S. Horiuchi, Y. Okimoto, R. Kumai, and Y. Tokura, J. Phys. Soc. Jpn. **69**, 1302 (2000).
- [44] Y. Anusooya-Pati and Z. G. Soos, Phys. Rev. B **63**, 205118 (2001).
- [45] T. Egami, S. Ishihara, and M. Tachiki, Science **261**, 1307 (1993).
- [46] S. Ishihara, T. Egami, and M. Tachiki, Phys. Rev. B **49**, 8944 (1994).
- [47] R. Resta and S. Sorella, Phys. Rev. Lett. **74**, 4738 (1995).
- [48] G. Ortiz, P. Ordejón, R. M. Martin, and G. Chiappe, Phys. Rev. B **54**, 13515 (1996).

- [49] N. Gidopoulos, S. Sorella, and E. Tosatti, Eur. Phys. J. B **14**, 217 (2000).
- [50] M. E. Torio, A. A. Aligia, and H. A. Ceccatto, Phys. Rev. B **64**, 121105 (2001).
- [51] J. Kuneš and V. I. Anisimov, Phys. Rev. B **78**, 033109 (2008).
- [52] M. Fabrizio, A. O. Gogolin, and A. A. Nersesyan, Phys. Rev. Lett. **83**, 2014 (1999).
- [53] Y. Z. Zhang, C. Q. Wu, and H. Q. Lin, Phys. Rev. B **67**, 205109 (2003).
- [54] A. Go and G. S. Jeon, J. Korean Phys. Soc. **53**, 1006 (2008).
- [55] A. Go and G. S. Jeon, Phys. Rev. B **84**, 195102 (2011).
- [56] K. Požgajčić and C. Gros, Phys. Rev. B **68**, 085106 (2003).
- [57] A. A. Aligia and C. D. Batista, Phys. Rev. B **71**, 125110 (2005).
- [58] A. A. Aligia, Phys. Rev. B **69**, 041101 (2004).
- [59] M. Fabrizio, A. Gogolin, and A. Nersesyan, Nucl. Phys. B **580**, 647 (2000).
- [60] G. I. Japaridze, R. Hayn, P. Lombardo, and E. Müller-Hartmann, Phys. Rev. B **75**, 245122 (2007).
- [61] C. D. Batista and A. A. Aligia, Phys. Rev. Lett. **92**, 246405 (2004).
- [62] M. E. Torio, A. A. Aligia, G. I. Japaridze, and B. Normand, Phys. Rev. B **73**, 115109 (2006).

- [63] S. R. Manmana, V. Meden, R. M. Noack, and K. Schönhammer, Phys. Rev. B **70**, 155115 (2004).
- [64] A. P. Kampf, M. Sekania, G. I. Japaridze, and P. Brune, J. Phys.: Condens. Matter **15**, 5895 (2003).
- [65] J. Lou, S. Qin, T. Xiang, C. Chen, G.-S. Tian, and Z. Su, Phys. Rev. B **68**, 045110 (2003).
- [66] L. Tincani, R. M. Noack, and D. Baeriswyl, Phys. Rev. B **79**, 165109 (2009).
- [67] H. Otsuka and M. Nakamura, Phys. Rev. B **71**, 155105 (2005).
- [68] N. Paris, K. Bouadim, F. Hebert, G. G. Batrouni, and R. T. Scalettar, Phys. Rev. Lett. **98**, 046403 (2007).
- [69] K. Bouadim, N. Paris, F. Hebert, G. G. Batrouni, and R. T. Scalettar, Phys. Rev. B **76**, 085112 (2007).
- [70] S. S. Kancharla and E. Dagotto, Phys. Rev. Lett. **98**, 016402 (2007).
- [71] H.-M. Chen, H. Zhao, H.-Q. Lin, and C.-Q. Wu, New J. Phys. **12**, 093021 (2010).
- [72] V. Tugushev, S. Caprara, and M. Avignon, Phys. Rev. B **54**, 5466 (1996).
- [73] A. A. Aligia, K. Hallberg, B. Normand, and A. P. Kampf, Phys. Rev. Lett. **93**, 076801 (2004).

- [74] A. Garg, H. R. Krishnamurthy, and M. Randeria, Phys. Rev. Lett. **97**, 046403 (2006).
- [75] L. Craco, P. Lombardo, R. Hayn, G. I. Japaridze, and E. Müller-Hartmann, Phys. Rev. B **78**, 075121 (2008).
- [76] K. Byczuk, M. Sekania, W. Hofstetter, and A. P. Kampf, Phys. Rev. B **79**, 121103(R) (2009).
- [77] P. Lombardo, R. Hayn, and G. I. Japaridze, Phys. Rev. B **74**, 085116 (2006).
- [78] X. Wang, R. Sensarma, and S. das Sarma, Phys. Rev. B **89** (2014).
- [79] E. Gull, P. Werner, X. Wang, M. Troyer, and A. J. Millis, Europhys Lett. **84**, 37009 (2008).
- [80] N. Trivedi and M. Randeria, Phys. Rev. Lett. **75**, 312 (1995).
- [81] E. Gull, M. Ferrero, O. Parcollet, A. Georges, and A. J. Millis, Phys. Rev. B **82**, 155101 (2010).
- [82] A. J. Kim, M. Y. Choi, and G. S. Jeon, J. Korean Phys. Soc. **64**, 268 (2014).
- [83] A. Georges, L. D. Medici, and J. Mravlje, Annu. Rev. Condens. Matter Phys. **4**, 137 (2013).
- [84] R. Arita and K. Held, Phys. Rev. B **72**, 201102(R) (2005).

- [85] M. Ferrero, F. Becca, M. Fabrizio, and M. Capone, Phys. Rev. B **72**, 205126 (2005).
- [86] A. Koga, N. Kawakami, T. Rice, and M. Sigrist, Physica B **359-361**, 1366 (2005).
- [87] A. Koga, N. Kawakami, T. M. Rice, and M. Sigrist, Phys. Rev. B **72**, 045128 (2005).
- [88] A. Koga, N. Kawakami, T. M. Rice, and M. Sigrist, Phys. Rev. Lett. **92**, 216402 (2004).
- [89] A. Koga, Y. Imai, and N. Kawakami, Phys. Rev. B **66**, 165107 (2002).
- [90] H. Lee, Y.-Z. Zhang, H. Jeschke, and R. Valentí, Ann. Phys. (Berlin) **523**, 689 (2011).
- [91] M. Greger, M. Kollar, and D. Vollhardt, Phys. Rev. Lett. **110**, 046403 (2013).
- [92] C. Knecht, N. Blümer, and P. van Dongen, Phys. Rev. B **72**, 081103 (2005).
- [93] H. Lee, Y.-Z. Zhang, H. O. Jeschke, R. Valentí, and H. Monien, Phys. Rev. Lett. **104**, 026402 (2010).
- [94] A. Liebsch, Phys. Rev. Lett. **95**, 116402 (2005).
- [95] P. Werner and A. J. Millis, Phys. Rev. Lett. **99**, 126405 (2007).

- [96] H. Hafermann, K. R. Patton, and P. Werner, Phys. Rev. B **85**, 205106 (2012).
- [97] E. Jakobi, N. Blümer, and P. van Dongen, Phys. Rev. B **87**, 205135 (2013).
- [98] L. de' Medici, S. Hassan, M. Capone, and X. Dai, Phys. Rev. Lett. **102**, 126401 (2009).
- [99] T. Kita, T. Ohashi, and N. Kawakami, Phys. Rev. B **84**, 195130 (2011).
- [100] S. Nakatsuji and Y. Maeno, Phys. Rev. Lett. **84**, 2666 (2000).
- [101] V. Anisimov, I. Nekrasov, D. Kondakov, T. Rice, and M. Sigrist, Eur. Phys. J. B **25**, 191 (2002).
- [102] L. de' Medici, Phys. Rev. B **83**, 205112 (2011).
- [103] S. Sakai, Y. Motome, and M. Imada, Phys. Rev. Lett. **102**, 056404 (2009).
- [104] Y. Z. Zhang and M. Imada, Phys. Rev. B **76**, 045108 (2007).
- [105] M. H. Hettler, M. Mukherjee, M. Jarrell, and H. R. Krishnamurthy, Phys. Rev. B **61**, 12739 (2000).
- [106] G. Kotliar, S. Y. Savrasov, G. Pálsson, and G. Biroli, Phys. Rev. Lett. **87**, 186401 (2001).
- [107] G. Kotliar, S. Y. Savrasov, K. Haule, V. S. Oudovenko, O. Parcollet, and C. A. Marianetti, Rev. Mod. Phys. **78**, 865 (2006).

- [108] A.-M. Tremblay, B. Kyung, and D. Sénéchal, *Low Temp. Phys.* **32**, 424 (2006).
- [109] H. Park, K. Haule, and G. Kotliar, *Phys. Rev. Lett.* **101**, 186403 (2008).
- [110] A. Liebsch, *Phys. Rev. B* **70**, 165103 (2004).
- [111] A. Liebsch, *Phys. Rev. Lett.* **91**, 226401 (2003).
- [112] S. Biermann, L. de' Medici, and A. Georges, *Phys. Rev. Lett.* **95**, 206401 (2005).
- [113] A. Liebsch and T. A. Costi, *Eur. Phys. J. B* **51**, 523 (2006).
- [114] T. A. Costi and A. Liebsch, *Phys. Rev. Lett.* **99**, 236404 (2007).
- [115] A. Damascelli, Z. Hussain, and Z.-X. Shen, *Rev. Mod. Phys.* **75**, 473 (2003).
- [116] M. Imada, A. Fujimori, and Y. Tokura, *Rev. Mod. Phys.* **70**, 1039 (1998).
- [117] D. Fournier, G. Levy, Y. Pennec, J. McChesney, A. Bostwick, E. Rotenberg, R. Liang, W. Hardy, D. Bonn, I. Elfimov, and A. Damascelli, *Nat. Phys.* **6**, 905 (2010).
- [118] S. Kancharla and S. Okamoto, *Phys. Rev. B* **75**, 193103 (2007).
- [119] K. Bouadim, G. Batrouni, F. Hébert, and R. Scalettar, *Phys. Rev. B* **77**, 144527 (2008).

- [120] R. Rüger, L. F. Tocchio, R. Valentí, and C. Gros, New J. Phys. **16**, 033010 (2014).
- [121] M. Golor, T. Reckling, L. Classen, M. M. Scherer, and S. Wessel, arXiv:1409.1103v1 .
- [122] K. Park, Phys. Rev. Lett. **95**, 027001 (2005).
- [123] K. Park, Phys. Rev. B **72**, 245116 (2005).
- [124] K. Park, New J. Phys. **11**, 073027 (2009).

국문 초록

이 논문에서는 동역학적 평균마당 이론과 연속 시간 양자 몬트카를로 방법을 이용한 허바드 형태 모형연구를 다룬다. 허바드 모형이 기술할 수 있는 모트 물리의 다양한 측면을 살펴보기 위하여, 기존의 홀 궤도함수 허바드 모형에 추가적인 자유도를 도입한다. 추가적으로 도입된 자유도는 엇갈림 격자 퍼텐셜, 뭇 궤도함수 효과, 두겹쳐 구조, 그리고 초전도 효과가 있다. 도입된 자유도에 따라 동역학적 평균장 이론 뿐 아니라 이의 뭇 궤도함수 확장 또는 송이 확장 등이 사용된다. 또한 연속 시간 양자 몬테카를로 방법의 상호보완적인 두개의 풀이법이 사용된다.

먼저 무한 차원 허바드 모형에서의 모트 상전이에 대해 다룬다. 연속 시간 양자 몬테카를로 방법이 동역학적 평균장 이론과 결합되어 사용되며, 이를 통해 충분히 낮은 온도의 물리를 정확하게 관찰할 수 있다. 몬테카를로 표본추출로부터 직접 측정되는 이중점유도와 운동에너지 밀도를 이용하여 모형의 상그림을 그린다. 특히 도체와 절연체가 공존하는 영역에서 불연속적 상전이 선을 결정하는 것이 이 연구의 주된 목적이다. 계산된 상전이선은 기존의 결과들과 좋은 일치를 보이며, 체계적으로 유한 온도에서의 결과를 고려함에 따라 알려진 절대영도의 결과를 점차 정확하게 예측하는 것이 확인된다.

다음으로 무한차원 이온 허바드 모형의 도체-절연체 상전이에 대해 다룬다. 연속 시간 양자 몬테카를로 방법과 동역학적 평균장 이론을 통하여, 상호작용의 크기가 커지면, 계의 성질이 락절연체에서 도체로 교차하고, 이어 도체가 모트 절연체로 불연속 상전이 함이 확인된다. 이 불연속 상전이는 특정 고비온도 이하에서만 일어나며, 보다 높은 온도에서는 교차한다. 고비온도의 크기는 엇갈림 격자 퍼텐셜의 크기에 따라 증가한다. 에너지 밀도의 온도 변화를 분석함으로서, 중간에 등장하는 도체가 페르미 액체임을 확인한다. 또한 이 도체는 강한 엇갈림 격자 퍼텐셜과 낮은 온도의 조건에서도 안정적으로 존재한다.

이후에는 뭇 궤도함수 허바드 모형의 유한온도 상전이에 대해 다룬다. 이징 형태의 훈트 결합이 사용되었다. 동역학적 평균장 이론의 뭇 궤도함수 확장이 강한 결합 연속 시간 양자 몬테카를로 방법과 함께 사용된다. 놀랍게도 기울기 역전 불연속 모트 상전이가 궤도함수 선택적인 모트상과 모트 절연체 사이에서 발견된다. 훈트 결합의 크기가 커질수록 기울기 역전 모트 상전이의 고비온도는 감소한다. 특정 훈트 결합 이상에서 불연속 상전이는 유한온도 교차로 변한다.

허바드 모형에서의 두겹커 효과 또한 연구되었다. 동역학적 송이 어림이 약한 결합 연속시간 양자 몬테카를로 방법과 함께 사용된다. 기존에 연구된 자성 상그림은 여전히 확실하지 않은 부분이 남아있다. 이 연구에서는 여덟 개의 격자점으로 구성된 송이가 처음으로 사용되었으며, 이는 무한 격자의 대칭성을 보존한다. 계의 자기적 성질과 관련된 도체-절연체 상전이가 연구되었으며, 계산 결과들이 절대영도의 물리에 암시하는 바에 대해 논한다.

마지막으로 구츠윌러-투영된 비시에스 모형의 자연스러운 확장인 비시에스+유 모형을 다룬다. 이 연구를 위하여, 동역학적 송이 어림과 약한 결합

연속 시간 양자 몬테카를로 방법이 사용되었으며, 송이 크기 변화를 통해 계산의 안정성을 확인하였다. 이 연구의 주제는 현상론적인 디-파동 초전도체에서 상호작용의 효과이다. 상호작용의 크기 또는 양공 첨가 농도를 조절함에 따라 초전도체와 모트 부도체 사이의 상전이가 관찰된다. 이 계의 상전이에 따른 스펙트럼 함수의 성질에 대해 논한다.

주요어: 강상관계, 허바드 형태 모형, 동역학적 평균장 이론, 연속 시간 양자 몬테카를로

학번: 2009-20403

